

Nonlocal Diffusion of Vortices in the Magnetic-Flux Creep Region inside a Hard Superconductor

V. R. Romanovskii

Presented by Academician S.T. Belyaev May 17, 1999

Received May 19, 1999

For describing the electrodynamics of hard superconductors, the critical-state model is widely used. According to this model, a current with a density assumed to be critical is induced in a hard superconductor as a response to any external perturbation giving rise to an electric voltage in this superconductor. For substantiating this model, the idea of pinning vortices according to which the vortex structure relaxes to the equilibrium state between the pinning and Lorentz forces acting on a vortex. In this case, the nonlocal dynamics of vortices is described by a macroscopic function, namely, the magnetic induction. This is true when the vortex density varies gradually in the spatial scale on the order of the London depth. In these cases, the evolution of the magnetic flux is a direct consequence of the collective nature of diffusion processes proceeding in hard semiconductors as a response to macroscopic perturbations of various nature. For such phenomena, the critical-state model makes it possible to investigate quasistatic properties of a hard superconductor in a simple and obvious form and to calculate both its magnetization and energy loss for remagnetization using only the equation

$$\operatorname{curl} \mathbf{B} = \mu_0 \mathbf{J}_c.$$

Here, \mathbf{J}_c is the critical-current density in a superconductor. However, generally speaking, this value is, to a certain degree, conventional, which is associated with the fact that the voltage nonlinearly increasing with the electric current arises inside a hard superconductor well before the value J_c is attained. This is the region of the magnetic-flux creep in which the vortex lattice comes gradually into motion.

The investigation of the nature of the transport features and magnetic properties in superconductors of the second kind within the region of the magnetic-flux creep is of perpetual significant interest, especially in recent years in connection with discovering high-tem-

perature superconductors [1–7]. At the same time, in the cases when the screening currents incompletely penetrate a sample, no fundamental physical regularities in the electrodynamic behavior of a hard superconductor are formulated taking account of the creep. There are also a number of ambiguous solutions [3, 4] for high-temperature superconductors.

As follows from the creep thermal-activation model [1], the relation between the electric-field strength and the current density is described by the exponential function

$$E = E_c \exp\left(-\frac{U(J)}{kT}\right),$$

where E_c is the constant dependent on vortex-lattice parameters, T is temperature, and $U(J)$ is the potential barrier for thermal fluctuations. In the case of $U(J) = U_0(1 - J/J_c)$ (U_0 is the vortex activation energy), this expression can be written in the form

$$E = E_c \exp\left(\frac{J - J_c}{J_\delta}\right), \quad (1)$$

where $J_\delta = kTJ_c/U_0$.

In spite of the fact that formula (1) is universal for superconductors of the second kind in a wide range of variation of the electric-field strength, it has a number of singularities. First, $E \neq 0$ for $J = 0$. Second, the thermal-activation model leads to a linear dependence of the parameter J_δ on the superconductor temperature. At the same time, no similar dependence is observed for actual hard superconductors [8–10]. In this case, a number of phenomenological models have been formulated on the basis of numerous experiments, and, along with (1), the equation of the type presented in [10] can be used:

$$E = J\rho_n \exp\left(\frac{J}{J_\delta} + \frac{T - T_c}{T_\delta}\right), \quad (2)$$

where ρ_n is the superconductor specific electric resistance in the normal state, T_c is the superconductor crit-

ical temperature, T is the superconductor temperature, and J_δ and T_δ are the electric-current constant and temperature constant for the electric-field strength growth.

Equation (2) allows us to avoid an ambiguity associated with appearing nonzero values of E in (1) and also to take into account an effect of the finite increase in the superconductor temperature on the state's stability in the creep region [11]. It turns out to be possible to describe the actual experiments on determination of conditions for the conservation of the superconductivity in complex superconducting structures based on hard superconductors [12, 13]. Moreover, if we introduce $J_k = J_\delta(T_c - T_0)/T_\delta$ (where T_0 is the coolant temperature), which can be interpreted as a maximum possible value for the dissipation-free electric-current density in a hard superconductor, model (2) transforms into the critical-state model ($J_k \rightarrow J_c$) [10] for $J_\delta, T_\delta \rightarrow 0$. In this paper, we invoke dependence (2) and study features of a macroscopic mechanism for the magnetic-flux diffusion inside a hard superconductor.

We consider a well-cooled semi-infinite superconductor. Let a uniform external magnetic field parallel to the superconductor boundary surface be absent at an initial moment and then begin to grow with a constant rate $\dot{B} = \frac{dB}{dt}$. To simplify the analysis to be done, we assume that the critical temperature of the superconductor depends only parametrically on the induction of the external magnetic field. Then, in the isothermal approximation, the set of Maxwell equations

$$\frac{\partial \mathbf{B}}{\partial t} = -\text{curl } \mathbf{E}, \quad \text{curl } \mathbf{B} = \mu_0 \mathbf{J}$$

with respect to the electric-field strength is reduced to the initial boundary value problem of the form:

$$\mu_0 \frac{\partial J}{\partial E} \frac{\partial E}{\partial t} = \frac{\partial^2 E}{\partial x^2}, \quad (3)$$

$$\frac{\partial E}{\partial x}(0, t) = -\frac{dB}{dt}, \quad E(\infty, t) = 0, \quad E(x, 0) = 0, \quad (4)$$

where, according to (2), $\frac{\partial J}{\partial E} = \frac{J_\delta}{E(1 + J_\delta/J)}$.

We estimate the multiplier ahead of the derivative with respect to time in equation (3). Taking into account the fact that $\delta = J_\delta/J_k \ll 1$ [10] in hard superconductors, while $J < J_k$ in the region of the magnetic-flux creep, it is easy to find from equation (2)

$$\frac{E}{J_k \rho_n} \frac{J_k}{J} = \exp\left(\frac{J/J_k - 1}{J_\delta/J_k}\right) \ll 1.$$

Therefore, by virtue of the smallness of this term, we

obtain after obvious transformations

$$\frac{J_\delta}{E\left(1 + \frac{J_\delta}{J}\right)} = \frac{\frac{J_\delta}{J_k \rho_n}}{\frac{E}{J_k \rho_n} + \frac{J_\delta J_k}{J} \frac{E}{J_k \rho_n}} \sim \frac{J_\delta}{E}.$$

Thus, instead of equation (3), we can consider a simplified equation of the form

$$\mu_0 \frac{J_\delta}{E} \frac{\partial E}{\partial t} = \frac{\partial^2 E}{\partial x^2}.$$

We seek its solution in the class of the self-similar functions [14] by virtue of the existence of the one-parameter group of transformation with two invariants of the form

$$Z = \frac{\mu_0 J_\delta x}{\dot{B} t}, \quad V(Z) = \frac{\mu_0 J_\delta E}{\dot{B}^2 t}.$$

In this case, the initial problem is reduced to integrating the ordinary differential equation with respect to $V(Z)$

$$V \frac{d^2 V}{dZ^2} + Z \frac{dV}{dZ} - V = 0 \quad (5)$$

with the boundary conditions

$$\frac{dV}{dZ}(0) = -1, \quad V(\infty) = 0. \quad (6)$$

In Fig. 1, we plot the family of possible phase trajectories for equation (5), which, in the case of $Z = 0$, satisfy the desired boundary condition. Among the invariants shown, only the dashed curve describes a unique solution to equation (5). Actually, in the phase trajectories lying below the dashed curve, the sections with negative values of $V(Z)$ appear. Therefore, these solutions do not satisfy the physical meaning of equation (3). In the phase trajectories lying above the dashed curve, the positive values of $\frac{dV}{dZ}$ exist; i.e., in this case,

the requirement of boundedness for the values of $V(Z)$ as $Z \rightarrow \infty$ is violated. Therefore, boundary value problem (5), (6) belongs to the class of problems for which the bounded solution exists in a finite region [15]. In this case, it is easy to show that the desired invariant $V(Z)$ not only vanishes at a certain point $Z = Z_0$, but all its derivatives with respect to the variable Z are also

equal to zero $\left(\frac{d^k V}{dZ^k} = 0, k = 1, 2, 3, \dots\right)$. To determine

the value Z_0 , it is necessary to use the condition of continuity for the magnetic induction at the superconductor

surface. In the case under consideration, this condition has the form

$$\mu_0 \int_0^{x_0(t)} J(x, t) dx = \frac{dB}{dt} t, \quad t > 0, \quad (7)$$

where $x_0(t) = Z_0 \dot{B} t / \mu_0 J_\delta$.

These results show that, in the case of the macroscopic diffusion of magnetic vortices, the electromagnetic field induced by them occupies a bounded space in the hard-superconductor bulk. In other words, even in the presence of the creep, the electromagnetic field cannot instantly penetrate a hard superconductor for an infinitely large distance but propagates across it with a constant velocity in the form of a wave. On the wave front $x_0(t)$, which separates the magnetized region from the region into which no magnetic flux has yet penetrated, both the electric-field strengths and magnetic induction and all their derivatives with respect to the spatial coordinate are equal to zero. This fact represents a characteristic feature of the mechanism for diffusion processes proceeding in hard superconductors as a response to external perturbances of various nature.

Using the properties discussed of the $V(Z)$ invariant, we pass from boundary value problem (5), (6) to the equivalent integral equation of the second kind

$$V(Z) = Z_0 - Z + \frac{Z^2 - Z_0^2}{2} - \int_{Z_0}^Z dx \int_0^x \frac{y}{V(y)} \frac{dV}{dy} dy.$$

For solving this equation, it is reasonable to use the method of successive approximations. It turns out in this case that even the linear approach $V_0 = Z_0 - Z$ approximates the desired values of $V(Z)$ with a good accuracy virtually within the entire range of variation of Z . By virtue of the above-considered specific features of the $V(Z)$ invariant, a slight difference is observed only in a small neighborhood of the point $Z = Z_0$. Therefore, in the linear approximation, the electric-field strength induced by the magnetic-flux diffusion inside the hard superconductor is described by the expression

$$E(x, t) = \frac{dB}{dt} [x_0(t) - x], \quad 0 \leq x \leq x_0(t), \quad t > 0.$$

In this case, the distribution of the magnetic-field induction inside the hard superconductor has the following form in quadratures:

$$B(x, t) = \frac{dB}{dt} t - \mu_0 \int_0^x \left(J_k + J_\delta \ln \frac{E}{J \rho_n} \right) dx.$$

Substituting the corresponding value $E(x, t)$ into this formula and into (7) and using simple manipulations with allowance for the relationship $x_0(t) \ll J_k \rho_n / \dot{B}$, we

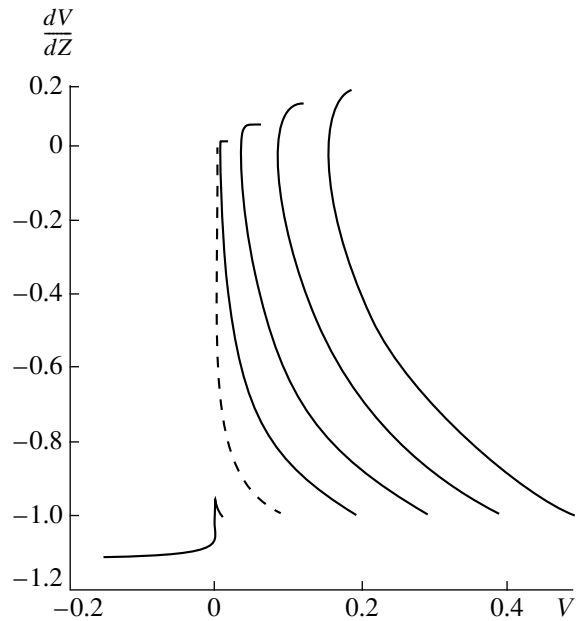


Fig. 1. Phase plane for problem (5), (6).

easily find the linear approximation for the magnetic-field induction

$$B(x, t) = \frac{dB}{dt} t - \mu_0 J_k x + \mu_0 J_\delta \left[x + (x_0 - x) \ln \frac{\frac{dB}{dt}(x_0 - x)}{J_k \rho_n (1 - \delta)} - x_0 \ln \frac{\frac{dB}{dt} x_0}{J_k \rho_n (1 - \delta)} \right] \quad (8)$$

and the law of growth for the magnetization boundary $x_0(t) = vt$ penetrating the hard superconductor with a constant velocity

$$v = \frac{\frac{dB}{dt}}{\mu_0 [J_k - 2J_\delta - J_\delta \ln(1 - J_\delta / J_k)]}. \quad (9)$$

The presented expressions enable us to find an analytical expression for the magnetic moment of a superconductor as a function of time and the rate of variation of the external magnetic field. According to linear approximation (8), (9) and in the case of incompletely penetrating screening currents into a superconducting plate with a half-width a , the desired value of the magnetic moment is

$$M(t) = \frac{1}{\mu_0} \left(\frac{1}{a} \int_0^{x_0(t)} B(x, t) dx - B_a \right) = B_a \left(\frac{x_0}{a} - 1 \right) - \mu_0 J_k \frac{x_0^2}{2a} \left[1 - 1.5\delta + 3\delta \ln \frac{\frac{dB}{dt} x_0}{J_k \rho_n (1 - \delta)} \right].$$

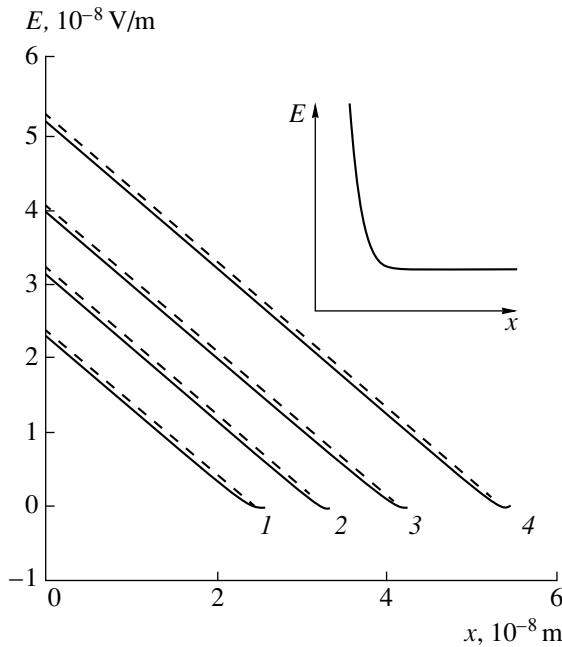


Fig. 2. Distribution of the electric-field strength inside the Nb-Ti superconductor: $t = (1) 0.9 \times 10^{-4}$ s, (2) 1.2×10^{-4} , (3) 1.5×10^{-4} , (4) 2×10^{-4} s.

It should be noted that, as was indicated previously, model (2) transforms into the critical-state model for J_{δ} , $T_{\delta} \rightarrow 0$. It is easy to verify that this passage to the limit is fulfilled for all the above-written linear approximations of the corresponding expressions describing the macroscopic pattern for the diffusion of magnetic vortices.

In order to verify the analysis performed, we carried out a certain numerical experiment. In Fig. 2, for various time moments, dashed lines present linear approximations of the spatial distribution for the strength of the electric-field induced inside the Nb-Ti superconductor by an external magnetic field varying with the rate $\frac{dB}{dt} = 1$ T/s. Here, the solid lines present the numerical results obtained on the basis of the direct solution to the nonlinear initial boundary value problem (3), (4). The initial parameters were given to be equal to

$$\rho_n = 5 \times 10^{-7} \text{ m}, \quad J_{\delta} = 4 \times 10^7 \text{ A/m}^2, \\ T_{\delta} = 0.048 \text{ K}, \quad T_c = 9 \text{ K}, \quad T_0 = 4.2 \text{ K}.$$

In the numerically solving problem (3), (4), the plate half-width was assumed to be 10^{-6} m.

In the insert to Fig. 2, we show the character of variation of the electric-field strength immediately near to the mobile boundary of the magnetization region. By virtue of the smallness of the spatial section, the figure is plotted schematically. Nevertheless, the curve presented is obtained on the basis of the numerical calcu-

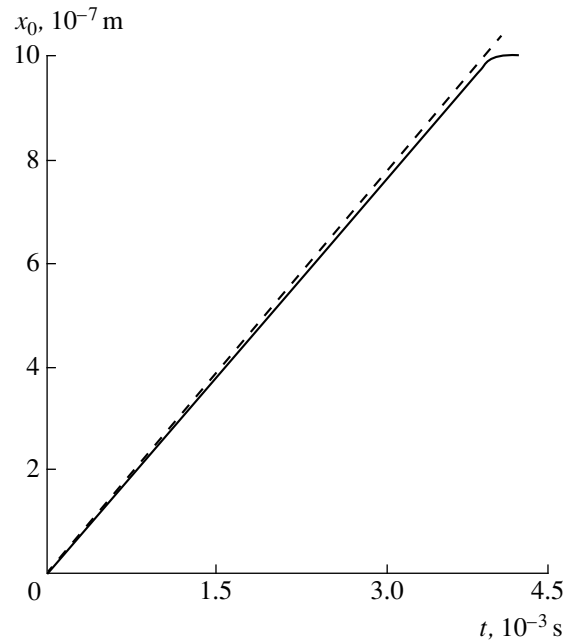


Fig. 3. Time dependence of a position for the magnetization-region front. The calculation is performed in the linear approximation (dashed line) and on the basis of the numerical solution to problem (3), (4) (solid line).

lation of problem (3), (4), which was carried out with a necessary accuracy in the neighborhood of this boundary.

In Fig. 3, the corresponding time variation of the coordinate for the magnetization-region front is shown. The appearance of the horizontal section indicates the complete penetration of the magnetic flux into the superconductor.

The results presented in Figs. 2 and 3 obviously demonstrate features of the electrodynamic behavior of a hard superconductor in the region of the magnetic-flux creep, which were formulated above.

Thus, in the case of incomplete filling of the cross section of a hard-superconductor plane-parallel plate by screening currents, the diffusion of the magnetic flux in the creep region proceeds with a constant rate as in the Bean critical-state model. Therefore, when arbitrary external perturbances act upon a hard superconductor, an electromagnetic field, which exists only within a finite region, is induced in the superconductor. Such a situation takes place even in the case when the electric-field, appearing well before the critical current has been attained, exists inside the superconductor. In this case, the spatial distributions of both the electric-field strength and the magnetic-field induction are well approximated with a good accuracy (not only qualitatively but also quantitatively) by linear dependences. However, in contrast to the critical-state model with the creep in a small neighborhood of the mobile magnetization-region front, the magnetic induction and the

electric-field strength approach smoothly unperturbed values.

ACKNOWLEDGMENTS

This work was supported by the Russian Foundation for Basic Research, project no. 98-02-16046a.

REFERENCES

1. P. W. Anderson, *Phys. Rev. Lett.* **9**, 309 (1962).
2. Yu. G. Kalmakhelidze and R. G. Mints, *Cryogenics* **29**, 1041 (1989).
3. V. M. Vinokur, M. V. Feigel'man, and V. B. Geshkenbein, *Phys. Rev. Lett.* **67**, 915 (1991).
4. H. G. Schnack and R. Griessen, *Phys. Rev. Lett.* **68**, 2706 (1992).
5. A. Gurevich and H. K pfer, *Phys. Rev. B: Condens. Matter* **48**, 6477 (1993).
6. I. L. Maksimov, V. V. Ranchin, and I. Yu. Shalaev, *Sverkhprovodimost': Fiz., Khim., Tekh.* **8**, 266 (1995).
7. A. L. Kasatkin, V. M. Pan, V. V. Vysotskiĭ, *et al.*, *Physica C* **31**, 296 (1998).
8. M. Polak, I. Hlasnik, and L. Krempasky, *Cryogenics* **13**, 702 (1973).
9. Yu. K. Krasnov, V. A. Shukhman, and L. V. Matyushkina, *Fiz. Nizk. Temp.* **5**, 109 (1979) [*Sov. J. Low Temp. Phys.* **5**, 51 (1979)].
10. G. L. Dorofeev, A. B. Imenitov, and E. Yu. Klimenko, *Cryogenics* **20**, 307 (1980).
11. V. E. Keĭlin and V. R. Romanovskiĭ, *Cryogenics* **33**, 986 (1993).
12. E. Yu. Klimenko, V. E. Kozitsyn, and N. N. Martovetskiĭ, *Dokl. Akad. Nauk SSSR* **292**, 1119 (1987) [*Sov. Phys.—Dokl.* **32**, 163 (1987)].
13. S. L. Kruglov and V. R. Romanovskiĭ, *Pis'ma Zh. Tekh. Fiz.* **20**, 89 (1994) [*Tech. Phys. Lett.* **20**, 929 (1994)].
14. V. A. Vasil'ev, V. R. Romanovskiĭ, and V. G. Yakhno, *Autowave Processes* (Nauka, Moscow, 1987).
15. L. V. Ovsyannikov, *Group Analysis of Differential Equations* (Nauka, Moscow, 1978).

Translated by V. Bukhanov

On a Relation between Strains and Vortices in Hydrodynamic Flows

V. A. Dubrovskii

Presented by Academician E.I. Shemyakin October 11, 1999

Received October 18, 1999

It is shown in paper [1] that, in the case of existence strains (i.e., nonzero strain-rate tensor), hydrodynamic flows are locally unstable everywhere with respect to eddy perturbations. To be exact, for the given strain-rate tensor

$$d_{ik} = \frac{1}{2} \left(\frac{\partial v_i}{\partial x_k} + \frac{\partial v_k}{\partial x_i} \right)$$

there is always a direction, such that a curl of velocity oriented along it grows in absolute value. This direction is determined by one or two eigenvectors corresponding to the matrix d_{ik} for one or two positive eigenvalues. In turn, the positive eigenvalues exist always due to the incompressibility condition ($\text{div } \mathbf{v} = 0$), which leads to zero trace of the matrix d_{ik} and, consequently, to the zero sum of all three eigenvalues.

As a result, the eddy flow component (the vector $\boldsymbol{\omega}$) turns out to be related to its deformation component (the tensor d_{ik}) by the Helmholtz hydrodynamic equations [2]

$$\frac{\partial \boldsymbol{\omega}_i}{\partial t} + (\mathbf{v} \nabla) \boldsymbol{\omega}_i = \frac{1}{2} \left(\frac{\partial v_i}{\partial x_k} + \frac{\partial v_k}{\partial x_i} \right) \boldsymbol{\omega}_k - \mathbf{v} \text{curl}_i \text{curl } \boldsymbol{\omega}, \quad (1)$$

$$\boldsymbol{\omega} = \text{curl } \mathbf{v},$$

that leads finally to a symmetry spontaneous violation after the instability has developed. This fact implies that symmetry of the flow under investigation changes when random origination and unstable development of new vortices occur.

It is interesting to clarify the inverse dependence of the flow deformation on the flow vorticity and to derive a system of equations determining an interdependent behavior of d_{ik} and $\boldsymbol{\omega}_i$. For this purpose, we, first, differentiate the i th and k th components of the hydrodynamic equations with respect to x_k and x_i , respectively, and

then summarize the results obtained. This yields the following equation for d_{ik} :

$$\begin{aligned} \frac{d d_{ik}}{d t} + d_{in} d_{nk} - \frac{1}{4} \omega^2 \delta_{ik} + \frac{1}{4} \omega_i \omega_k + \frac{1}{\rho} \frac{\partial^2 p}{\partial x_i \partial x_k} \\ = \frac{v \partial}{\partial x_n} \left(\frac{\partial d_{in}}{\partial x_k} + \frac{\partial d_{kn}}{\partial x_i} \right) + \frac{\partial^2 \phi}{\partial x_i \partial x_k}, \quad d_{kk} = 0, \end{aligned} \quad (2)$$

where $\frac{d}{d t} = \frac{\partial}{\partial t} + (\mathbf{v} \nabla)$, ϕ is the potential of the external force $\nabla \phi$, and the summation is performed over identical indices.

System of equations (1), (2) describes simultaneous behavior of the deformations d_{ik} and velocity curls $\boldsymbol{\omega}_i$ in hydrodynamic flows. The choice of these quantities as observable ones agrees with the general concept for equations to be invariant under the Galilean transformations. In fact, here, the observable quantities are presented by the spatial velocity gradients $\frac{\partial v_i}{\partial x_k}$ and their time derivatives $\frac{\partial v_i}{\partial t}$. At the same time, the tensor $\frac{\partial v_i}{\partial x_k}$ can be decomposed into the symmetric and antisymmetric parts:

$$\frac{\partial v_i}{\partial x_k} = \frac{1}{2} \left(\frac{\partial v_i}{\partial x_k} + \frac{\partial v_k}{\partial x_i} \right) + \frac{1}{2} \left(\frac{\partial v_i}{\partial x_k} - \frac{\partial v_k}{\partial x_i} \right).$$

These symmetric and antisymmetric parts determine deformation and vorticity of flows, respectively. Thus, both these parts are coupled by the formalized laws of conservation (1), (2).

Terms containing pressure and the external force represent disadvantage of equation (2) with respect to (1), since owing to these terms, local qualitative investigation of d_{ik} as a function of $\boldsymbol{\omega}_i$ becomes more difficult. Therefore, we start with considering a simpler case of interdependent behavior of their absolute values estimated by $d^2 = d_{ik} d_{ik}$ and $\omega^2 = \boldsymbol{\omega}_i \boldsymbol{\omega}_i$. Scalar multipli-

cation of (1) by $\boldsymbol{\omega}$ and (2) by d_{ik} (with respect to the indices i and k) yields

$$\begin{aligned} \frac{dd^2}{dt} = & -\frac{1}{2}\omega_i d_{ik} \omega_k - 2d^3 - 4v \frac{\partial d_{ik}}{\partial x_k} \frac{\partial d_{in}}{\partial x_n} \\ & + \frac{2}{\rho} \frac{\partial}{\partial x_i} \left[\frac{\partial v_i}{\partial x_k} \frac{\partial(\rho\phi - p)}{\partial x_k} + 2\rho v d_{ik} \frac{\partial d_{kn}}{\partial x_n} \right], \end{aligned} \quad (3)$$

$$\frac{d(\omega^2/4)}{dt} = \frac{1}{2}\omega_i d_{ik} \omega_k - \frac{v}{2}(\text{curl}\boldsymbol{\omega})^2 + \frac{v}{2}\text{div}[\boldsymbol{\omega} \text{curl}\boldsymbol{\omega}], \quad (4)$$

where $d^3 = d_{in}d_{nk}d_{ki}$. Equations (3) and (4) determine time dependence of squared moduli of the both strain and velocity curl on four factors, which are described by four different terms occurring in the right-hand sides of (3) and (4). The strictly negative terms proportional to the viscosity v describe dissipative processes. The divergence terms describe an additional contribution to the time variation of the velocity curl and the strain that inflows (outflows) to (from) a space point under consideration from (to) its nearest neighborhood. After integrating over volume of a closed system, these terms turn into surface integrals and disappear by virtue of boundary conditions. The terms $\omega_i d_{ik} \omega_k$ entering with opposite signs into the right-hand sides of (3) and (4) are mostly interesting. For such a term in (4) resulting in an increase (decrease) in a degree of vorticity, a similar term in (3) having the opposite sign causes a simultaneous decrease (increase) in the strain level. In other words, the terms $\omega_i d_{ik} \omega_k$ describe a nonlinear channel of energy transfer from the vortex motion to that caused by deformation and *vice versa*. As a result, the transfer intensity depends on a mutual configuration of ω_i and d_{ik} , as well as on their absolute values. Such a mutual transformation of vortex-induced and deformation-induced flows into each other represents a very important component of, to some extent, the chaotic process of flow variability. It clearly manifests itself in the analytic approach based on using the quantities d_{ik} and ω_i as observable ones. It is worth noting here that, in connection with problems of field generation in magneto-hydrodynamics and electrical hydrodynamics, nonlinear pendulum-type transformation of energy of deformation-induced flows into that of electric and magnetic fields, and vice versa was discussed previously in [4, 5]. Moreover, the transformation was described in terms of the type $A_i d_{ik} A_k$, where the vector \mathbf{A} represented either electric-field (\mathbf{E}) or magnetic-field (\mathbf{H}) intensities. It is of interest to note that certain features of uniform isotropic turbulence simulated numerically in [3] implied such a transformation. The instability caused everywhere by eddy perturbations (at a given strain), which was discussed in [1], proves to be a part of a general pendulum-type process for mutual strain-to-vortex transformation. In this case, it was noted [1] that it is basically impossible to magnetically confine the plasma in magnetohydrodynamics.

The term in (3) proportional to d^3 is of no less importance and interest. It proves to be related to the fundamental phenomenon of intermittent behavior in the problem of turbulence. This fact is analyzed below. The quantities d^2 and d^3 occurring in (3) and (4) represent contractions of the tensor d_{ik} with respect to the indices i and k , that is, scalars. Therefore, in the reference system related to the principal axes of contraction-tension, considerations of invariance allow these quantities to be substituted by the following expressions containing the principal values λ_k of the contractions tension: $d^2 = \lambda_1^2 + \lambda_2^2 + \lambda_3^2$ and $d^3 = \lambda_1^3 + \lambda_2^3 + \lambda_3^3$. With the use of the incompressibility condition $d^3 = 3\lambda_1\lambda_2\lambda_3$, the expression for d^3 can be written as $\text{div}\mathbf{v} = \lambda_1 + \lambda_2 + \lambda_3 = 0$. Taking this relation into account and combining (3) and (4) together yield

$$\begin{aligned} \frac{d}{dt} \left(\lambda_1^2 + \lambda_2^2 + \lambda_3^2 + \frac{\omega^2}{4} \right) = & -6\lambda_1\lambda_2\lambda_3 \\ & - 4v \left[\frac{\partial d_{ik}}{\partial x_k} \frac{\partial d_{in}}{\partial x_n} + \frac{1}{8}(\text{curl}\boldsymbol{\omega})^2 \right] \\ & + \frac{\partial}{\partial x_i} \left\{ \frac{v}{2} [\boldsymbol{\omega} \text{rot}\boldsymbol{\omega}]_i + 4v d_{ik} \frac{\partial d_{kn}}{\partial x_n} + \frac{2}{\rho} \frac{\partial v_i}{\partial x_k} \frac{\partial(\rho\phi - p)}{\partial x_k} \right\}. \end{aligned} \quad (5)$$

Equations (4) and (5) help us to estimate qualitatively the state of flows with respect to their deformation and vorticity. We note first that the second term in the right-hand side of (5), which contains square brackets, is always negative and determines viscous dissipation. The term with braces in (5) represents divergence and determines the inflow (outflow) of vortices and strains to (from) the point under consideration from (to) its vicinity. After integrating over volume, this term vanishes because of zero boundary conditions. Therefore, after the above-mentioned integration, we obtain from (5)

$$\begin{aligned} \frac{d}{dt} \left(\bar{\lambda}_1^2 + \bar{\lambda}_2^2 + \bar{\lambda}_3^2 + \frac{\bar{\omega}^2}{4} \right) = & -6\bar{\lambda}_1\bar{\lambda}_2\bar{\lambda}_3 - 4v \left[\frac{\partial d_{ik}}{\partial x_k} \frac{\partial d_{in}}{\partial x_n} + \frac{1}{8}(\text{curl}\boldsymbol{\omega})^2 \right]. \end{aligned} \quad (6)$$

We now consider different cases of time behavior of absolute values for both velocity curls and strains. According to (6), the time variation of the sum of squares for both the velocity curl ω^2 and the strain d^2 depends essentially on sign and value of the volume-averaged product of all three eigenvalues $\bar{\lambda}_1\bar{\lambda}_2\bar{\lambda}_3$. The sign of this product is opposite for each of the two possible local vortex structures. It is positive when dominant structures correspond to one positive and two negative eigenvalues, i.e., when vortices capable of growing have the velocity curl directed along an eigenvector

calculated for the matrix d_{ik} at the positive eigenvalue.

Then, the relations $\frac{d(\bar{d}^2 + \bar{\omega}^2/4)}{dt} < 0$ and $\frac{d\bar{\omega}^2}{dt} > 0$

yield $\frac{d\bar{d}^2}{dt} < 0$. Consequently, for flows in which one positive eigenvalue dominates (the case of tension along one of the axes), an intense growth of vortex tubes is accompanied by a decrease in strains, that is, by the energy transfer from the strains to the vortices through a channel described by the term $\omega_i d_{ik} \omega_k$. As a result, such a state cannot exist long, because this effect (development of vortex tubes) leads inevitably to liquidation of the cause (the strains).

The other possible vortex structure called a pancake-like or sheet-like one [3, 6], is associated with dominance of two positive and one negative eigenvalues. Then, the average product $\overline{\lambda_1 \lambda_2 \lambda_3}$ occurring in the right-hand side of (6) proves to be negative and the general time dependence in (5) (without taking into account the dissipative terms) becomes positive. Consequently, the growth of vortices maybe is not followed by a decrease in the degree of deformation. However, the dependence of $|\omega|$ on the corresponding positive term λ_i is stronger than a linear function [this fact results from (4)]. Therefore, the absence of decreasing the strains does not proceed long and can lead to a decrease in the deformation level. Anyhow, vortices whose positive eigenvalue is modulo intermediate and, consequently, the smallest will exist longer. As a result, flows characterized by two positive eigenvalues prove to be the most tenacious of life (although, less intense than the vortex tubes). Moreover, in this case, vortices that must become dominant in the due course have velocity curls directed along an eigenvector calculated for the matrix d_{ik} at the intermediate positive eigenvalue. The conclusions based on the investigation presented here agree with the results of numerical simulation for developed homogeneous isotropic turbulence [3, 6].

As a limiting case, we can consider a vortex motion with velocity curls directed mainly along the eigenvector corresponding to the zero eigenvalue. This case is treated in [6] as similar to two-dimensional. Here, however, an interesting problem arises. It concerns investigating a special class of solutions for which $\det(d_{ik}) = 0$. Because of this condition, the system of equations for v_i and p [equations (1) and (2)] becomes overdetermined that often corresponds to the continuity breakdown. In solids, a special class of solutions can be associated with the development of instability leading to fissuring.

Finally, it is of interest to consider the case of quasi-steady (on the average) developed vortex flows of a low-viscosity fluid. Then, the quantity $\overline{\lambda_1 \lambda_2 \lambda_3}$ appear-

ing in the right-hand side of (6) must be equal to zero. This implies such a flow pattern at which both possible above-discussed vortex structures (with $\lambda_1 \lambda_2 \lambda_3 > 0$ and $\lambda_1 \lambda_2 \lambda_3 < 0$, respectively) exist in space and time. They alternate with each other, i.e., vortex tubes with intense periodic vortex motion give place to less intense plane pancake-like structures. These facts reveal a cause of intermittent behavior (alternation) representing the fundamental feature of developed turbulence and discovered previously by experimental and numerical modeling [3, 6, 7]. On the other hand, in the closed systems, zero value of the time derivative occurring in is caused by intermittent behavior of the two alternative flow structures, which are characterized by opposite signs of the product $\lambda_1 \lambda_2 \lambda_3$. Consequently, the approach based on using the strains d_{ik} and the velocity curls ω_i as observable quantities reveals the fundamental fact that the intermittent behavior causes conservation of the sum of squares of both the strains and velocity curls and vice versa. This new law of conservation is important for theory of developed quasi-steady turbulence.

We note in conclusion that, since the terms $\omega_i d_{ik} \omega_k$ and $\lambda_1 \lambda_2 \lambda_3$ occurring in (4) and (5) vanish in the two-dimensional case, the two effects revealed here are three-dimensional in principle. They exhibit the nonlinear pendulum-type energy exchange between vortices and strains and the fact that conservation of the sum of squares of velocity curls and strains relates to the totally intermittent behavior ($\overline{\lambda_1 \lambda_2 \lambda_3} = 0$). Both effects lead inevitably to three-dimensional chaos. However, because of causality existing always between vortices and strains, this chaos is ordered to some extent. Numerical simulation of developed homogeneous turbulence, which was carried out in [6], revealed a certain organization of turbulent chaos as well.

REFERENCES

1. V. A. Dubrovskiĭ, Dokl. Akad. Nauk **356**, 36 (1997) [Phys.-Dokl. **42**, 464 (1997)].
2. N. E. Kochin, I. A. Kibel', and N. V. Roze, *Theoretical Fluid Mechanics* (OGIZ, Leningrad, 1948), Vol. 2.
3. Z.-S. She, E. Jackson and S. A. Orszag, Nature **344** (6263), 226 (1990).
4. V. A. Dubrovskiĭ, Dokl. Akad. Nauk SSSR **286**, 74 (1986).
5. V. A. Dubrovskiĭ and N. N. Rusakov, Dokl. Akad. Nauk SSSR **306**, 64 (1989).
6. A. Vincent and M. Meneguzzi, J. Fluid Mech. **225**, 1 (1991).
7. L. D. Landau and E. M. Lifshits, *Hydrodynamics* (Nauka, Moscow, 1986).

Translated by Yu. Verevochkin

Fractal Dimensionality of a Surface as an Order Parameter

Ya. L. Kobelev*, L. Ya. Kobelev*,
and Corresponding Member of the RAS E. P. Romanov**

Received July 12, 1999

Many properties of solids (including properties of their surfaces) can be described on the basis of experimental and theoretical studies of fractal dimensionality for crystallite surfaces. This description is based on an assumption, confirmed experimentally, that the distribution of surface clusters consisting mainly of atoms composing the crystallite surface is governed by fractal-geometry laws [1]. Many physical properties for a set of atomic clusters on a surface of a polycrystal and on crystallite surfaces inside a polycrystal can be described, in a rather good approximation, as properties of fractal sets (which are represented by these clusters). In the last decade, as a result of a large number of physical and materials-technology studies [2], the concept of a fractal dimensionality for these sets has become a new physical characteristic of solids, which is associated with their strength, friability, kinetics of cracking, and roughness of their surfaces. This characteristic depends on temperature, pressure, as well as both conditions and duration of crystallite growth, etc. and is widely used for describing physical properties in solid-state physics, materials technology, and other fields of physics. Nevertheless, in the majority of papers we know, when theoretically describing the dependence of physical effects on the fractal dimensionality, the authors treat it as a parameter to be found experimentally. However, the fractal dimensionality has been found in a number of experiments to depend on temperature, both conditions and duration of growth of polycrystals [3], shock pressure [4], etc.

The goal of this paper is to construct a phenomenological theory for the dependence of the fractal dimensionality of crystallite surfaces on physical quantities such as temperature, duration of growth, pressure, etc. In this case, the fractal dimensionality for a surface should be considered (by analogy with the paper [5], in which the fractal dimensionality was treated as an order parameter appearing in a fractal set of space-time

points) as a new order parameter. This parameter appears in the process of self-organizing clusters of surface atoms in the case of varying both internal and external crystallite parameters. This approach is similar to the well-known Ginzburg–Landau theory [6] of order parameters and allows us to describe fairly completely the phenomenological dependence of the fractal dimensionality of crystallite surface on arbitrary physical parameters.

FRACTAL DIMENSIONALITY AS AN ORDER PARAMETER

1. We denote as $d(r, t)$ the local fractal dimensionality of a crystallite surface. Following [5], we consider this quantity as a function of the potential interaction energy of ions and electrons forming the surface and those inside the crystallite, which influence formation of the fractal distribution of surface clusters. Employing methods of statistical physics (since the surface is formed by a macroscopic number of atoms), we can present, in the final analysis, the physical quantities such as pressure, temperature, duration of growth, etc. as sums of the potential interaction energies of atoms and electrons. In a phenomenological theory, a microscopic nature of the physical quantities characterizing crystallite properties can be ignored. Thus, these quantities can be substituted into the Ginzburg–Landau free-energy functional as parameters, namely, the pressure P_i , temperature T , time t (or the surface growth duration), the crystallite mean surface area S_0 , etc. We denote as P_i and S_i ($i = 1, 2, 3, \dots$) physical quantities of two types; namely, P_i are the physical quantities varying with S_i , and S_i are those determining the dynamics (in the S_i space) for the dependence of the fractal dimensionality on P_i in the case under consideration. The choice of P_i and S_i is conditional and is dictated by the type of experiments studying the dependence of the fractal dimensionality on various physical quantities. The pressure, time, etc. can be chosen as P_i , while time and mean increment of the area (per unit time) for the growing crystallite surface, etc. can be chosen as S_i .

2. Taking into account the aforesaid and assuming that the fractal dimensionality of the surface appears as

* Ural State University,
pr. Lenina 51, Yekaterinburg,
620083 Russia

** Institute of Metal Physics, Ural Division,
Russian Academy of Sciences,
ul. S. Kovalevskoi 18, Yekaterinburg, 620219 Russia

an order parameter [6] (i.e., as a phase transition), we write out the free-energy functional in the form (the vertical dash separates out the functional dependence)

$$F(|d(r, t)) = \int_{P_i} dP_i f\left(S_i, P_i, d, \frac{\partial d}{\partial P_i}, \dots\right). \quad (1)$$

For small values of d and its derivatives with respect to P_i , we expand the integrand of (1) in a series and rewrite (1) in the form

$$F(|d(r, t)) = F_0 + \int_{P_i} dP_i \left\{ a_i(P_i, S_i) \frac{\partial d}{\partial P_i} + b_i(P_i, S_i) \left(\frac{\partial d}{\partial P_i}\right)^2 + kd + \frac{1}{2}(\varphi - \varphi_0)d^2 + \frac{1}{3}k'd^3 + \dots \right\}. \quad (2)$$

Here, P_i is one of crystallite physical parameters; φ is a function of the parameters (P_i, S_i) that are determined by potentials of electrons and ions on the surface and, in turn, determine the energy advantage in the case of the origination of a fractal structure on the surface for $\varphi < \varphi_0$; and a_i, b_i , etc. are functions of P_i and S_i (in a nonlinear case, they are functions of d).

MINIMUM PRINCIPLE OF THE FRACTAL DIMENSIONALITY. EQUATIONS FOR THE FRACTAL DIMENSIONALITY

1. We now employ the minimum principle of the fractal dimensionality (which was first proposed in [5]) for functional (2). This principle requires that the fractal dimensionality must have a minimum for all realizable states of the fractal system under consideration. To find the fractal dimensionality of d and its parametric dependence, we vary functional (2) with respect to d , equate the variation to zero, and obtain, as a result, the equations

$$2 \frac{\partial}{\partial P_i} \left[b_i(P_i, S_i) \frac{\partial d}{\partial P_i} \right] + (\varphi - \varphi_0)d + k_1 d^2 + \left(k + \frac{\partial a_i(P_i, S_i)}{\partial P_i} \right) = 0 \quad (3)$$

and the boundary conditions

$$\left[b_i(P_i, S_i) \frac{\partial d}{\partial P_i} + \frac{\partial a_i(P_i, S_i)}{\partial P_i} \right]_{P_{0i}}^{P_i} = 0. \quad (4)$$

2. If d depends explicitly on S_i , equation (3) takes the form

$$\frac{\partial d}{\partial S_i} = \frac{\partial}{\partial P_i} \left[A(P_i) \frac{\partial d}{\partial P_i} \right] + (\varphi - \varphi_0)d + k_1 d^2 + k(P_i, S_i). \quad (5)$$

The choice of terms to be kept in the expansion of the functional is determined by physical conditions of the problem under consideration. When the relaxation term and that containing k are disregarded, with both $\varphi - \varphi_0$ and nonlinear terms being small, equation (3) transforms into the diffusion equation

$$\frac{\partial d}{\partial S_i} = 2 \frac{\partial}{\partial P_i} \left[b_i(P_i, S_i) \frac{\partial d}{\partial P_i} \right] \quad (6)$$

in the (S_i, P_i) space.

The dependence of the fractal dimensionality (treated as an order parameter) of a crystallite surface on various physical quantities is described, in the above approximations, by equations similar to diffusion ones. Particular cases of this problem were analyzed to describe the dependence of the fractal dimensionality for a growing crystal on the growth duration [7] or on shock pressure [8]. In these cases, either the variation (per unit time) of the mean area of a growing crystallite or its mean area was taken as S_i , while the time or the pressure was taken as P_i .

3. Two arguments are worth noting. Firstly, if the system memory is taken into account, equation (3) can be written out in terms of the Riemann–Liouville fractional derivatives [9] or the generalized fractional derivatives [5]. Secondly, a similarity to the Ginzburg–Landau method will be enhanced if the complex field $\psi(P_i, S_i)$, which defines d by the relation $d = \psi^* \psi$, rather than the fractal dimensionality of d , is taken as an order parameter. In the latter case, we assume d to be real, choose the other dependence of the free-energy functional on ψ and ψ^* with $k = 0$ and vary the functional with respect to ψ^* . As a result, instead of (4), we obtain the equation similar to the Landau–Ginzburg equation of the phenomenological superconductivity theory

$$\frac{\partial \psi}{\partial S_i} = \frac{\partial}{\partial P_i} \left[A(P_i) \frac{\partial \psi}{\partial P_i} \right] + (\varphi - \varphi_0)\psi + k_1 \psi d = 0. \quad (7)$$

Almost all of the qualitative conclusions, following from equations (3) and (7), which relate to the behavior of d , are identical. In particular, for small $\varphi - \varphi_0$, provided that the diffusion contributions, an explicit dependence of d on S_i , and the constant term are ignored, the fractal dimensionality of the crystallite surface is governed by the equation

$$d \sim (\varphi_0 - \varphi). \quad (8)$$

4. A number of particular cases of equation (3) was given in [10]. We now consider the dependence of the function $\varphi - \varphi_0$ on potentials of physical fields determining the surface structure of a solid body. As far as the fractal structure of the surface is completely determined by the electronic and ionic states of the crystallite, the function $\varphi - \varphi_0$, within the framework of statistical concepts (classical or quantum), is a functional of the density distribution for electrons and ions in the crystallite. The function $\varphi(\mathbf{r}, t | n_e, n_i)$ can depend on

either the mean kinetic energy of electrons and ions [i.e., on temperature: $\varphi - \varphi_0 \sim T(r, t) - T_0(r, t)$] or on the mean potential energies of interacting electrons and ions [which are expressed in terms of the electron and ion density distributions, for example,

$$\varphi - \varphi_0 \sim \int [(V_e(r - r_1)n_e(r_1, t) - (V_i(r - r_1)n_i(r_1, t))]dr_1$$

etc.], or on other combinations of the electron and ion potentials determining the formation of a fractal set of clusters on the crystallite surface. These combinations allow for the interaction between electrons and ions and are expressed, ultimately, in terms of the variables P_i . The choice of the distribution functions $n_e(r, t)$ and $n_i(r, t)$ is determined by either corresponding models (quantum-mechanical, statistical, etc.) of solid-state physics, which describe physical properties of the crystallite surface. In other approaches, these functions are given by kinetic equations for open systems (see, e.g., [11]). In the phenomenological theory, this procedure yields the choice of the function $\varphi - \varphi_0$. It should be kept in mind that the choice of the fractal-dimensionality normalization must take into account the fact that the crystallite-surface dimensionality is equal to two if a fractional part of the fractal dimensionality is absent.

5. Equations for the density of electrons and ions of a surface containing fractal structures must depend on the local fractal dimensionality $d(\mathbf{r}, t)$. Therefore, the set of equations for $d(\mathbf{r}, t)$ and $n(\mathbf{r}, t)$ is a consistent system for describing fractal properties of a surface. In kinetic equations for $n(\mathbf{r}, t)$, the fractal dimensionality can be introduced by using the mathematical method of generalized fractional derivatives, which was proposed in [5]. This method makes it possible to estimate not only the dependence of the fractal dimensionality on physical parameters but to allow for the influence of the fractal dimensionality originated on the behavior of electrons and ions on the surface. Kinetic equations for large systems containing fractal structures are given in [12].

Thus, the interpretation of appearance of the fractal dimensionality of crystallite surfaces as a phase transition results in a new order parameter (fractal dimensionality). It is determined by the atomic-cluster distribution on the crystallite surface and allows the well-

developed mathematical method of the Ginzburg–Landau theory of order parameters [6] to be employed for describing the fractal dimensionality as a function of physical characteristics (internal and external) of the crystallite. The method of thermodynamic flows, which was used in [7, 8]), is a particular case of the problem of the fractal dimensionality. In the method under consideration, the fact that the derivatives in equations (3) for the fractal dimensionality are fractional can be taken into account by replacing integer derivatives by the generalized fractional ones used in [5].

REFERENCES

1. B. B. Mandelbrot, *The Fractal Geometry of Nature* (Freeman, New York, 1982).
2. V. S. Ivanova, A. S. Balankin, I. Zh. Bunin, and A. A. Oksogoev, *Synergetics and Fractals in Materials Technology* (Nauka, Moscow, 1994).
3. V. Ya. Shur, S. A. Negashev, A. L. Subbotin, *et al.*, *Mater. Res. Soc. Symp. Proc. Ser.* **433**, 521 (1996).
4. P. V. Korolev and S. N. Kul'kov, *Perspekt. Materialy*, No. 3, 21 (1997).
5. L. Ya. Kobelev, *Fractal Theory of Time and Space* (Konross, Yekaterinburg, 1999).
6. V. L. Ginzburg and L. D. Landau, *Zh. Éksp. Teor. Fiz.* **20**, 1064 (1948).
7. V. L. Kobelev and L. Ya. Kobelev, in *Proceedings of Ninth International Meeting on Ferroelectricity, Seoul, Korea, 1997* (Seoul, 1997), p. 10.
8. V. L. Kobelev, E. P. Romanov, L. Ya. Kobelev, *et al.*, *Fiz. Met. Metalloved.* **85** (4), 54 (1988).
9. S. G. Samko, A. A. Kilbas, and O. I. Marychev, *Integrals and Derivatives of Fractional Order and Their Certain Applications* (Nauka i Tekhnika, Minsk, 1987).
10. Ya. L. Kobelev, L. Ya. Kobelev, and E. P. Romanov, Available from VINITI, no. 1668-B99 (Yekaterinburg, 1999).
11. Yu. L. Klimontovich, *Statistical Theory of Open Systems* (Yanus, Moscow, 1995; Kluwer, Dordrecht, 1995), Vol. 1.
12. L. Ya. Kobelev, Ya. L. Kobelev, and E. P. Romanov, Available from VINITI, no. 1667-B99 (Yekaterinburg, 1999).

Translated by V. Chechin

Plastic Deformation of Structurally Inhomogeneous Martensite in γ -Manganese Alloys after FCC–FCT Transformation

E. Z. Vintaikin and G. I. Nosova

Presented by Academician Yu.A. Osip'yan May 21, 1999

Received May 21, 1999

In γ -manganese alloys, whose FCC-structure is stabilized by copper additives, FCC–FCT martensite transformation takes place in the case of a considerably large manganese content [1]. As manganese is dissolved (up to 70%), a martensite transformation is completely suppressed in homogeneous alloys. A metastable region of segregation [2], which makes it possible to obtain isomorphous nanocrystalline γ_1 and γ_2 phases, enriched and depleted by manganese, exists in Mn–Cu system. The phase segregation extends the range of martensite transformation. In this case, martensite shears involve regions both enriched and depleted by manganese, so that, as a result of the transformation, two martensite nanocrystalline FCC-phases are formed with a various degree of manifesting tetragonal properties. As a result of the martensite transformation, a twinned structure, containing thin and rough twins, forms in the bulk of the alloy, with sizes of these twins being, approximately, 1 and 10 μm , respectively. The boundaries of thin twins are parallel to the $\{110\}$ -type planes, and the tetragonal c -axes in neighboring crystals are mutually perpendicular. The rough twins contain colonies of thin twins. The boundaries of rough twins are $\{110\}$ planes inclined at an angle of 60° to boundaries of thin twins [3].

Such a structure admits a possibility of plastic deformation by two mechanisms, namely, by twinning and usual slipping along the $\{111\}$ -type planes in $\langle 1\bar{1}0 \rangle$ direction. In the latter case, the noticeable hardening of alloys occurs [4] owing to the phase segregation accompanied by formation of nanocrystalline disperse phases and appearance of lattice distortions due to the various degree of manifesting tetragonal properties in the phases. This fact can be a cause of a number of features in which the shape-memory effect manifests itself. In this paper, conditions for realization of the

deformation by twinning in various variants of martensite crystals are analyzed. Critical shear stresses of twinning and slipping in microvolumes are also determined as a result of studies of single-crystal mechanical properties.

Under the FCC–FCT transformation, the volume of the alloy changes negligibly, and we can consider the parameters of the tetragonal lattice to be $c = a_0(1 - 2\delta)$ and $a = a_0(1 + \delta)$, the degree of manifesting tetragonal properties is $1 - c/a = 3\delta$ and depends on temperature. We assume that the transformation deformation is of the Bain nature, and the twinning (in the case of invariant lattice) is an additional deformation.

A fragment of the twinned structure after the FCC–FCT transformation with two variants ($V1$ and $V2$) of rough twins is shown in Fig. 1.

In thin $V1(C\parallel OY)$ and $V1(C\parallel OZ)$ twins composing $V1$ twins, shears take place, which are determined by the $D1(YZ)$ and $D1(ZY)$ matrices: for $V1(C\parallel OY)$

$$D1(YZ) = \begin{pmatrix} 0 & 0 & 0 \\ 0 & -2\delta & 0 \\ 0 & 0 & 2\delta \end{pmatrix},$$

for $V1(C\parallel OZ)$

$$D1(YZ) = \begin{pmatrix} 0 & 0 & 0 \\ 0 & \delta & 0 \\ 0 & 0 & -\delta \end{pmatrix}$$

and the general (rough) shear is

$$D1(ZX) = \begin{pmatrix} \delta & 0 & 0 \\ 0 & 0 & 0 \\ 0 & 0 & -\delta \end{pmatrix}.$$

In thin $V2(C\parallel OZ)$ and $V2(C\parallel OX)$ twins corresponding to the $V2$ variant, the following shears take place:

*Institute of Metal Physics and Functional Materials,
Bardin Central Research Institute
for the Iron and Steel Industry,
Vtoraya Baumanskaya ul. 9/23, Moscow, 107005 Russia*

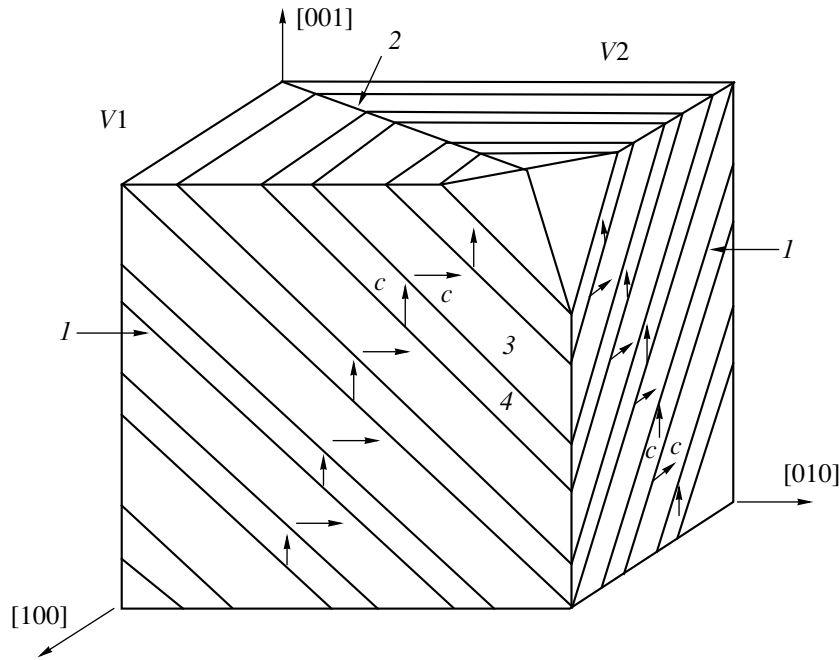


Fig. 1. Fragment of a twinned structure in the alloy under study for two variants (V1 and V2) of rough twins: (1) the boundaries of thin twins; (2) the boundary of rough twins; (3) the V1(C||OY) variant of a thin twin; (4) the V1(C||OZ) variant of a thin twin. The direction of tetragonal *c*-axis is indicated by the arrow.

for V2(C||OZ)

$$D2(ZX) = \begin{pmatrix} \delta & 0 & 0 \\ 0 & 0 & 0 \\ 0 & 0 & -\delta \end{pmatrix},$$

for V2(C||OX)

$$D2(XZ) = \begin{pmatrix} -2\delta & 0 & 0 \\ 0 & 0 & 0 \\ 0 & 0 & 2\delta \end{pmatrix}$$

and the general (rough) shear is

$$D2(XZ) = \begin{pmatrix} 0 & 0 & 0 \\ 0 & \delta & 0 \\ 0 & 0 & -\delta \end{pmatrix}.$$

The boundary between the V1 and V2 rough twins is the (11̄0) plane, the (011) and (101) planes being the boundaries of thin twins in V1 and V2, respectively.

Under compression deformation along OZ-axis in a V1(C||OY) thin twin, the twinning shear equal to -2D1(YZ) occurs, so that a jump of the tetragonal axis

to the C||OZ position takes place. In this case, the boundaries of thin twins shift into V1(C||OY) twins. As is seen from Figs. 1 and 2, the direction [011̄] is the shear direction for (011) planes. The twinned shear indicated can be extended to a V2(C||OX) twin but cannot be realized in V2(C||OZ) owing to the incompatibility of twinned systems. As is seen from Fig. 2, this shear can be carried out in V2(C||OZ) by slipping along two systems, namely, (111) [011̄] and (1̄11) [011̄], i.e., with the same directions of slipping coinciding with the direction of the twinned shear. In the case of equal initiation of two slipping systems, the efficient slipping plane (of the zig-zag shape in the cross section) coincides with the (011) twinning plane, i.e., a nearly complete accommodation of slipping and twinning is observed.

Under compression along the OY-axis in V1(C||OZ), the -2D1(ZY) shear passing into a V2 twin occurs. A similar situation takes place also under compression along the OX-axis when the twinning deformation, starting in a V2 rough twin as a result of the presence of twinning boundaries in it, passes to a V1 twin.

The deformation under both compression and tension for other variants of martensite crystals can be considered in a similar way. This allows us to carry out the averaging with respect to different orientations and derive the following equations for compression and

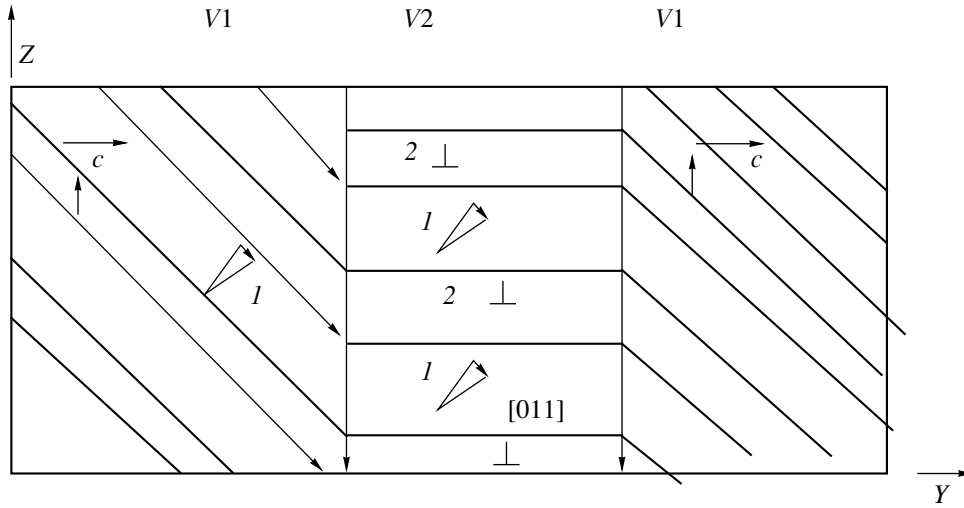


Fig. 2. Deformation by: (1) twinning and (2) dislocation slipping in V1 and V2 rough twins under compression along the OZ-axis of a single crystal. [Section by the (100) plane.]

tension along [001], when two mechanisms are realized in common:

$$0.055 \frac{\tau_s}{f_s} + 0.945 \frac{\tau_t}{f_t} = \sigma_c,$$

$$0.445 \frac{\tau_s}{f_s} + 0.555 \frac{\tau_t}{f_t} = \sigma_t.$$

Here, τ_s and τ_t are critical shear stresses for slipping (in {111} $\langle 1\bar{1}0 \rangle$ system) and twinning (in {101} $\langle 1\bar{1}0 \rangle$), where f_s and f_t are the Schmit factors for slipping (0.41) and twinning (0.5); σ_c and σ_t are the normal stresses at the yield initial stage under compression and tension of single crystals along $\langle 100 \rangle$, respectively. As is seen from these equations, for determination of crystal shear stresses, it is sufficient to carry out mechanical tests with the determination of yield stress under compression and tension.

Mechanical tests were carried out with single crystals of 75% Mn–25% Cu alloy, which were grown by the Bridgman method. Dendrite liquation in the crystals was virtually eliminated by long-lasting annealing at 800°C for 150 h in the argon ambient. The samples for compression or tension tests, which had been made respectively, in the shape of parallelepipeds with the size of $10 \times 5 \times 5 \text{ mm}^3$ or with the operating part $10 \times 4 \times 2 \text{ mm}^3$ and heads for mounting in holders, were fabricated by the oriented electric-spark saw. The [100] and [111] crystallographic directions were chosen as the load axes. The heat treatment included quenching at 800°C and annealing at 450°C for 2 h, when the phase segregation occurred. The mechanical tests were performed with the “Instron” test machine at room temperature (when the degree of tetragonal properties attained $1 - c/a = 0.03$) at the strain rate of 0.5 mm/min.

The results of mechanical tests for single crystals are shown in Fig. 3. Both under compression and tension along the [001] direction, we have observed a plateau of slight yield (such a plateau was not observed for the deformation along the [111] direction). We can see that the plateau of the slight yield in the tension curve is higher by the factor of 1.5 to 2 than for compression in the [100] direction. The substitution of the corre-

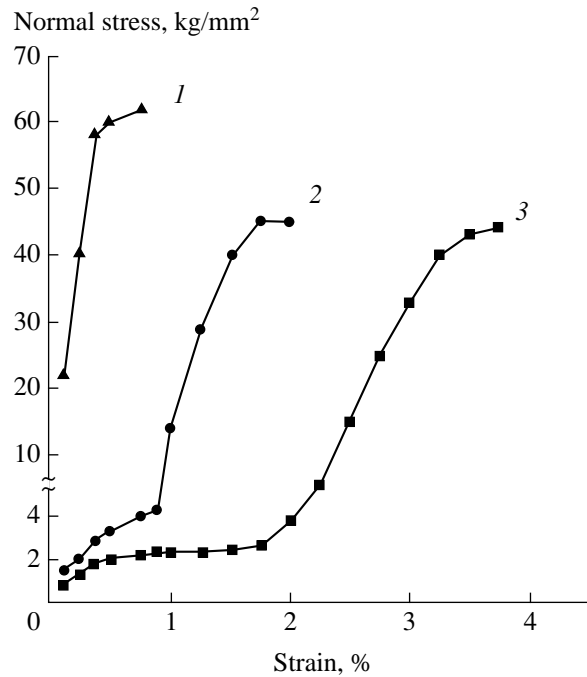


Fig. 3. Stress–strain curves for single crystals of 75% Mn–25% Cu alloy quenched and annealed at 450°C for 2 h: (1) compression deformation along the [111] direction; (2) tension along the [001] direction; (3) compression along the [001] direction.

sponding values into equations leads to the following result: $\tau_s = 2.6$ and $\tau_t = 1.0$ kg/mm².

It seems to be unexpected that the critical shear stresses of the accommodation slipping turned out to be very low. They are nearly by the order of magnitude lower than those fixed in the region of the hard yield, when possibilities of twinning processes were exhausted. In this case, the critical shear stress for slipping, which was calculated according to the curves of deformation along the [111] and [001] directions, turned out to be equal to 17 kg/mm².

The slight dislocation motion in the martensite at the initial stage of plastic deformation is likely caused by accommodation stresses arising in the course of transformation in the slipping regions and, owing to the load applied, directed along the shear stresses. Another cause of this light plastic deformation occurring in the microvolume under consideration can be associated with a possible passing by dislocations around the nanoparticle distortion fields formed as a result of phase segregation.

It is worth noting that the experimental result obtained makes it possible to understand a number of features in kinetics of martensite transformations, in particular, an extraordinary small hysteresis of FCC–FCT martensite transformation in alloys containing manganese.

As is well known, the hysteresis of direct and inverse transformations is determined by a stored energy of plastic strain, while growing crystals of a new phase. A small magnitude of slipping stresses determines the small work of the accommodation plastic deformation, and, consequently, small temperature hysteresis of the martensite transformation in γ -Mn alloys.

ACKNOWLEDGMENTS

This work was supported by the Russian Foundation for Basic Research, project no. 98-02-16795.

REFERENCES

1. A. I. Bichinashvili, E. Z. Vintaikin, D. F. Litvin, *et al.*, *Fiz. Met. Metalloved.* **41**, 130 (1976).
2. E. Z. Vintaikin, V. B. Dmitriev, and V. A. Udovenko, *Fiz. Met. Metalloved.* **46**, 790 (1978).
3. Z. S. Basinski and J. W. Christian, *J. Inst. Metals* **80**, 658 (1951/1952).
4. E. Z. Vintaikin, G. I. Nosova, D. F. Litvin, *et al.*, *Fiz. Met. Metalloved.* **84**, 161 (1997) [*Phys. Met. Metallogr.* **84**, 316 (1997)].

Translated by T. Galkina

TECHNICAL
PHYSICS

Solving Problems of the Optimum Control on the Basis of Atomic Functions

V. F. Kravchenko*, A. A. Kuraev**,
and Corresponding Member of the RAS V. I. Pustovoit***

Received October 19, 1999

A problem of optimum control or a boundary value problem can be reduced to a multiparameter optimization with a given performance criterion (goal function). To do this, a multiparameter approximation for the desired control function in the problem of the optimum control (or the boundary being optimized in the boundary value problem) should be preliminarily introduced [1–4]. Such an approximation must be performed within a class of functions satisfying *a priori* all the constraints to the problem under consideration. The choice of this class significantly affects the successful solving of the problem. Here, a restriction most frequently met is the requirement of smoothness (i.e., of infinite differentiability). This requirement is satisfied by atomic functions that are highly flexible and convenient for any approximation [5–10].

SETTING UP THE PROBLEM OF THE OPTIMUM CONTROL OF A DYNAMIC PROCESS

To prevent the subsequent solutions from becoming too cumbersome, we dwell on the simplified version of the optimum-control problem, in which: (a) the left endpoint of phase trajectories is mobile; (b) their right endpoint is free (constraints are introduced into the general functional, i.e., into the goal function); (c) the state-variables vectors and control vectors are continuous; and (d) the interval of motion T_0 is specified. Solving of this problem allows us to adequately illustrate fundamental features of the method proposed. Extending the method to the general case also presents no particular problem [3, 4]. For the conditions indicated, the problem of the optimum control is posed as follows.

* Institute of Radio Engineering and Electronics,
Russian Academy of Sciences,
Mokhovaya ul. 11, Moscow, 103907 Russia

** Belarussian State University of Information Science
and Radio Engineering,
ul. Brovki 17, Minsk, 220072 Belarus

*** Central Design Bureau of Unique Instrumentation,
Russian Academy of Sciences,
ul. Butlerova 15, Moscow, 117342 Russia

(I) A mathematical model for a dynamic process is specified in the form of ordinary differential equations (equations of state)

$$\frac{dX_s}{dT} \triangleq \dot{X}_s = f_s[X_1, X_2, \dots, X_s, \dots, X_n, \\ g_1(T), \dots, g_k(T), M_1, \dots, M_l, T], \quad (1) \\ s = 1, 2, \dots, N, \quad 0 \leq T \leq T_0,$$

or, in the vector form,

$$\frac{dX}{dt} \triangleq \dot{X} = f_s[X, g(T), M, T].$$

Here, $X = (X_1, X_2, \dots, X_n)^T$ is the n -dimensional (transposed) vector of phase variables, $g(T) = (g_1, g_2, \dots, g_m)^T$ is the m -dimensional control vector for the interaction process, M are its control parameters, and T is the reduced space length or reduced interaction time for the process development.

(II) The boundary conditions are specified at the left endpoint for $T = 0$ as

$$X_s(0) = X_s(\mathbf{B}), \quad (2)$$

where $\mathbf{B} = (B_1 \dots B_j \dots B_c)^T$ are the parameters of the initial conditions for the process.

(III) The goal function for the problem is specified in the form of the functional (the Boltz problem)

$$J = \Phi(\mathbf{X}(T_0)) + \int_0^{T_0} f_{n+1}(\mathbf{X}, \mathbf{g}, \mathbf{M}, T) dT. \quad (3)$$

We formulate the problem of the optimum control in the following form: among the parameters \mathbf{M} and \mathbf{B} and continuous functions $X_s(T)$ ($s = 1, 2, \dots, n$) and $g_k(T)$ ($k = 1, 2, \dots, m$) satisfying equations (1) in the interval $[0, T_0]$ and satisfying boundary conditions (2) at $T = 0$, we should find those for which functional (3) attains its extremum.

APPROXIMATION OF THE CONTROL

We approximate the desired control function in the following manner:

$$q_k^N(T) = \sum_{i=1}^N A_{ki} \text{up}\left(\frac{T - T_{ki}}{\rho_{ki}}\right). \quad (4)$$

Here, T_{ki} is the translation parameter, ρ_{ki} is the parameter of the width for the function $\text{up}(z)$, and $T_{ki}/\rho_{ki} \in [0, T_0]$. The function $\text{up}(z)$ (atomic function) is defined as a finite solution to the equation (see [5–10])

$$\text{up}'(z) = 2\text{up}(2z + 1) - 2\text{up}(2z - 1). \quad (5)$$

Fast-calculation methods for the function $\text{up}(z)$ are given in [5–10]; in particular, tables for $\text{up}(z)$ are presented in [5]. The tables providing the appropriate accuracy by interpolation are most reasonable for using in calculations. After solving the Cauchy problem (1), (2) and using (4), functional (3) becomes a function of $3N \times m$ parameters: A_{ki} , T_{ki} , ρ_{ki} , \mathbf{M} , and \mathbf{B} . The minimum of this function can be found by one of the methods for minimizing functions of many variables. When gradient methods are applied to minimize J , the components of the gradient of J , in accordance with the theory developed in [1–4], are determined in the following way:

$$\begin{aligned} \frac{\partial J}{\partial B_j} &= - \sum_{s=1}^N \frac{\partial X_{0s}}{\partial B_j} \lambda_s(0), \quad j = 1, 2, \dots, c, \\ \frac{\partial J}{\partial M_i} &= - \int_0^{T_0} \frac{\partial H}{\partial M_i} dT, \quad i = 1, 2, \dots, l, \\ \frac{\partial J}{\partial A_{ki}} &= - \int_{T_{ki} - \rho_{ki}}^{T_{ki} + \rho_{ki}} \frac{\partial H}{\partial q_k} \text{up}(z_{ki}) dT, \\ \frac{\partial J}{\partial T_{ki}} &= \frac{2}{\rho_{ki}} \left[\int_{T_{ki} - \rho_{ki}}^{T_{ki}} \text{up}(2z_{ki} + 1) dT \right. \\ &\quad \left. - \int_{T_{ki}}^{T_{ki} + \rho_{ki}} \text{up}(2z_{ki} - 1) dT \right], \\ \frac{\partial J}{\partial \rho_{ki}} &= \frac{2}{\rho_{ki}} \left[\int_{T_{ki} - \rho_{ki}}^{T_{ki}} z_{ki} \text{up}(2z_{ki} + 1) dT \right. \\ &\quad \left. - \int_{T_{ki}}^{T_{ki} + \rho_{ki}} z_{ki} \text{up}(2z_{ki} - 1) dT \right], \\ k &= 1, 2, \dots, m, \quad i = 1, 2, \dots, N. \end{aligned} \quad (6)$$

Here,

$$I = J + \int_0^{T_0} \sum_{s=1}^n \lambda_s \varphi_s dT,$$

$$\varphi_s = \dot{X}_s - f_s(X_s, g_k, M_i, T)$$

is the Hamiltonian function; the Lagrange multipliers $\lambda_s(T)$ (i.e., variables conjugated according to Hamilton) are determined from the following boundary value problem:

$$\dot{\lambda}_s + \frac{\partial H}{\partial X_s} = 0, \quad s = 1, 2, \dots, n, \quad (7)$$

$$\lambda_s(T_0) = - \frac{\partial \Phi}{\partial X_s(T_0)}, \quad s = 1, 2, \dots, n. \quad (8)$$

THE SCHEME OF THE ITERATIVE PROCEDURE

We suppose that in the course of minimizing J , a point $(B_j^{(n)}, M_i^{(n)}, A_{ki}^{(n)}, T_{ki}, \rho_{ki}^{(n)})$ is attained in the space of the parameters being optimized. In this case:

(i) System (1) is solved with the indicated values of the parameters and boundary conditions (2) with allowance for equation (4);

(ii) The boundary conditions for $\lambda_s(T_0)$ are determined in accordance with (8);

(iii) Going from the left to the right (i.e., from T_0 to 0 in terms of the T variable), systems of equations (1) and (7) are solved simultaneously. At the same time, the components of the gradient of J are determined in accordance with (6). These components are used as initial data while employing gradient methods of minimization to find the next $(n + 1)$ th-point for the minimizing sequence in the space $(B_j, M_i, A_{ki}, T_{ki}, \rho_{ki})$. The Goldfarb method with variable metric [12] can be recommended as the most efficient with respect to the convergence rate and stability.

AN EXAMPLE OF SOLVING THE PROBLEM OF THE OPTIMUM CONTROL

We present the results of application of the method described for solving the problem of optimizing (with respect to the efficiency) the profile of the irregular waveguide in a relativistic traveling-wave tube. Equations (1) governing the nonlinear interaction of the electron current with an electromagnetic wave excited in the waveguide by this current are described in detail in [13–15]. These equations are not presented here due to their cumbersome form. In the case under consideration, the normalized profile of the waveguide

$$g(T) = \frac{b(T)}{b_0}$$

acts as a control function for the interaction process. Here, $b(T)$ is the inner radius of the waveguide, b_0 is the

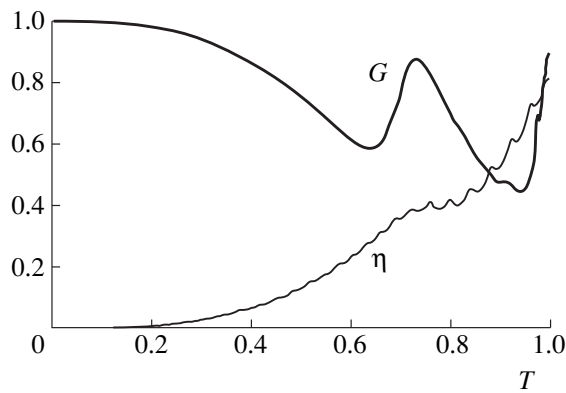


Fig. 1.

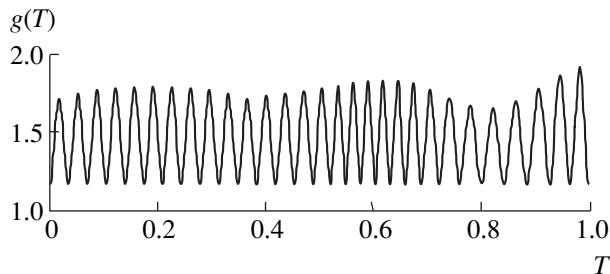


Fig. 2.

critical radius for the E_{01} -wave [13–15], $T = Z/L$, Z is the current length along the waveguide axis, and L is the length of the interaction region, i.e., $T \in [0, 1]$, $T_0 = 1$. The control function $g(T)$ was specified in the form of (4).

We present here the data from one of the optimum variants found: $2\pi L/\lambda = 31.4$ (λ is the wavelength used), $|I_0| = 200$ A is the electron beam current, $\beta_0 = v_0/c = 0.729$ (v_0 is the electron velocity, c is the speed of light in vacuum), and $P_{in} = 0.06P_0$ is the input power (P_0 is the electron-beam power). For the optimized variant, the calculated efficiency is $\eta_{opt} = 0.814$ (the efficiency for a traveling-wave tube with a regular corrugated waveguide does not exceed the level of 0.45). The integral characteristics $\eta(T)$ and $G(T)$ for this variant are shown in Fig. 1. Here, $G(T)$ is the function of the phase-focusing action for electrons: $G = 1$ in the absence of the bunching, while $G = 0$ in the case of the complete (ideal) bunching. The optimum profile of the waveguide $g_{opt}(T)$ is shown in Fig. 2. The mechanism of the optimum interaction within the variant under consideration differs noticeably from that previously found in [13–15]. It can be interpreted as a mechanism of a double strong phase focusing for an electron bunch, when its energy is taken off twice as intensely. The first segment, where the energy is taken off, is located within the interval $T = 0.2$ – 0.7 . In this segment, the bunching is the most pronounced at $T = 0.64$. Furthermore, the bunch decomposes ($T = 0.64$ – 0.72). To

restore bunching in the segment $T = 0.72$ – 0.84 , the strong regime of the energy take-off is engaged, and a characteristic shoulder is formed on the curve $\eta(T)$. At $T = 0.85$, the level of bunching is restored, and furthermore, up to $T = 1$, the second segment of the enhanced energy take-off with improved bunching function is located.

Thus, in this paper, the gradient method is proposed for solving problems of the optimum control. The method is based on approximating the control in the class of atomic functions and using a conjugated (in the Hamiltonian sense) system of equations for the analytic determination of the goal-function gradient. Owing to this approach, the method proposed accelerates the solving of the optimization problem by the factor of $(n + 3)/4$, where n is the number of the parameters being optimized. Using, as an example, the method proposed for solving the problem of optimization (with respect to the efficiency) of the irregular-waveguide profile in a relativistic traveling-wave tube, we have performed the numerical experiment that has demonstrated the efficiency of the method. Therefore, this approach can have wide applications in optimizing electronic microwave equipment and instrumentation.

REFERENCES

1. A. A. Kuraev and S. V. Kolosov, in *Electronic Technique. Ser. 1. Microwave Electronics (2)*, (1974), pp. 45–57.
2. A. A. Kuraev, *Zh. Vychisl. Mat. Mat. Fiz.* **18**, 1604 (1978).
3. A. A. Kuraev, *Theory and Optimization of Microwave Electronic Devices* (Nauka i Tekhnika, Minsk, 1979).
4. A. A. Kuraev, *High-Power Microwave Devices. Methods of Analysis and Optimization of Parameters* (Radio i Svyaz', Moscow, 1986).
5. V. F. Kravchenko, V. A. Rvachev, and V. L. Rvachev, *Radiotekh. Électron.* **40**, 1385 (1995).
6. V. F. Kravchenko and A. A. Zamyatin, *Dokl. Akad. Nauk* **365**, 340 (1999) [*Dokl. Phys.* **44**, 171 (1999)].
7. V. F. Kravchenko and A. A. Zamyatin, *Dokl. Akad. Nauk* **365**, 475 (1999) [*Dokl. Phys.* **44**, 216 (1999)].
8. V. F. Kravchenko, V. I. Pustovoit, and V. V. Timoshenko, *Dokl. Akad. Nauk* **368**, 184 (1999) [*Dokl. Phys.* **44**, 610 (1999)].
9. V. F. Kravchenko, *Élektromagn. Volny Électron. Sist.* **3**, 40 (1998).
10. V. F. Kravchenko, A. A. Kuraev, and V. A. Rvachev, *Radiotekhnika*, No. 9, 4 (1997).
11. V. F. Kravchenko, A. A. Kuraev, A. K. Sinitsyn *et al.*, *Élektromagn. Volny Électron. Sist.* **4**, 33 (1999).
12. D. Goldfarb, *Math. Comput.* **24**, 23 (1970).
13. A. A. Kuraev and T. L. Popkova, *Radiotekh. Électron.* **42**, 1256 (1997).
14. A. A. Kuraev, T. L. Popkova, and A. K. Sinitsyn, *Radiotekhnika*, No. 9, 13 (1997).
15. A. A. Kuraev, T. L. Popkova, and A. K. Sinitsyn, *Élektromagn. Volny Électron. Sist.* **3**, 49 (1998).

Translated by V. Tsarev

Temperature Modifications of Structural and Magnetic Characteristics of Multicomponent Amorphous Cobalt-Base Alloys

V. A. Polukhin, L. I. Malkina, and Academician N. A. Vatolin

Received July 20, 1999

In this study, on the basis of X-ray-structural data and the measurements of magnetic characteristics (the magnetic permeability, the maximum induction, and the coercive force), we have revealed correlations between modifications of structural and magnetic properties on various types of relaxation annealing. Moreover, by analyzing the correlation functions $\{A(S)$ and the radial-distribution function} and using values of structural parameters, we investigated the processes of the amorphous-state stabilization, the nucleation, and the growth of the crystalline phase for magnetically soft amorphous cobalt-base alloys obtained by the spinning of melts. We investigated the multicomponent amorphous alloys with the following compositions: $\text{Co}_{57}\text{Ni}_{10}\text{Fe}_5\text{Si}_{11}\text{B}_{17}$, $\text{Co}_{67}\text{Fe}_3\text{Cr}_3\text{Si}_{15}\text{B}_{12}$, and $\text{Co}_{68}\text{Fe}_4\text{Cr}_4\text{Si}_{13}\text{B}_{11}$. All of these alloys have a virtually zero magnetostriction. The structure was analyzed with invoking the data of molecular-dynamic simulation for binary amorphous alloys $\text{Co}_{1-x}\text{B}_x$ and $\text{Fe}_{1-x}\text{B}_x$ [1].

For the alloys under consideration at room temperature, we observe a typical diffraction pattern with a pronounced effect in the form of a split second maximum (see Fig. 1). It can be also easily seen that the first minimum is deeper than that for melts [2, 3]. In the scattering curve (Fig. 2), a secondary maximum appears (with the shape of a “shoulder”) in the region of small angles (superimposed on the principle peak of intensity). It is worth noting that, for the alloy $\text{Co}_{57}\text{Ni}_{10}\text{Fe}_5\text{Si}_{11}\text{B}_{17}$, the curves both for the structural factor and for the radial-distribution functions, with the splitting of the second peaks into subpeaks, differ substantially from the corresponding curves for other alloys: adding nickel with decreasing the concentration of cobalt leads to increasing the fraction of large interatomic spacings and to “loosening” the packing around metalloids atoms. These changes are just reflected by the “inversion” of the ratio between the heights of the right-hand and left-hand subpeaks of the second peak. It is remarkable that, in

the multicomponent alloys under consideration, the half widths $L_{1/2}$ {or L_c for the first $A(S)$ peaks} of the principle maxima of the radial-distribution function are close to those for the model melts [1]. The half-widths for the first diffraction maxima are related to the correlation radii and to the statistics of interatomic spacings, and the height $A(S_1)$ is related to the packing density of atoms [4]; i.e., the higher first $A(S)$ maximum corresponds to the alloy with close-packed metal atoms. As a result of the relaxation, increasing the first subpeak occurs, being accompanied by decreasing the shoulder (the second subpeak), whereas, in the case of the recrystallization, the opposite picture is observed: the first subpeak decreases, while the shoulder is modified into the Bragg diffraction maximum. It means that the structural relaxation is not the onset of the crystallization but is a transformation of the system state into the V -structure state [5]. In this case, the position of the first $A(S)$ maximum for the multicomponent amorphous cobalt-base bands is displaced towards larger scattering angles as compared with its abscissa for liquid cobalt at T_{melt} and for the $\text{Co}_{80}\text{B}_{20}$ melt near the liquidus curve, whereas the most probable spacing R_1 does not virtually differ from that for cobalt [3].

The temperature modifications of the structure of alloys were investigated at the step-like conditions of heating the samples with the heating time of 45–60 min at the exposure temperatures. In Fig. 2, we present the structural factors $A(S)$ obtained by the X-ray analysis of the alloy $\text{Co}_{68}\text{Fe}_4\text{Cr}_4\text{Si}_{13}\text{B}_{11}$ under the heating conditions stated. The most probable is the formation of new metastable phases: amorphous and crystalline. In this case, additional sources of inner stresses appear in the amorphous matrix as a result of the multiphase nucleation and the development of a frame-like structure of individual local packings around the metalloids atoms [5]. It can be seen from Fig. 2 that the ordinates of the first peaks in the structural factor vary insignificantly (the similar picture took place also for the radial-distribution function), while the shape of the curves changes appreciably. It is distinct from the case of binary alloys for which increasing and narrowing the peaks indicated always take place on the heat treatment. Moreover, we

Institute of Metallurgy, Ural Division,
Russian Academy of Sciences,
ul. Amundsena 101, Yekaterinburg, 620016 Russia

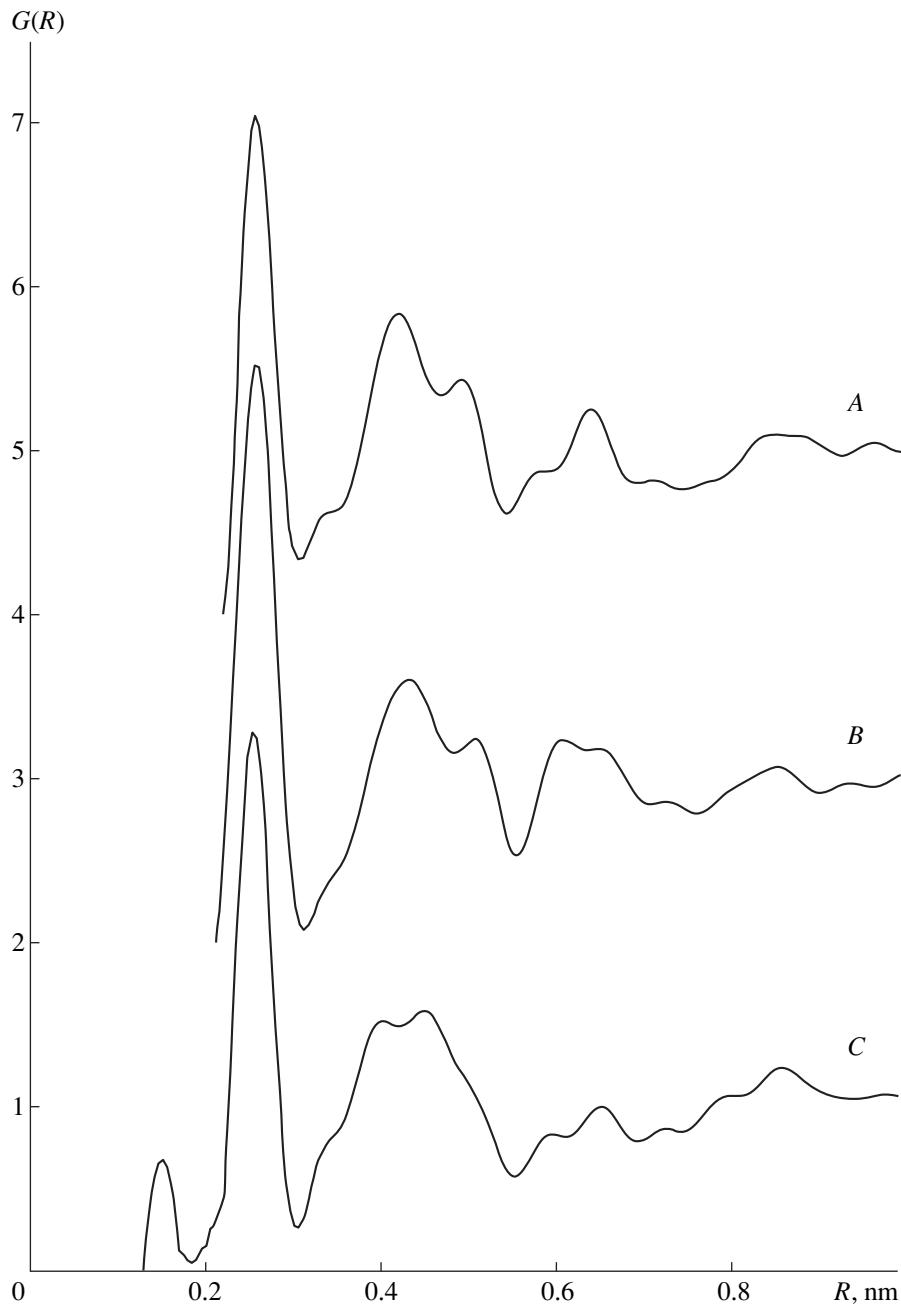


Fig. 1. Radial-distribution functions of atoms in amorphous alloys of various compositions as the Fourier images of the X-ray structural factors: (A) $\text{Co}_{68}\text{Fe}_4\text{Cr}_4\text{Si}_{13}\text{B}_{11}$, (B) $\text{Co}_{67}\text{Fe}_3\text{Si}_{15}\text{B}_{12}$, and (C) $\text{Co}_{57}\text{Fe}_5\text{Ni}_{10}\text{Si}_{11}\text{B}_{17}$.

observed that the values of parameters S_1 (as well as R_1) are close to those for a close-packed structure of atoms of a base metal (Co). This fact shows that the relaxation annealing sometimes leads to increasing and narrowing every $A(S)$ peak or the radial-distribution function of atoms (this is especially true for the first peak, that is typical for single- or two-component amorphous metals), because the number of locally-equilibrium values of interatomic spacings, the spread around which decreases under annealing, is determined by the composition, while these equilibrium values themselves are

determined by the nature of chemical bonds in an amorphous alloy. The annealing results in increasing the density of an amorphous alloy and in isolating a free volume if the diffusion processes become more intense.

The half-width of the integral radial-distribution functions of atoms in the multicomponent alloys under consideration is equal to 0.046 nm (for comparison, it is 0.039 nm for $\text{Fe}_{80}\text{B}_{20}$ and 0.45 nm for $\text{Co}_{80}\text{B}_{20}$ [1]) and is known to be directly related to the mean square displacements of atoms ($L_{1/2} \Rightarrow \langle \Delta R^2 \rangle$). For the V -struc-

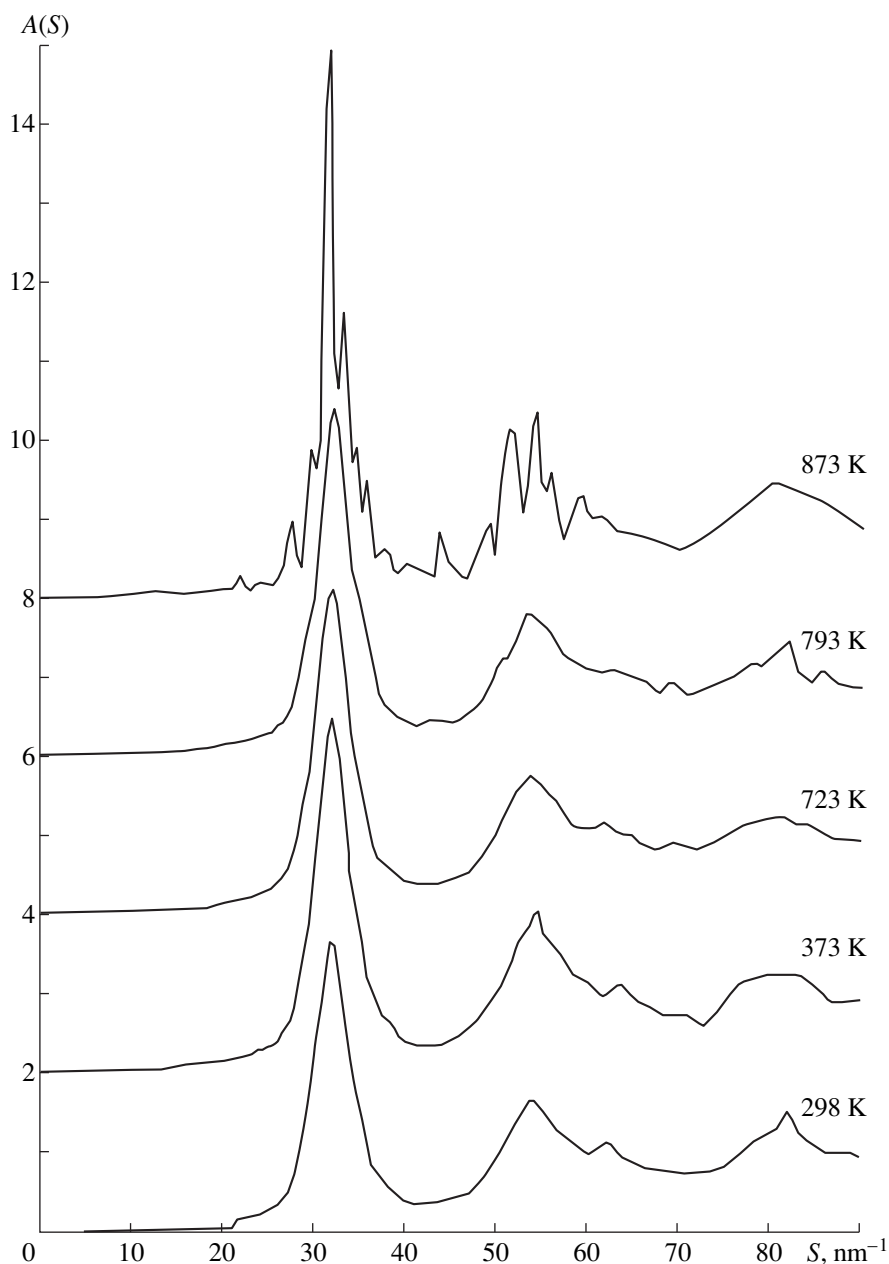


Fig. 2. X-ray structural factors for the amorphous bands of the $\text{Co}_{68}\text{Fe}_4\text{Cr}_4\text{Si}_{13}\text{B}_{11}$ alloy obtained on relaxation heating with time of high-temperature storage of 45–50 min for every temperature of exposure.

ture at a temperature T with heat displacements of atoms about the equilibrium centers in the amorphous structure, the mean square displacement $\langle \Delta R^2 \rangle$ can be related to the Debye characteristic temperature Θ_D [3] as

$$\langle \Delta R^2 \rangle^2 = \frac{2.89T}{M\Theta_D^2},$$

where M is the molar mass. For the known settled-life time τ , the diffusion coefficient $D = \langle \Delta R^2 \rangle / \tau$, limiting

the intensity of the relaxation process, can also be estimated.

The annealing not only results in decreasing the spread of partial interatomic spacings about the equilibrium values, but also activates sharply the diffusion processes accompanying the rearrangement of local packings. In this case, for multicomponent alloys, a more sensitive characteristic of the structure modifications resulted from the relaxation annealing is sometimes not the height $G(R)$ of the principle peak, but its half-width $L_{1/2}$ {like the half-width L_c for $A(S)$ }, which almost symbasically repeats the extrema of significant

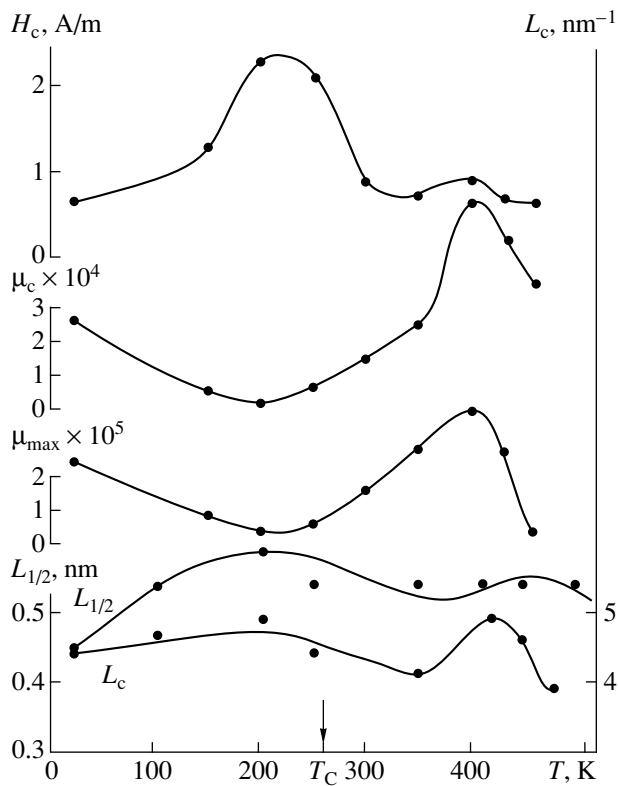


Fig. 3. Dependence of magnetic characteristics (H_c , μ_0 , and μ_{\max}) on the annealing temperature $T(K)$ for the amorphous alloy $\text{Co}_{57}\text{Fe}_5\text{Ni}_{10}\text{Si}_{11}\text{B}_{17}$, and the dependence of the half-width of the radial-distribution function of atoms ($L_{1/2}$), $A(S)$, and L_c on the temperature of the X-ray diffraction analysis (T_C is the Curie temperature).

temperature modifications of magnetic characteristics (see Fig. 3). From Fig. 3, it is seen that a nonmonotone variation in the half-width of the first peaks of the radial-distribution function of atoms {and $A(S)$ } correlates reasonably well with the temperature variation in such magnetic characteristics as the coercive force H_c and the permeability μ for the amorphous magnetic cobalt-base alloys. Such an implicit dependence of H_c and μ on the relaxation processes at the local-coordination scale is determined by the specificity of formation of magnetic moments in cobalt-base alloys. In their turn, the magnetic moments are completely determined by the distribution of interatomic spacings between the nearest neighbors independently of values of their local coordination numbers, as with iron-base ferromagnetics. Such a character of structural modifications stems, above all, from the intensity of the relaxation processes at the initial stage of crystallization including that in the surface layers possessing higher density of microinhomogeneity defects as compared with bulk. And here, not only a value of an annealing temperature, but also its duration, determining the “incubation period” for the phase, chemical, and structural modifications, turns out to be the decisive factor. In the course of relaxation,

a single amorphous phase breaks down into a kind of two structure-different phases, namely, the surface and bulk ones, naturally, with different magnetic characteristics.

In the crystalline compounds of the type of the Fe_3C “cementite” with the local trigonal–prismatic order in the coordination sphere, metalloid atoms are surrounded by nine other atoms: six metal atoms (the first nearest neighbors in the coordination shell) and three metalloid atoms (the second nearest neighbors in the first coordination shell). The local order around the metalloid atoms in amorphous iron-base alloys (for example, in the binary $\text{Fe}_{80}\text{B}_{20}$ alloy, molecular-dynamic model) is known to be close to the trigonal–prismatic order (from 6 to 8 vertexes in the first coordination with semioctahedrons on the faces) corresponding to the Archimedean antiprism (the Voronoï polyhedron $\{0, 2, 8\}$ with topological distortions $\{0, 2, 8, 1\}$, with the most likely angles of 75° , and with the metal–metalloid spacings on the order of $0.82R_1$) or to the dodecadeltahedron $\{0, 6, 2\}$ also with 8 vertexes and with the semioctahedrons on every face [5]. At the same time, the basis of the composition ordering in cobalt-base alloys is likely provided by quasi-molecular formations emerging around every atom. These formations are geometrically close to the trigonal–prismatic polyhedrons with three semioctahedrons per every square face of the prism (with the coordination being close to 9, with the angles of 82° , with the interatomic metal–metalloid spacing being on the order of $0.76R_1$ as opposed to $0.82R_1$ in the Fe-base alloys, and with both the Voronoï-type polyhedrons $\{0, 3, 6\}$ and their topological distortions, e.g., $\{0, 3, 6, 1\}$, prevailing). With lower probability, Co atoms form the octahedron coordinations around the metalloid atoms with the characteristic interatomic spacings of $0.71R_1$ and with an angle of 90° (the octahedron coordination can be transformed into the prismatic one by turning only one face through 60° [5]). In other words, it can be assumed that the amorphous band is heterogeneous in types of packing of atoms and in distribution of components, and it involves atomic microgroups, which differ in the interatomic spacings, coordination numbers, and concentration of components. Actually, the metal–metalloid spacings (in the range from $0.71R_1$ to $0.83R_1$) must be smaller, and the metal–metal spacings (close to R_1) must be larger in amorphous alloys than those in pure metals; it is these groups that influence the position and the shape of the first maximum. In the course of vitrification of a melt, these stiff quasimolecular formations combine into an immobile frame (the residual diffusion of metal atoms being realized in cavities of the frame [5]) and dictate the features of the shape for the first peaks of structural factors in the small-angle region.

The relaxation of the structure in an amorphous alloy, as noted above, involves the topological and composition or chemical ordering. In the first case, the geometry of the short-range order varies predomi-

nantly. This manifests itself, firstly, as the regularization of interatomic spacings in the first coordination around the metal atoms, that approaches an icosahedron in shape (with two characteristic spacings R_1 and $0.95R_1$). As a consequence, the left-hand subpeak of the second peak emerges and grows. Secondly, the regularization of the geometry of the prismatic (octahedron) coordination for the nearest neighbors around the metalloid atoms also develops in accordance with the dimensional factor through the relationship between the atomic radii for metals and metalloids. The types of contacts for the second nearest neighbors (through a pair of atoms or a "dumbbell", a triple contact, a triangle, and the contacts in linear chains [6]) are also relevant. The composition relaxation involves such an element of structural modifications as "avoiding" the first nearest neighboring metalloid atoms (by "wedging" the pairs formed in the course of the superfast annealing by the pairs of metal atoms). The presence of a shoulder in the first peak of the radial-distribution function of atoms (Fig. 1, curve C) can be associated with an inhomogeneous localization of atoms in the first coordination sphere. These atoms provide the presence of, at least, two shortest spacings that correspond to the first peak of the radial-distribution function.

The heating to temperatures of 620–720 K influences predominantly the modification of such characteristics as $L_{1/2}$ and L_c . At the same temperatures, as already noted, significant modifications of magnetic properties are also observed (see Fig. 3). Decreasing the half-widths of the peaks is most likely influenced by atomic microgroups enriched in metalloid atoms. In these microgroups, the nearest spacings between the metal atoms differ considerably from those inherent in pure metals with close packing of atoms.

At temperatures in the range 790–800 K, the diffraction pattern is still characterized by a diffusion distribution of intensity; $L_{1/2}$ and L_c decrease; simultaneously, the height of the first diffraction maximum $A(S_1)$ increases considerably (6.0–7.0), and also the position of the right-hand subpeak of the second pike is changed. Consequently, as a result of the diffusion processes with increasing the heating temperature, the short-order modifications occur, above all, in coordinations around the metalloid atoms; besides, the atoms are redistributed in microgroups, and the "preparation" for the crystallization takes place being attended with increasing the intensity of the small-angle scattering. The asymmetry of the first peak of the radial-distribution function increases, R_1 being virtually invariable. The microdomains are enlarged including those with the short-range order of the type of intermetallic phases. Several nearby coordination spheres of these phases get into the domain of the first maximum of the radial-distribution function, and this determines the symmetry of the maximum. In the case of multicompo-

nent amorphous alloys, the shape of the splitting (into subpeaks) for the second peak of the radial-distribution function $\{A(S)\}$ and another features (harmonics and shoulders) are influenced by the specificity of formation of the first coordination, above all, from the base-element atoms around the metalloid atoms and by the action of components (nickel, iron, manganese, and chromium) on the density and the geometry of packing because these elements lead to a marked redistribution of statistical weights of the spacings between the first, second, and subsequent nearest neighbors. Increasing the metalloid concentration also modifies the shape of the splitting for the second peak of the structural factor (the radial-distribution function) for the complex-composition alloys under consideration. It is accompanied by a marked reduction in the height of the right-hand subpeak of the second peak. This reduction is virtually as much as that for the continuous "relaxation annealing" in the case of simulated two-component amorphous magnetic alloy $\text{Co}_{1-x}\text{B}_x$ [1]. However, in contrast with single- and two-component amorphous alloys, in the case of thermal treatment of multicomponent systems, the intensity of relaxation processes is characterized more adequately not by the growth and narrowing of the first peak of the function of radial distribution of atoms (the structural factor) but its half-width $L_{1/2}$, which can vary in a nonmonotone way (correlating with H_c , μ_0 , and μ_{\max}) reflecting both the regular succession of the "switching-on" the diffusion processes and their intensity according to the type of chemical bond and the values of potential barrier for every component.

ACKNOWLEDGMENTS

This work was supported by the Russian Foundation for Basic Research, project no. 99-03-32317.

REFERENCES

1. V. A. Polukhin, L. I. Malkina, and N. I. Sidorov, *Rasplavy* **13**, 12 (1999).
2. N. A. Vatolin and É. A. Pastukhov, *Diffraction Investigation of Structure of High-Temperature Melts* (Nauka, Moscow, 1980).
3. S. I. Popel', M. A. Spiridonova, and L. A. Zhukova, *Atomic Ordering in Melts and Amorphous Metals* (Yekaterinburg, 1997).
4. J. M. Cowley, *Diffraction Physics* (North-Holland, Amsterdam, 1975; Mir, Moscow, 1977).
5. V. A. Polukhin and N. A. Vatolin, *Rasplavy* **1**, 29 (1987).
6. V. A. Polukhin and N. A. Vatolin, *Simulation of Amorphous Metals* (Nauka, Moscow, 1985).

Translated by V. Bukhanov

Translational–Rotary Motion as a New Method for Attacking Astrometric Problems in Theory of the Earth’s Rotation

Yu. G. Markov, L. V. Rykhlova, and I. V. Skorobogatykh

Presented by Academician A.A. Boyarchuk July 1, 1999

Received July 1, 1999

A basis for many astrometric studies is the dynamic theory of the Earth’s rotation about its center of mass.

At the end of the 18th century, L. Euler derived differential equations for the rotary motion of a rigid body about a fixed point, which were used in the original form until the present time. He showed that the instantaneous axis of rotation can circumscribe a cone about the body axis. Euler also evaluated that the period of this motion, which he called the period of free nutation, is about 305 days for a body with the Earth’s dimensions and shape. The effect of external forces was assumed to be absent.

Nearly a century later, from observations, the period of nutation was found to be 412 to 430 days. The disagreement of this estimate with the predicted one was ascribed to the elasticity and deformability of the Earth, inhomogeneity of its structure, etc. This value was called the Chandler period in honor of its discoverer.

Since then, all existing theories about the Earth’s rotation came to be constructed on the basis of the interior structure of the Earth, whereas the observed rotational parameters, in turn, are considered as criteria for accepting an appropriate Earth model.

The Earth’s rotation around the axis passing through the center of mass is usually considered, almost without exception, independently of the displacement of the Earth’s center of mass about the Sun and about the barycenter of the Earth–Moon system. The interaction between translational and rotational motions is postulated to be absent [1].

From the dynamic standpoint, this approach accounts quite adequately for the overall motion of the Earth in space. However, the specialized international observations and studies of the motion of the Earth’s poles have revealed that, within the framework of this approach, understanding the mechanisms of excitation of the basic component of the pole motion, i.e., the Chandler component, did not advance.

In our opinion, it is the currently available precision in determining parameters of the Earth’s rotation that necessitates the removal of a number of simplifications in the presently accepted Earth-rotation theory. When constructing a high-precision theory for the rotary motion of the deformable Earth, a more general statement of the problem seems to be appropriate. We imply such subtle dynamic effects as the free nutation of the Earth-rotation axis and the variation of latitudes. A mathematical model is proposed in which the Earth is considered as an elastic rigid body dissipating its energy in the deformation process and executing translational–rotary motion in the Earth–Moon system in the gravitation field of the Sun.

We propose a new theoretical model in which the orbit of the viscoelastic planet evolves as a result of the work accomplished by internal dissipative forces (with allowance for no thermodynamic processes), whereas the planet by itself executes orbital–rotary motion.

1. The Earth is conceived as consisting of two components: the rigid one (core), occupying the domain $\Omega_1 \in \mathbf{E}^3$, and the viscoelastic shell (mantle), occupying, in the natural undistorted state, the domain $\Omega \in \mathbf{E}^3$. The densities of these components are ρ_1 and ρ_2 , respectively (\mathbf{E}^3 is the three-dimensional Euclidean space). The domains Ω_1 and Ω have a common boundary Γ . On the boundary between the core and the mantle, particles of the elastic medium (mantle) do not move; the other part of the boundary (the Earth’s surface) is free. The elastic medium obeys the linear theory of elasticity for small strains. The modal approach is taken as the basic one. In the case of the axial-symmetric elastic component with axisymmetric boundary conditions, the vector \mathbf{u} of the elastic displacement is represented in the form of [5] as

$$\mathbf{u}(\mathbf{r}, t) = \sum_{k, m=0}^{\infty} [q_{km}(t)\mathbf{V}_{km}(\mathbf{r}) + p_{km}(t)\mathbf{W}_{km}(\mathbf{r})]. \quad (1)$$

Here, $q_{km}(t)$ and $p_{km}(t)$ are the generalized normal coordinates (modal variables) describing the planetary motion in terms of the internal degrees of freedom;

$\mathbf{V}_{km}(\mathbf{r})$ and $\mathbf{W}_{km}(\mathbf{r})$ are the characteristic free-oscillation forms for the elastic component, which correspond to the fundamental frequency ν_{km} and obey the orthonormalization conditions. The characteristic forms $\mathbf{V}_{km}(\mathbf{r})$ and $\mathbf{W}_{km}(\mathbf{r})$ are functions of the coordinates \mathbf{r} for an elastic-medium particle. These functions are obtained from one another by rotating through the angle $\varphi_k = \pi/(2k)$ about the symmetry axis, where $2k$ is the number of nodes of the characteristic form counted off along the parallel, and m is the corresponding form number at a fixed k . It is worth noting that the equations for free oscillations of an axial-symmetric elastic body (planet) are conveniently considered in a cylindrical coordinate system (ρ, φ, z) . Then, in this system, orthogonal-basis characteristic forms with $k \neq 0$ are

$$\begin{aligned} & \mathbf{V}_{km}(\rho, \varphi, z) \\ &= \{ U_{km}(\rho, z) \sin k\varphi, V_{km}(\rho, z) \cos k\varphi, W_{km}(\rho, z) \sin k\varphi \}, \\ & \mathbf{W}_{km}(\rho, \varphi, z) = \{ U_{km}(\rho, z) \cos k\varphi, -V_{km}(\rho, z) \sin k\varphi, \\ & \quad W_{km}(\rho, z) \cos k\varphi \}. \end{aligned} \tag{2}$$

Axial-symmetric characteristic forms describing longitudinal–transversal strains correspond to the case $k = 0$. Bending-type strains correspond to forms with $k = 1$. For $k = 2$, we obtain strains that can serve to describe tidal humps such as on a celestial body.

Viscoelastic features of the material of the planet shell (mantle) are specified by dissipative functional $D[\dot{\mathbf{u}}]$ proportional to the potential-energy functional corresponding to elastic strains. This is true provided that, in the latter functional, components of the small-strain tensor are substituted by the corresponding components of the strain-rate tensor, i.e., $D[\dot{\mathbf{u}}] = \chi b E [\dot{\mathbf{u}}]$ (the Kelvin–Voigt model), where χ is the coefficient accounting for the energy dissipation, and b is a dimensional constant.

The model proposed allows us to derive mathematically justified results compatible with the current-observation precision, while describing the translational–rotary motion of planets and their satellites.

2. The equations of motion involve equations both describing the translational–rotary motion of a planet as a whole and determining strains. The class of problems under consideration is characterized by the presence of processes with various characteristic times. Basic methods for solving these problems are the averaging method and its modifications.

We present equations for the translational–rotary motion of a deformable-planet–satellite system in the field of an attracting center (three-dimensional version of the problem). These equations have been originally derived by the authors and can be used for mathematically modeling the motion of the Earth–Moon system in the gravitation field of the Sun.

We assume that $O\xi_1\xi_2\xi_3$ is the inertial coordinate system with the origin at the attracting center O and with the $O\xi_3$ -axis orthogonal to the plane of the orbit of the point C_0 , which is the barycenter of the planet–satellite system. We introduce the König coordinate system $C_0\xi'_1\xi'_2\xi'_3$ at the center of mass of the deformable planet–satellite system. Notice that in the undistorted state, the planet is dynamically compressed, i.e., $C > A$, where C and A are the axial and equatorial moments of inertia, respectively. A coordinate system $C'_2x_1x_2x_3$ is rigidly bound to the planet hard core; the axes of the system are aligned in parallel with the principal central axes of the undistorted planet; the point C'_2 is the center of mass of the planet in the absence of strains. The functional for the potential energy of attraction between the planet and the satellite is

$$\Pi = -\frac{m_1 m_2 f}{R_{21}} + \mu_1 R_{21}^3 \left[\frac{1}{2}(A - C)(1 - 3\gamma_3^2) + U_1 \right],$$

$$U_1 = \int_{\Omega} \rho_2 [(\mathbf{r}, \mathbf{w}) - 3(O^{-1}\mathbf{R}_{21}^0, \mathbf{r})(O^{-1}\mathbf{R}_{21}^0, \mathbf{w})] dx, \tag{3}$$

$$\mathbf{w} = \mathbf{u} - \mathbf{u}_C, \quad \mu_1 = f m_1, \quad dx = dx_1 dx_2 dx_3.$$

Here, f is the gravitational constant; m_1 and m_2 are the masses of the planet and the satellite, respectively; $\mathbf{R}_{21} = \mathbf{R}_{21}\mathbf{R}_{21}^0$ is the radius vector drawn from the point C_2 to the center of mass of the satellite (the point C_1). The matrix $O(t)$ specifies the transition from the coordinate system $C_2x_1x_2x_3$ (which is obtained from the coordinate system $C'_2x_1x_2x_3$ by parallel translation to the point C_2) to the König coordinate system $C_0\xi'_1\xi'_2\xi'_3$. $O^{-1}\mathbf{R}_{21}^0 = (\gamma_1, \gamma_2, \gamma_3)$ are the projections of the unit vector \mathbf{R}_{21}^0 onto the axes of the coordinate system C_2x_i ($i = 1, 2, 3$); $\rho_2 = \text{const}$ and Ω are the density of the elastic component and the domain occupied by it in the natural undistorted state; \mathbf{w} and \mathbf{u} are the vectors of the elastic displacement (with respect to the coordinate systems C_2x_i and C'_2x_i) for a particle of the medium, which occupied the position \mathbf{r} ; and \mathbf{u}_C is the planet center-of-mass displacement, occurring under deformations, with respect to the planet core. The terms on the order of $\left(\frac{l}{R_{21}(0)}\right)^3$ and higher are omitted in (3). Here, l is the characteristic size of the planet, and $R_{21}(0)$ is the initial value of R_{21} . The form of the potential-energy functional for attraction of the satellite and the planet by the center O is similar to (3).

For describing rotary motion of the planet as a whole about its center of mass (i.e., about the point C_2), we use the canonical Andoyer variables I_i, φ_i ($i = 1, 2, 3$).

Here, $I_2 = |\mathbf{G}|$ is the module of the kinetic-moment vector \mathbf{G} , I_1 and I_3 are the projections of the vector \mathbf{G} onto the axes C_2x_1 and $C_2\xi_3'$, respectively; and the following relations are valid: $\cos\delta_1 = I_3I_2^{-1}$ and $\cos\delta_2 = I_1I_2^{-1}$. The relative orbital circular motion of the centers of mass C_1 and C_2 is described in terms of the Delone variables Λ , H , ϑ , and h , where $\Lambda = |\mathbf{\Lambda}|$ is the total angular momentum for the centers of mass of the planet and satellite, while their moving about the barycenter; H is the projection of the vector $\mathbf{\Lambda}$ onto the axis $C_0\xi_3'$, ϑ is the true anomaly, h is the longitude of the ascending orbital node on the plane $C_0\xi_1'\xi_2'$, and $\frac{H}{\Lambda} = \cos i$, where i is the inclination of the center-of-mass orbital plane to the ecliptic plane. While deriving the equations of motion, it is convenient to use the Routh functional $R[\Lambda, H, \vartheta, h, I_i, \varphi_i, \mathbf{w}, \dot{\mathbf{w}}]$. The equations of translational-rotary motion for the deformable-planet-satellite system in the field of a gravitation center, written out as the canonical Routh equations, have the form

$$\begin{aligned} \dot{I}_i &= -\frac{\partial R_*}{\partial \varphi_i} + 3\mu_1 R_{21}^{-3} \left\{ (A-C)\gamma_3 \frac{\partial \gamma_3}{\partial \varphi_i} \right. \\ &+ \int_{\Omega} \rho_2 \frac{\partial}{\partial \varphi_i} [(O^{-1}\mathbf{R}_{21}^0, \mathbf{r})(O^{-1}\mathbf{R}_{21}^0, \mathbf{u})] dx \left. \right\} \\ &+ 3\mu_0 R^{-3} \left\{ (A-C)\kappa_3 \frac{\partial \kappa_3}{\partial \varphi_i} \right. \\ &+ \int_{\Omega} \rho_2 \frac{\partial}{\partial \varphi_i} [(O^{-1}\mathbf{R}^0, \mathbf{r})(O^{-1}\mathbf{R}^0, \mathbf{u})] dx \left. \right\}, \\ \dot{\varphi}_1 &= \left(\mathcal{J}^{-1}[\mathbf{w}](\mathbf{G} - \mathbf{G}_w), \frac{\partial \mathbf{G}}{\partial I_1} \right) \\ &- 3\mu_1 R_{21}^{-3} \left\{ (A-C)\gamma_3 \frac{\partial \gamma_3}{\partial I_1} \right. \\ &+ \int_{\Omega} \rho_2 \frac{\partial}{\partial I_1} [(O^{-1}\mathbf{R}_{21}^0, \mathbf{r})(O^{-1}\mathbf{R}_{21}^0, \mathbf{u})] dx \left. \right\} \\ &- 3\mu_0 R^{-3} \left\{ (A-C)\kappa_3 \frac{\partial \kappa_3}{\partial I_1} \right. \\ &+ \int_{\Omega} \rho_2 \frac{\partial}{\partial I_1} [(O^{-1}\mathbf{R}^0, \mathbf{r})(O^{-1}\mathbf{R}^0, \mathbf{u})] dx \left. \right\}, \end{aligned}$$

$$\begin{aligned} \dot{\varphi}_3 &= -3\mu_1 R_{21}^{-3} \left\{ (A-C)\gamma_3 \frac{\partial \gamma_3}{\partial I_3} \right. \\ &+ \int_{\Omega} \rho_2 \frac{\partial}{\partial I_3} [(O^{-1}\mathbf{R}_{21}^0, \mathbf{r})(O^{-1}\mathbf{R}_{21}^0, \mathbf{u})] dx \left. \right\} \\ &- 3\mu_0 R^{-3} \left\{ (A-C)\kappa_3 \frac{\partial \kappa_3}{\partial I_3} \right. \\ &+ \int_{\Omega} \rho_2 \frac{\partial}{\partial I_3} [(O^{-1}\mathbf{R}^0, \mathbf{r})(O^{-1}\mathbf{R}^0, \mathbf{u})] dx \left. \right\}, \\ \dot{S} &= 3\mu_0 R^{-3} m_* R_{21}^2 \cos\theta \frac{\partial \cos\theta}{\partial S} \\ &+ 3\mu_1 R_{21}^{-3} \left\{ (A-C)\gamma_3 \frac{\partial \gamma_3}{\partial S} \right. \\ &+ \int_{\Omega} \rho_2 \frac{\partial}{\partial S} [(O^{-1}\mathbf{R}_{21}^0, \mathbf{r})(O^{-1}\mathbf{R}_{21}^0, \mathbf{u})] dx \left. \right\}, \\ (S, s) &\in \{(\Lambda, \vartheta), (H, h)\} \quad (i = 1, 2, 3), \\ \dot{h} &= -3\mu_0 R^{-3} m_* R_{21}^2 \cos\theta \frac{\partial \cos\theta}{\partial H} \\ &- 3\mu_1 R_{21}^{-3} \left\{ (A-C)\gamma_3 \frac{\partial \gamma_3}{\partial H} \right. \\ &+ \int_{\Omega} \rho_2 \frac{\partial}{\partial H} [(O^{-1}\mathbf{R}_{21}^0, \mathbf{r})(O^{-1}\mathbf{R}_{21}^0, \mathbf{u})] dx \left. \right\}, \\ \dot{\vartheta} &= n + \mu_0 R^{-3} m_* R_{21}^2 \left\{ R_{21}^{-1} \frac{\partial R_{21}}{\partial \Lambda} (1 - 3\cos^2\theta) \right. \\ &- 3\cos\theta \frac{\partial \cos\theta}{\partial \Lambda} \left. \right\} - 3\mu_1 R_{21}^{-4} \frac{\partial R_{21}}{\partial \Lambda} \left[\frac{1}{2}(A-C)(1 - 3\gamma_3^2) \right. \\ &+ \int_{\Omega} \rho_2 \frac{\partial}{\partial \Lambda} [(O^{-1}\mathbf{R}_{21}^0, \mathbf{r})(O^{-1}\mathbf{R}_{21}^0, \mathbf{u})] dx \left. \right] \\ &- 3\mu_0 R^{-3} \left\{ (A-C)\gamma_3 \frac{\partial \gamma_3}{\partial \Lambda} \right. \\ &+ \int_{\Omega} \rho_2 \frac{\partial}{\partial \Lambda} [(O^{-1}\mathbf{R}^0, \mathbf{r})(O^{-1}\mathbf{R}^0, \mathbf{u})] dx \left. \right\}. \end{aligned} \tag{4}$$

Here, $R_* = \frac{1}{2}(\mathbf{G} - \mathbf{G}_w, J^{-1}[\mathbf{w}](\mathbf{G} - \mathbf{G}_w))$, $\mathbf{G}_w = \int_{\Omega} \rho_2[(\mathbf{r} + \mathbf{w}) \times \dot{\mathbf{w}}] dx$, and

$$J^{-1}[\mathbf{w}] = J_0^{-1} - J_0^{-1} J_1[\mathbf{w}] J_0^{-1} + \dots,$$

$$J_0^{-1} = \text{diag}(A^{-1}, A^{-1}, C^{-1}),$$

$$\frac{\partial R_*}{\partial \varphi_2} = \frac{\partial R_*}{\partial \varphi_3} = 0, \quad m_* = \frac{m_1 m_2}{m},$$

μ_0 is the gravitational parameter of the attracting center. Furthermore, $O^{-1}\mathbf{R}^0 = (\kappa_1, \kappa_2, \kappa_3)$ are the projections of the unit vector \mathbf{R}^0 onto the axes of the coordinate system C_2x_i ($i = 1, 2, 3$), and $(\mathbf{R}^0, \mathbf{R}_{21}^0) = \cos \theta = \cos \vartheta \cos(\vartheta_1 - h) + \cos i \sin \vartheta \sin(\vartheta_1 - h)$.

The equation for the angular variable φ_2 can be obtained by adding the term $\frac{\partial R_*}{\partial I_2}$ to the right-hand side

of the equation for φ_3 , while substituting $\frac{\partial(\cdot)}{\partial I_3} \rightarrow \frac{\partial(\cdot)}{\partial I_2}$.

Equations (4) obtained make it possible to study the complex problem of the translational–rotary motion for the Earth–Moon system with allowance made for viscoelastic properties of the Earth material.

It is worth noting that setting up the problem in such a way may play a crucial role in studying the evolution

processes in the Solar system under the action of gravitation tides [2–8]. The global evolution of the Earth–Moon system can be evaluated on the basis of the evolution (averaged) equations derived on the basis of the exact equations for system (4).

REFERENCES

1. H. Moritz and I. Mueller, *Earth Rotation. Theory and Observations* (Ungar Phys. Publ. Comp., New York; Naukova Dumka, Kiev, 1992).
2. G. H. Darwin, *The Tides and Kindred Phenomena in the Solar System* (John Murrey, London, 1898; Nauka, Moscow, 1969).
3. P. Goldreich and S. J. Peale, *Astron. J.* **72**, 662 (1967) [in *Tides and Resonances in the Solar System.*, Ed. by V. N. Zharkov (Mir, Moscow, 1975)].
4. N. N. Kozlov and T. M. Eneev, Preprint No. 134, IPM RAN (Keldysh Institute of Applied Mathematics, Russian Academy of Sciences, Moscow, 1977).
5. V. G. Vil'ke, *Analytic and Qualitative Methods of Mechanics for Systems with Infinite Degree-of-Freedom Number* (Moscow State Univ., Moscow, 1986).
6. Yu. G. Markov, *Astron. Zh.* **73**, 748 (1996) [*Astron. Rep.* **40**, 681 (1996)].
7. V. V. Bondarenko, Yu. G. Markov, and I. V. Skrobogatykh, *Astron. Vestn.* **32**, 340 (1998).
8. V. V. Bondarenko, A. V. Demin, and Yu. G. Markov, *Izv. Akad. Nauk, Ser. Fiz.* **62**, 1884 (1998).

Translated by V. Tsarev

**POWER
ENGINEERING**

“Sakhalin” Pulsed MHD 500 MW Power System Based on Solid-Propellant Fuel

Academician **E. P. Velikhov***, **O. G. Matveenko****, **V. P. Panchenko****,
Corresponding Member of the RAS **V. D. Pismennyi*****, **A. A. Yakushev****, **A. V. Pisakin*****,
A. G. Blokh***, **B. G. Tkachenko*****, **N. M. Sergeenko*****, Academician **V. B. Zhukov******,
Yu. P. Babakov****, **E. F. Zhegrov******, **V. A. Polyakov******, Academician **V. A. Glukhikh*******,
G. Sh. Manukyan*****, **V. A. Krylov*******, **V. A. Vesnin*******, **V. A. Parkhomenko*******,
E. M. Sukharev*****, and **Ya. I. Malashko*******

Received August 25, 1999

1. As a result of developing autonomous pulsed magnetohydrodynamic (MHD) generators [1–3], the “Sakhalin” MHD power system was constructed in Russia, which operates by combusting the solid (powder) plasma-forming propellant (see Fig. 1). This system is now the most powerful in the world (the electric power in the channel amounts to 600 MW). Using such a large-scale power system (plasma flow rate amounts to 1000 kg/s) with a high-temperature working medium (T_0 up to 3900 K) and electrical conduction $\sigma \geq 50$ S/m, $\sigma u^2 \geq 200$ (S/m) (km/s)² and employing to a great extent advantages associated with three-dimensional nature of MHD energy conversion, we have managed to attain the MHD interaction factor $S_i = \sigma B^2 L / \rho u \geq 1$. This enabled us to obtain extremely high operating parameters and unique specific characteristics.

2. Components of the “Sakhalin” MHD power system are typical of the autonomous pulsed MHD power systems operating with a solid plasma-forming propellant [1–3].

Plasma generator represents a combustion chamber for a solid plasma-forming propellant with additives of salts of cesium or potassium. The propellant combustion rate depended on pressure inside the plasma generator, as well as on the propellant temperature, and varied from 1 to 1.7 cm/s. The plasma-generator case was constructed of a glass-fiber material and has the shape of a cylinder 1.8 m in diameter and 4.5 m long. Seven cylindrical charges of solid plasma-forming propellant each 0.55 m in diameter and 3.72 m long are placed inside the case along its longitudinal axis. This provides a necessary value and desired time-dependence for pressure inside the plasma generator ($p_0 \approx \text{const}$). The combustion-product pressure inside the plasma generator varied within the range from 4 to 5.7 MPa; the designed temperature was 3800–3900 K. The propellant mass amounted to 5800–6200 kg, while the plasma-generator total mass attained 7500 kg.

The subcritical and critical parts of a graphite-supersonic nozzle are located in the rear cover of the plasma generator. The critical cross section has a rectangular shape close to the quadratic one with an area of 0.272 m².

MHD channel. The Faraday-type MHD channel with continuous electrodes of the rectangular cross section was used in the “Sakhalin” power system. Designed plasma parameters at the input of the MHD channel are the following. Pressure is 0.25–0.35 MPa, temperature $T \sim 2750$ K, the Mach number (according to the mixture parameters) is 2.4, the velocity is 2050 m/s, the electrical conduction is ~ 50 S/m, the electron mobility is 0.17–0.25 T⁻¹, and the near-electrode voltage drop is 200 V.

The gas-dynamic contour of the MHD channel consists of three sections: the accelerating section (1.29-m long supersonic part of the nozzle), the electrode section, and the diffuser one (1.3 m long). The electrode zone is 4.5 m long, the areas of the input and output cross sections are 1.0 m × 0.9 m and 1.0 m × 1.6 m,

* Russian Research Center Kurchatov Institute,
pl. Kurchatova 1, Moscow, 123182 Russia

** Troitsk Institute for Innovation
and Thermonuclear Research, Troitsk,
Moscow oblast, 142092 Russia

*** AO “Nizhegorodskii Machine-Building Plant,”
Nizhniĭ Novgorod, Sormovskoe sh. 21,
603052 Russia

**** Federal Centre of Dual Technologies “Soyuz,”
Dzerzhinskii, Moscow oblast,
ul. Sovetskaya 6, 140056 Russia

***** Efremov Institute of Electrophysical Equipment, St.
Petersburg, Metallostroi,
Sovetskii pr. 1, 189631 Russia

***** Scientific Research Institute “Geodeziya,”
Krasnoarmeisk, Moscow oblast,
ul. Tsentral'naya 16, 141260 Russia

***** Central Design Bureau “Almaz,”
Leningradskoe sh. 80, Moscow,
125190 Russia

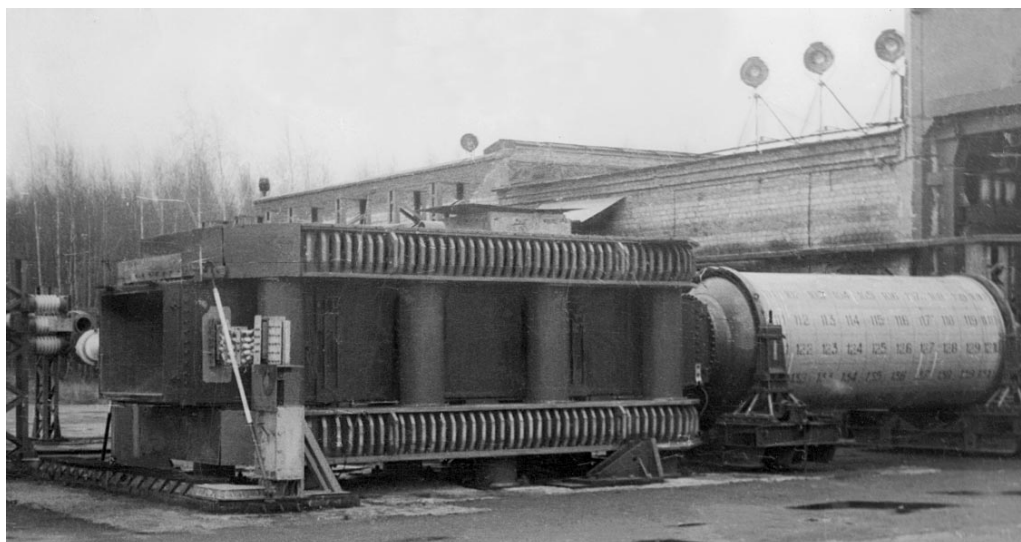


Fig. 1. General view of the “Sakhalin” MHD power system on a test bed.

respectively. Graphite modules $93 \text{ mm} \times 93 \text{ mm}$ in area and 25 mm thick, which are attached to copper bars each with a cross section of $10 \text{ mm} \times 45 \text{ mm}$. The total thickness of electrode walls amounts to 70 mm.

Insulating walls in the electrode and exhaust zones are formed by two-layer plates each 50 mm thick. The electrode walls and insulating ones form a box placed inside the stainless-steel load-bearing frame.

Basic parameters of the MHD channel are the following. The electric-current intensity is $\sim 200 \text{ kA}$, the voltage $\sim 2.5 \text{ kV}$, the power—600 MW. The energy-conversion coefficient amounts to 12%, the power density attains 100 MW/m^3 , the specific energy yield is close to 0.7 MJ/kg , the mass is $\sim 6 \text{ t}$.

Magnetic system. In order to provide the magnetic-field induction within the working space of the MHD channel, the iron-free magnetic system was used. The electromagnet consists of two plane trapezoidal (race-track) coils with a rectangular cross section of $0.4 \text{ m} \times 0.75 \text{ m}$, and of the load-bearing frame. Each coil consists of four isolated sections with independent terminals, that enables us to change their connection. Non-cooled windings (with the filling factor of 0.7) are manufactured from an aluminum-alloy bar with the cross section of $46 \text{ mm} \times 46 \text{ mm}$. Their heating attained $\sim 30 \text{ K}$ in a time of the pulse duration. The load-bearing frame is a welded leak-tight structure made of titanic alloy (see Fig. 1). The masses of the winding and the magnet are 16.5 t and $\sim 30 \text{ t}$, respectively.

Basic parameters of the electromagnet are: the induction is lower than 2.5 T, the field inhomogeneity along the channel is lower than 15% at the edges, the magnet constant is $\alpha_0 = B_0/I_m = 0.045 \text{ T/kA}$, the inductance is 6.5 mH (in the case of the self-excitation), the number of winding sections to be switched is four, the nominal current intensity is 50 kA, the energy stored is $\sim 100 \text{ MJ}$.

Inductive storage is employed as a load of the MHD generator. This device is used to store electrical energy up to 600 MJ. The inductive storage is an iron-free cylindrical solenoid formed by four sections 5.3 m in height and 4.9 m in diameter with its mass equal to 39 t. The sections are electrically isolated from each other and are supplied with independent terminals. An aluminum-alloy bar with the cross section of $45 \text{ mm} \times 230 \text{ mm}$ is used as a winding conductor. The current-carrying winding serves also as a load-bearing element resisting to tearing forces.

Basic parameters of the inductive storage are the following. The inductance is 30 mH, the resistance is $3.5 \text{ m}\Omega$, the electrical current should be lower than 210 kA, the magnetic-field induction attains up to $\sim 2 \text{ T}$, the stored-energy density per mass and volume units are 15 MJ/t and 1 MJ/m^3 , respectively.

The initial magnetic field within the MHD-channel space is produced by the initial excitation system based on the condenser battery (1920 units, two sections): the maximum voltage amounts to 5 kV, the total capacity is 0.27 F, the maximum accumulated energy is 0.65 MJ, the maximum discharge current is 50 kA, and the mass is 9300 kg.

In order to provide the energy extraction to the load and a desired commutation of the magnet sections, we have developed switching equipment: high-current one-shot connecting (CS) and disconnecting (DS) switches and commutating devices (CD) including CS and DS; powerful ballast resistors (R), and valve devices (V).

3. A circuit diagram and operating mode of the MHD power system. The operating mode of the MHD power system is governed by commands (cyclogram) realized by a control system.

Figure 2 presents the circuit diagram for the MHD power system. Here, D is an autonomously controlled

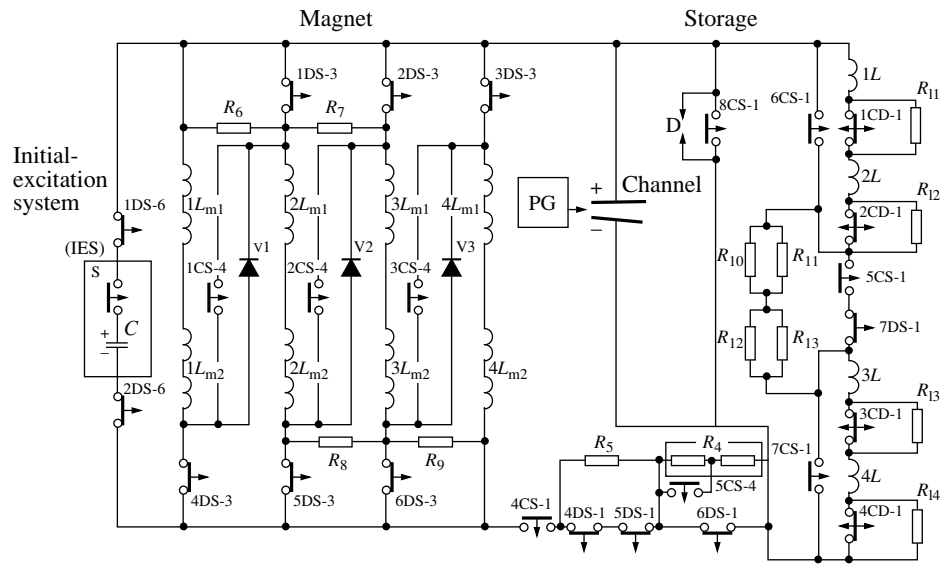


Fig. 2. Schematic circuit diagram of the MHD power system.

discharger, S is a switch connecting the initial excitation system (IES) to the electromagnet winding, R_6 – R_9 are resistors limiting the voltage at the 4DS–6DS and equalizing electrical currents in the sections; R_4 and R_5 are ballast resistors, R_{10} – R_{13} are resistors for the inductive-storage energy dissipation, R_1 is the load resistor.

Following the “plasma-generator start” command, in a prescribed time interval (1–2 s), connection of the initial-excitation system to the electromagnet-feed circuit occurs by switching on the S key. During ~ 0.1 s, the excitation current attains its maximum value $I_0 = (4\text{--}20$ kA), and generation of the current (power) in the MHD channel starts.

After the voltage at the MHD-channel clamps has exceeded that of the initial-excitation system, the magnet is connected to the MHD channel by means of the 4CS-1 contactor.

Further operating mode of the MHD power system is described by the designed (ideal) cyclogram (see Fig. 3, $p_k = 5.6$ MPa). In Fig. 3, a moment of switching on the initial-excitation system is chosen as the starting one. When the prescribed (initial) magnetic field B_{in} (or the magnet current $I_m \sim 50$ kA) is attained, the magnet windings are commutated anew by disconnecting the 1DS-1–6DS-3 and connecting the 1CS-4–3CS-4 contactors. Commutation overvoltages arising as a result of this process are suppressed by the R_6 – R_9 ballast resistors. To stabilize the magnetic field at the level attained, the R_4 (24 m Ω) ballast resistor is inserted into the magnet-feed circuit by actuating the 6DS-1 disconnecting device.

The 1L–4L inductive storage is connected in parallel to the MHD channel via the 5CS-1 contactor. In the first experiments, the R_{10} – R_{13} resistor block (with an equivalent resistance of 47.5 m Ω) was employed as a MHD-channel load instead of the inductive storage.

As the inductive-storage current I_s attains a prescribed value of ~ 150 kA, the energy extraction to the load occurs by disconnecting the 1CD–4CD contactors. The energy extracted is monitored according to the both CD disconnecting time and load parameters. After the energy has been extracted, the load current is cut off by connecting the 1CD–4CD devices, and the MHD system returns again to the energy-storing regime.

4. Results of the experimental investigations.

Tests of MHD-power system components have verified their expected properties. After assembling the MHD-power system and placing it on the test bed (see Fig. 1), the experiments with the MHD generator, which had been aimed at studying its self-excitation and the MHD generation of electrical energy, were performed. The results of two such experiments (nos. 1 and 2) are presented in the table.

In these experiments, the parallel connection of four magnet sections was used during the entire run of the MHD-generator tests. In order to provide reliable self-excitation, the maximum current in the initial-excitation system was set to be sufficiently large ($I_0 \approx 18$ kA).

In the course of the experiment no. 1, at the moment of 3.1 s after the propellant had been ignited, the initial excitation system was switched on. Within 0.1 s, the magnet current I_0 attained the value $I_0 = 18.4$ kA, and self-excitation of the MHD generator started. In 4.3 s, the currents of the both magnet and channel had increased up to ~ 130 kA, whereupon (at the time point of 4.4 s), the ohmic load with the equivalent resistance of 47.5 m Ω was connected in parallel to the channel. In this case, the load current was 40 kA, while the channel current has jumped up to 180 kA. In the channel, both the current and the voltage continued their increasing, and to the moment of 5.3 s, they attained 200 kA and 2.55 kW, respectively, while the power reached the

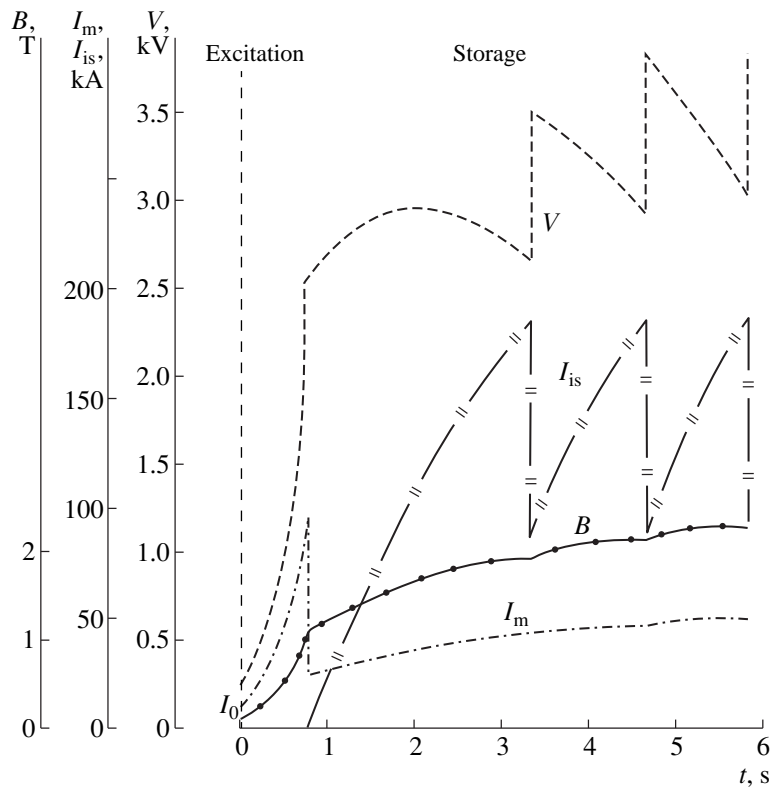


Fig. 3. Designed cyclogram of the MHD-power system operation.

value of 510 MW. To that time, the electromagnet current increased from 130 to 150 kA at a voltage of ~1.2 kV, i.e., the electromagnet has consumed ~35% of the power generated.

Furthermore, within the time interval from 5 to 7 s, the electrical parameters of the channel and magnet became stable at the level of $I_{ch} \approx 190$ kA, $I_m \approx 150$ kA, $B_0 \approx 2$ T, $V_{ch} \approx 2.3$ kV, $V_1 \approx 2$ kV and $V_m \approx 1.2$ kV.

Following the propellant-combustion attenuation, generation of the electric-power N_e in the MHD channel decreased during the time from 7 to 7.4 s, while the

magnetic field and the current inside the magnet (I_m, V_m) attenuated until ~7.8 s.

In the experiment no. 2, the self-excitation regime proceeded similarly to that in experiment no. 1. At the time of 4.36 s after the propellant-combustion had been started (the initial-excitation system had been switched on at $t = 2.57$ s) the channel current attained the value of $I_{ch} = I_m = 170$ kA ($V_{ch} = 2.86$ kV). To the time point $t = 4.58$ s, the values of electrical quantities were: $I_{ch} = I_m = 193$ kA, $N_e = 502$ MW, $V_{ch} = 2.6$ kV, $B_0 = 2.2$ T, $p_2 = 0.3$ MPa. Furthermore, (after the time moment

Table 1. Basic results of typical complex experiments

Test number	Charge mass, kg	Time of charge combustion, s	Plasma-generator maximum pressure, atm	Initial current without excitation, kA	Nominal current in the MHD channel, kA	Voltage, kV	Maximum power, MW	Magnetic-field induction, T	Electromagnet maximum current I_m , kA	Inductive-storage maximum current I_{is} , kA	Electromagnet-net-power fraction	Current (energy) gain factor
1	5780	7.37	45.5	18.4	200	2.55	510	2.09	152	—	0.35	10.9(118)
2	5810	7.52	43.7	17.4	193	2.6	502	2.2	190	—	—	11(121)
3	6460	8.64	43.5	6.1	195	1.41	275	1.5	56.1	165	0.28	32(1022)
4	6260	8.17	44.4	4.4	209	1.75	365	1.54	52.5	156	0.25	47.5(2256)
5	6146	7.71	46.8	4.54	180	2.16	388	1.54	52.6	126	0.29	40(1600)
6	6170	7.98	46.3	3.94	200	1.86	372	1.55	56	141	0.28	50.8(2577)

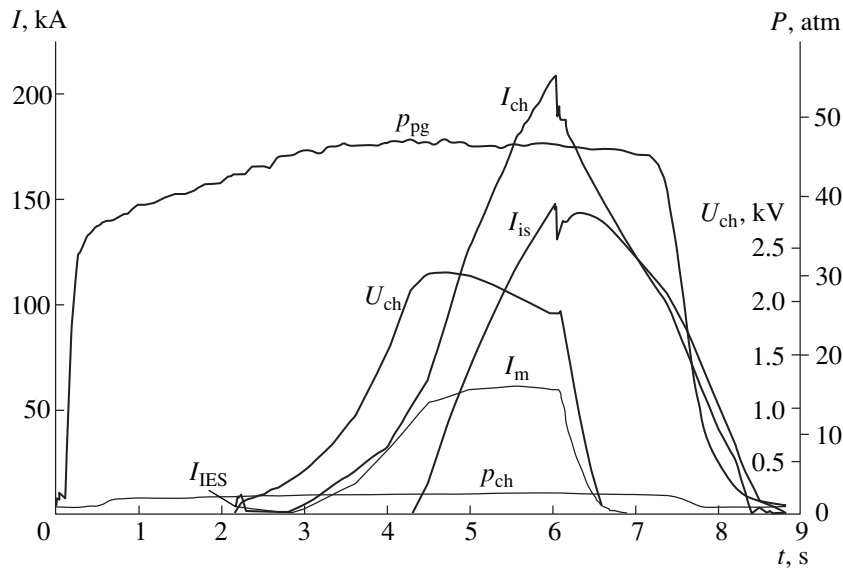


Fig. 4. Variation of MHD-power system key parameters in the experimental run no. 6.

$t = 4.6$ s), the MHD-channel operating mode was close to the short-circuit regime: the current has jumped up to $I_{ch} = 291$ kA, while the voltage has fallen down to 0.2–0.4 kV. In this process, the static pressure at the channel-input has increased up to its maximum value $p_1 = 0.35$ MPa (with the 0.4 s delay), while at the output, it has increased up to 0.48 MPa, i.e., by the factor of four compared to the jump-free damping of the supersonic flow. The current inside the magnet had attained the maximum value of 240 kA, then it has dropped to zero in the time of 2.5 s (to the time point $t = 7$ s).

As a result of the MHD-generator tests, we have made the following conclusions:

The operation of the plasma generator at $p_0 \approx 4.5$ MPa and the mass flow rate of 800 kg/s appeared to be stable and reproducible.

Properties of plasma formed as a result of combustion of the powder propellant are close to expected ones [$\sigma_{ch} \approx 50$ S/m, $\sigma_{ch} u_{ch}^2 \geq 200$ (S/m) (km/s)²].

In the case when four electromagnet sections are connected in parallel, and the initial current within the initial-excitation system is ~ 17 kA, the self-excitation time is ~ 1.5 s, and the current-amplification factor is 11, while the energy-gain factor (with respect to the energy accumulated in the magnet) amounts to 120.

The MHD channel provides the electrical-power generation at the 500-MW level.

The MHD channel can operate efficiently in the separation-flow regime and in the pseudo-jump one; the MHD power system carrying the short-circuit regime;

After slightly repairing the fire surface of the gas-dynamic channel, the nozzle and the MHD channel can be employed for further experiments.

We have also performed a series of experimental runs with the inductive storage of energy and its extraction into the R_1 ohmic load (see Fig. 2). The results for four typical events are presented in Table 1 (runs nos. 3–6).

A typical experimental cyclogram for the operation of the MHD-power system is presented in Fig. 4 (run no. 6 in Table 1). For all of the four experiments nos. 3–6, in spite of their noticeable differences, there are the following common properties.

The initial currents I_0 were 4–6 kA that resulted in a time delay of the MHD-generator self-excitation up to ~ 2 s, and even to short-term attenuating the magnetic field (the current). After the current intensity in the magnet had attained a prescribed (nominal) value $I_m = I_{ch}$, the required commutation of the magnet block from the parallel-connection regime to the series-parallel one (2×2) occurred. At the same time, a ballast resistor was inserted into the magnet circuit by means of two disconnecting devices. This resulted in stabilization of the magnetic-field induction (i.e., current) at a level of 1.5 T (~ 50 kA). With the parallel connecting an active-inductive load to the MHD channel (at $t = 4$ –5 s after the combustion had started), an increase of the currents in the both channel and inductive storage began (from ~ 50 to 200 kA and from zero to ~ 150 kA, respectively). These currents reached their maximum (designed) values within 2.0 to 2.5 s.

Up to this moment, the fraction of the power consumed by the magnet has attained 25% of the total power generated and even lower with allowance for the ballast resistor introduced into the magnet circuit. The current-amplification factor in the MHD-channel-magnet system arrived at $I_m/I_0 = 30$ –50, while the gain factor for the energy stored in the magnet (~ 100 MJ) attained 1000 to 2000. The maximum energy accumulated in the

inductive storage was close to 420 MJ, and even 680 MJ (run no. 4) with the extracted energy taken into account.

In the runs nos. 3–6, the energy extraction from the inductive storage to the $\sim 0.1\text{-}\Omega$ load has been carried out by two pulses with a short time gap between them. In this case, the desired current value (~ 150 kA) was attained. Usually, it happened within the time interval of 5–6 s after the fuel had been ignited (Fig. 4). Initially, the energy was extracted from the first and third sections of the inductive storage (provided by the 1CD-1 and 3CD-1 commutating devices), and then, from the second and fourth ones (2CD-1 and 4CD-1). The relative energy extracted to the load amounted to 10–30%.

After the energy has been extracted to the load, the R_5 ballast resistor was introduced into the magnet circuit, which resulted in fast attenuation of both the magnet current I_m and the magnetic field (Fig. 4). In this case, the current from the inductive storage began to flow in the MHD channel. After disappearance of the magnetic field, this current became to be equal to time-decreasing current of the inductive storage. As a result, all the electrical parameters attenuated in a time exceeding by 1 to 2 s that of the existence of the plasma flow (see Fig. 4).

We observed no noticeable visible damages of basic elements and electrical insulation of the MHD power system. The damages of the fire surfaces of MHD-channel walls exhibited erosive nature and corresponded to expected bounds.

5. As a result of performing a vast amount of calculated-theoretical, design-technological, and experimental work, we succeed in constructing and testing the “Sakhalin” autonomous pulsed MHD power system that is the most powerful in the world and operates with a powder (solid) propellant. This power system exhibits record parameters and unique specific characteristics presented in Table 2.

The “Sakhalin” MHD power system is the most powerful of the series of autonomous pulsed solid-propellant MHD systems constructed in Russia, such as “Pamir,” “Ural,” “Soyuz,” and “Khibiny.”

Plasma-forming powders [4] have opened a fundamentally new tendency in the field of pulsed-power engineering. In contrast to solid propellants, their distinctive feature is a higher (by four orders of magnitude) electrical conduction of the combustion products at a rather low (~ 3800 K) burning temperature. There exists an actual feasibility to increase electrical conduction even more by a factor of 1.5 to 2. Physicochemical and strength characteristics of the powders make it possible to develop plasma generators with a charge mass within the range from several tens of grams to several tens of tons. These generators are capable of operating within the temperature range of $\pm 40^\circ\text{C}$, with the storage stability being guaranteed for decades. The charge production is provided by the uninterrupted-automated technology with the remote control and inspection that is very important in the case of employing high-power

Table 2. Basic parameters of the “Sakhalin” MHD power system

Consumption-product mass flow rate	720–1000 kg/s
Electric-energy generation time	5–6 s
Electric power of the MHD channel	510 MW
MHD-channel nominal current	200 kA
Nominal voltage	2.5 kV
Maximum energy accumulated in a pulse	up to 600 MJ
MHD-generator mass (without IES)	50 t
MHD-generator size (length \times width \times height)	13.5 m \times 3.7 m \times 2.7 m
Energy-transformation efficiency	12%
Power density in the MHD channel	90 MW/m ³
Specific energy output per fuel unit mass	0.65 MJ/kg
Energy extracted per fuel unit mass	up to 0.15 MJ/kg
Gain factor for the energy extracted	up to 650
Specific MHD-generator mass per power unit	0.1 t/MW
Specific volume of the MHD generator	0.3 m ³ /MW
Mass energy density	5 MJ/t
Volume energy density	0.5 MJ/m ³

condensed substances (powders). The “Sakhalin” MHD power system and the experimental results obtained in the process of its tests have shown that the modern status of science and engineering enables us to construct compact autonomous MHD systems of short-term operation. These facilities provide a power of ~ 1 GW and an electric-energy accumulation up to several gigajoules at an energy density of ~ 10 MJ/t, i.e., ~ 1 MJ/m³.

REFERENCES

1. E. P. Velikhov and Yu. M. Volkov, *Perspectives of Development of Pulsed MHD Power Engineering and Its Application in Geology and Geophysics*, Preprint no. IAE-3446 (Kurchatov Institute of Atomic Energy, Moscow, 1981).
2. V. V. Breev, A. V. Gubarev, and V. P. Panchenko, *Supersonic MHD Generators* (Moscow, Énergoizdat, 1988).
3. *Geophysical–Electrical Investigations with a Powerful Current Source at the Baltic Geological Platform*, Ed. by E. P. Velikhov (Moscow, Nauka, 1989).
4. B. P. Zhukov, Zh. Vsesoyuz. Khim. O–va **45**, 84 (1991).

Translated by O. Chernavskaya

On Critical Modes of an Inhomogeneous Plate

Yu. A. Ustinov

Presented by Academician V.V. Vorovich March 31, 1999

Received April 13, 1999

1. We consider harmonic vibrations of a plate $x, y \in S, 0 \leq z \leq h$, whose elastic characteristics $\lambda = \lambda(z)$, $\mu = \mu(z)$, and the density $\rho = \rho(z)$ are positive piecewise continuous functions of the variable z and whose faces ($z = 0, z = h$) are stressless. We will seek the solution of equations of the elasticity theory in the following form

$$\begin{aligned} u_x &= a_1(z)m_{1,x}(x, y) + a_3(z)m_{2,y}(x, y), \\ u_y &= a_1(z)m_{1,y}(x, y) - a_3(z)m_{2,x}(x, y), \\ u_z &= ik a_2(z)m_1(x, y), \end{aligned} \quad (1)$$

$$\Delta m_\alpha + k^2 m_\alpha = 0, \quad \Delta = \frac{\partial^2}{\partial x^2} + \frac{\partial^2}{\partial y^2}, \quad \alpha = 1, 2.$$

After separating variables, we arrive at the spectral problems:

(i) relative to a pair of functions $\mathbf{a} = \{a_1, a_2\}$

$$\begin{aligned} L(ik, \omega)\mathbf{a} &\equiv \{-k^2 C\mathbf{a} + ik[(B\mathbf{a})' + B^*\mathbf{a}'] \\ &+ (A\mathbf{a}') + \rho\omega^2\mathbf{a}, (A\mathbf{a}' + ikB\mathbf{a})|_{z=0,h}\} = 0, \end{aligned} \quad (2)$$

$$C = \begin{bmatrix} \lambda + 2\mu & 0 \\ 0 & \mu \end{bmatrix}, \quad B = \begin{bmatrix} 0 & \mu \\ \lambda & 0 \end{bmatrix},$$

$$B^* = \begin{bmatrix} 0 & \lambda \\ \mu & 0 \end{bmatrix}, \quad A = \begin{bmatrix} \mu & 0 \\ 0 & \lambda + 2\mu \end{bmatrix};$$

and (ii) relative to a_3

$$(\mu a_3)' - [k^2\mu - \rho\omega^2]a_3 = 0, \quad a_3|_{z=0,h} = 0. \quad (3)$$

Here, ω is the cyclic frequency of vibrations.

We denote the spectra of the problems (2) and (3) with respect to the parameter k by $\Lambda_1(\omega)$ and $\Lambda_2(\omega)$, respectively.

Statement 1. *The spectra $\Lambda_1(\omega)$ and $\Lambda_2(\omega)$ are symmetric sets. For any real value of the frequency ω , $\Lambda_1(\omega)$ consists of a bounded set of real eigenvalues and*

denumerable set of complex eigenvalues, and $\Lambda_2(\omega)$ consists of a bounded set of real eigenvalues and denumerable set of imaginary eigenvalues.

Remark 1. A more comprehensive description of eigenvalues, eigenfunctions, and associated functions can be found, for example, in [1, 2].

The homogeneous fundamental solutions of the form

$$\begin{aligned} u_{xp} &= a_{1p}(z)m_{1p,x}(x, y), \\ u_{yp} &= a_{1p}(z)m_{1p,y}(x, y), \\ u_{zp} &= ik_p a_{2p}(z)m_{1p}(x, y), \end{aligned} \quad (4)$$

$$\Delta m_{1p} + k_p^2 m_{1p} = 0,$$

$$u_{xv} = a_{3v}(z)m_{2v,y}(x, y),$$

$$u_{yv} = -a_{3v}(z)m_{2v,y}(x, y), \quad u_{zv} = 0, \quad (5)$$

$$\Delta m_{2v} + k_v^2 m_{2v} = 0,$$

correspond to the ordinary eigenvalues $k_p \in \Lambda_1$ and $k_v \in \Lambda_2$.

Theorem 1. *If the spectra $\Lambda_1(\omega)$ and $\Lambda_2(\omega)$ consist of only nondegenerate eigenvalues, then any homogeneous solution (meeting the condition of zero stress at $z = 0$ and $z = h$) can be presented as a finite or infinite sum of fundamental solutions (4) and (5). In this case, if S is an unbounded domain, the solutions of the Helmholtz equations, which correspond to either real or complex values of k_p and k_v , can be chosen on the basis of either the energy conservation principle for radiation [1, 3, 4] or the condition of damping, respectively.*

Remark 2. The proof of a similar theorem, which was given for a static problem in [5], can be applied, with insignificant modifications, to the case of stationary vibrations under consideration.

2. Assume that k_c is a degenerate eigenvalue and ω_c is the critical frequency at which this k_c appears. The pair (k_c, ω_c) and the fundamental solutions corresponding to it will be referred to as the critical pair and the critical modes, respectively. We restrict ourselves by the description of the most typical cases when $k_c = 0$.

Substituting $k = 0$ into (2) and (3) gives two self-conjugate spectral problems of determining the critical frequencies:

$$(\mu\varphi^{(1)})' + \rho\omega^2\varphi^{(1)} = 0, \tag{6}$$

$$\varphi^{(1)}|_{z=0,h} = 0,$$

$$[(\lambda + 2\mu)\varphi^{(2)}]' + \rho\omega^2\varphi^{(2)} = 0, \tag{7}$$

$$\varphi^{(2)}|_{z=0,h} = 0.$$

Here, equation (6) is a result of the indicated substitution both into relations (2) ($a_1 = \varphi^{(1)}$) and (3) ($a_3 = \varphi^{(1)}$), and equation (7) follows from (2) ($a_2 = \varphi^{(2)}$).

We denote the sets of eigenvalues of problems (6) and (7) by $\{\omega_n^{(1)}\}$ and $\{\omega_n^{(2)}\}$ ($n = 1, 2, \dots$), respectively.

Let $\varphi_{r0}^{(1)}$ be the eigenfunction, and $\omega_c = \omega_r^{(1)}$, with

$$\lambda_r = \int_0^h [\lambda\varphi_{r1}^{(1)}\varphi_{r0}^{(1)} + \lambda(\varphi_{r0}^{(1)})^2 - \mu\varphi_{r0}^{(1)}\varphi_{r1}^{(1)}] dz,$$

$$\mu_r = \int_0^h \mu(\varphi_{r0}^{(1)})^2 dz,$$

$$d_r^{(1)} = \lambda_r + 2\mu_r.$$

Here, $\varphi_{r1}^{(1)}$ is a solution of the boundary-value problem

$$[(\lambda + 2\mu)\varphi_1'] + \rho(\omega_r^{(1)})^2\varphi_1 = -(\lambda\varphi_{r0}^{(1)})' - \mu\varphi_{r0}^{(1)},$$

$$[(\lambda + 2\mu)\varphi_1' + \lambda\varphi_{r0}^{(1)}]_{z=0,h} = 0.$$

Statement 2. If $d_r^{(1)} \neq 0$, the root subspace of problem (2), which corresponds to the critical pair $\{0, \omega_r^{(1)}\}$, consists of the eigenvector $\mathbf{a}_{r0}^{(1)} = \{\varphi_{r0}^{(1)}, 0\}$ and the adjoint vector $\mathbf{a}_{r1}^{(1)} = \{0, i\varphi_{r1}^{(1)}\}$. The general form of the fundamental solution is as follows:

$$\begin{aligned} u_x^{(1)} &= \varphi_{r0}^{(1)}b_x + \varphi_{r2}^{(1)}\theta_{,x}, \\ u_y^{(1)} &= \varphi_{r0}^{(1)}b_y + \varphi_{r2}^{(1)}\theta_{,y}, \quad u_z^{(1)} = \varphi_{r1}^{(1)}\theta. \end{aligned} \tag{8}$$

Here, the function $b_x(x, y)$ and $b_y(x, y)$ satisfy the equations

$$\begin{aligned} (\lambda_r + \mu_r)\theta_{,x} + \mu_r\Delta b_x &= 0, \\ (\lambda_r + \mu_r)\theta_{,y} + \mu_r\Delta b_y &= 0, \quad \theta = b_{x,x} + b_{y,y}, \end{aligned} \tag{9}$$

that formally coincide with equations of the elasticity theory in the plane case. The function $\varphi_2 = \varphi_{r2}^{(1)}$ is the

solution to the problem

$$\begin{aligned} (\mu\varphi_2') + \rho(\omega_r^{(1)})^2\varphi_2 &= -\lambda\varphi_{r1}^{(1)} - (\mu\varphi_{r1}^{(1)})' + (\mu\lambda_r/\mu_r - \lambda)\varphi_{r0}^{(1)}, \\ (\varphi_2' + \varphi_{r1}^{(1)})|_{z=0,h} &= 0. \end{aligned}$$

Remark 3. If $\lambda_r + \mu_r \neq 0$, the functions b_x and b_y can be represented in terms of the biharmonic Airy functions Φ in the following way [6]:

$$\begin{aligned} 2\mu_rb_x &= -\Phi_{,xx} + Kp_x - \varepsilon y + c_x, \\ 2\mu_rb_y &= -\Phi_{,yy} + Kp_y + \varepsilon x + c_y, \end{aligned}$$

where ε , c_x , and c_y are arbitrary constants,

$$p_{x,x} = p_{y,y} = \Delta\Phi, \quad p_{x,y} = -p_{y,x},$$

$$\theta = \frac{\Delta\Phi}{2(\lambda_r + \mu_r)}, \quad K = \frac{d_r^{(1)}}{2(\lambda_r + \mu_r)}.$$

Statement 3. If $d_r^{(1)} = 0$ (the first exceptional case), there exist at least two (or just two, in the case of a homogeneous plate) additional adjoint vectors $\mathbf{a}_{r2}^{(1)} = \{\varphi_{r2}^{(1)}, 0\}$ and $\mathbf{a}_{r3}^{(1)} = \{0, i\varphi_{r3}^{(1)}\}$, where $\varphi_3 = \varphi_{r3}^{(1)}$ is a solution to the problem

$$[(\lambda + 2\mu)\varphi_3'] + \rho(\omega_r^{(1)})^2\varphi_3 = -(\lambda\varphi_{r2}^{(1)})' - \mu\varphi_{r1}^{(1)},$$

$$[(\lambda + 2\mu)\varphi_3' + \lambda\varphi_{r2}^{(1)}]_{z=0,h} = 0.$$

In this case, the fundamental solutions are determined by the relations

$$u_x^{(1)} = \varphi_{r0}^{(1)}b_x + \varphi_{r2}^{(1)}\theta_{,x},$$

$$u_y^{(1)} = \varphi_{r0}^{(1)}b_y + \varphi_{r2}^{(1)}\theta_{,y}, \quad u_z^{(2)} = \varphi_{r1}^{(1)}\theta + \varphi_{r3}^{(1)}C,$$

where C is an arbitrary constant. The functions b_x and b_y satisfy the equations

$$\Delta(b_{x,xx} + b_{y,xy}) = 0, \quad \Delta(b_{x,xy} + b_{y,yy}) = 0. \tag{10}$$

Remark 4. In this case,

$$2\mu_rb_x = -\Phi_{,xx} - \varepsilon y + c_x,$$

$$2\mu_rb_y = -\Phi_{,yy} + \varepsilon x + c_y, \quad \Delta^2\Phi = 2(\lambda_r + \mu_r)C.$$

Let $\varphi_{r0}^{(2)}$ be the eigenfunction and $\omega_c = \omega_r^{(2)}$, with

$$d_r^{(2)} = \int_0^h [\mu\varphi_{0r}^{(2)}\varphi_{r1}^{(2)} + \mu(\varphi_{0r}^{(2)})^2 - \lambda\varphi_{0r}^{(2)}\varphi_{1r}^{(2)}] dz.$$

Statement 4. If $d_r^{(2)} \neq 0$, the root subspace of problem (2), which corresponds to the critical pair

$\{0, \omega_r^{(2)}\}$, consists of the eigenvector $\mathbf{a}_{r0}^{(2)} = \{0, \varphi_{r0}^{(2)}\}$ and the adjoint vector $\mathbf{a}_{r1}^{(2)} = \{i\varphi_{r1}^{(2)}, 0\}$. The general form of the fundamental solution is as follows:

$$\begin{aligned} u_x^{(2)} &= \varphi_{r1}^{(2)} b_{z,x}, & u_y^{(2)} &= \varphi_{r1}^{(2)} b_{z,y}, \\ u_z^{(2)} &= \varphi_{r0}^{(2)} b_z, & \Delta b_z &= 0. \end{aligned} \quad (11)$$

Here, $\varphi_{r1}^{(2)}$ is a solution to the problem:

$$\begin{aligned} (\mu\varphi_1') + \rho(\omega_r^{(2)})^2 \varphi_1 &= -\lambda\varphi_{r0}^{(2)} - (\mu\varphi_{r0}^{(2)})', \\ (\varphi_1 + \varphi_{r0}^{(2)}) \Big|_{z=0,h} &= 0. \end{aligned}$$

Statement 5. If $d_r^{(2)} = 0$ (the second exceptional case), there exist at least two (or just two, in the case of a homogeneous plate) additional adjoint vectors $\mathbf{a}_{r2}^{(2)} = \{0, \varphi_{r2}^{(2)}\}$ and $\mathbf{a}_{r3}^{(2)} = \{i\varphi_{r3}^{(2)}, 0\}$, where $\varphi_{r2}^{(2)}$ and $\varphi_{r3}^{(2)}$ are solutions of the following problems:

$$\begin{aligned} [(\lambda + 2\mu)\varphi_2'] + \rho(\omega_r^{(2)})^2 \varphi_2 &= -(\lambda\varphi_{r1}^{(2)})' - \mu\varphi_{r1}^{(2)} - \mu\varphi_{r0}^{(2)}, \\ [(\lambda + 2\mu)\varphi_2' + \lambda\varphi_{r1}^{(2)}]_{z=0,h} &= 0, \end{aligned}$$

$$\begin{aligned} (\mu\varphi_3') + \rho(\omega_r^{(2)})^2 \varphi_3 &= -\lambda\varphi_{r2}^{(2)} - (\mu\varphi_{r2}^{(2)})', \\ (\varphi_3 + \varphi_{r2}^{(2)}) \Big|_{z=0,h} &= 0. \end{aligned}$$

In this case, the fundamental solutions are determined by the relations:

$$\begin{aligned} u_x^{(2)} &= \varphi_{r1}^{(2)} b_{z,x} + \varphi_{r3}^{(2)} \Delta b_{z,x}, \\ u_y^{(2)} &= \varphi_{r1}^{(2)} b_{z,y} + \varphi_{r3}^{(2)} \Delta b_{z,y}, \\ u_z^{(2)} &= \varphi_{r0}^{(2)} b_z + \varphi_{r4}^{(2)} \Delta b_z, & \Delta^2 b_z &= 0. \end{aligned} \quad (12)$$

Statement 6. If $\omega_c = \omega_r^{(1)} = \omega_m^{(2)}$ (the third exceptional case), two fundamental solutions correspond to the spectral pair, namely:

$$u_x^{(1)} = b_x \varphi_{r0}^{(1)}, \quad u_y^{(1)} = b_y \varphi_{r0}^{(1)}, \quad (13)$$

$$u_z^{(1)} = 0, \quad b_{x,x} + b_{y,y} = 0;$$

$$u_x^{(2)} = u_y^{(2)} = 0, \quad u_z^{(2)} = \varphi_{m0}^{(2)}. \quad (14)$$

The existence of the fundamental solutions of the form (13) and (14) follows from relations (8), (9), and (10) when b_x and b_y are constants. However, these relations and especially equations (11) and (12) admit the existence of the critical modes in which the displacement amplitudes infinitely increase with x and y , while the stress amplitudes remain bounded. As is known [6], similar properties are inherent in solutions of plane

static problems of the elasticity theory and problems of bending. In the first and second exceptional cases, the equations given above admit solutions with infinitely rising stress amplitudes. Therefore, for an unbounded plate, the solution may belong to a class of the generalized functions infinitely rising at $|x|, |y| \rightarrow \infty$. These fundamental solutions have no physical meaning because of two idealizations used, namely, we assumed the plate to be unbounded and the material to be perfectly elastic. However, the boundary-value problem can become intractable on account of the condition of finiteness for solutions. In the case of critical frequencies, a theorem similar to that given above can be formulated only if all the solutions meeting the above relations are taken into account. In the resonance case for an unbounded plate, the unique solution can be selected on the basis of the energy conservation principle for radiation by constructing specific fundamental solutions similar to those obtained in [2, 7].

3. We now consider a plate having a layered two-phase periodic structure with the period l . Each phase is characterized by the length l_β and the mechanical parameters λ_β, μ_β , and ρ_β ($\beta = 1, 2, l = l_1 + l_2$), with $h = Nl$, where N is a natural number. Employing the Floquet–Lyapunov theory [8] to equations (8) and (9), we can reduce the problem of determining the critical frequencies to the problem of finding the roots of the following equations:

$$\begin{aligned} \cos \gamma_n &= \cos(q_1^{(\alpha)}) \cos(q_2^{(\alpha)}) \\ &- \frac{1}{2} \left(\frac{k_1^{(\alpha)}}{p^{(\alpha)} k_2^{(\alpha)}} + \frac{p^{(\alpha)} k_2^{(\alpha)}}{k_1^{(\alpha)}} \right) \sin(q_1^{(\alpha)}) \sin(q_2^{(\alpha)}), \end{aligned}$$

$$q_\beta^{(\alpha)} = h_\beta k_\beta^{(\alpha)}, \quad k_\beta^{(\alpha)} = \frac{\omega}{c_\beta^{(\alpha)}},$$

$$c_\beta^{(1)} = \left(\frac{\mu_\beta}{\rho_\beta} \right)^{1/2}, \quad c_\beta^{(2)} = \left[\frac{\lambda_\beta + 2\mu_\beta}{\rho_\beta} \right]^{1/2},$$

$$p^{(1)} = \frac{\mu_2}{\mu_1}, \quad p^{(2)} = \frac{\lambda_2 + 2\mu_2}{\lambda_1 + 2\mu_1},$$

$$\gamma_n = \frac{n\pi}{N}, \quad n = 1, 2, \dots, \quad \alpha = 1, 2.$$

The following eigenfunction corresponds to each of the roots $\omega = \omega_{ns}^{(\alpha)}$ ($s = 1, 2, \dots$):

$$\begin{aligned} \varphi_{1ns}^{(\alpha)} &= C_{1ns}^{(\alpha)} y_{1ns}^{(\alpha)}(z - mh, r_n)^m \\ &+ C_{2ns}^{(\alpha)} y_{1ns}^{(\alpha)}(z - mh, r_n^{-1}) r_n^{-m} \end{aligned}$$

when $mh \leq z \leq mh + l_1, m = 0, \dots, N - 1$;

$$\begin{aligned} \varphi_{1ns}^{(\alpha)} &= C_{1ns}^{(\alpha)} y_{2ns}^{(\alpha)}(z - mh, r_n)^m \\ &+ C_{2ns}^{(\alpha)} y_{2ns}^{(\alpha)}(z - mh, r_n^{-1}) r_n^{-m} \end{aligned}$$

when $mh + l_1 \leq z \leq mh + l$.

Here, $y_{1ns}^{(\alpha)}(z - mh, r_n)$ and $y_{2ns}^{(\alpha)}(z - mh, r_n)$ are derived by the substitution of

$$z = z - mh, \quad r = r_n = \exp(i\gamma_n),$$

and

$$k_\beta = k_{\beta ns}^{(\alpha)} = \frac{\omega_{ns}^{(\alpha)}}{c_\beta^{(\alpha)}},$$

into the following equations:

$$y_1(z, r) = pk_1k_2 \cos(k_1(z - l_1)) + rp k_2 [pk_2 \sin q_2 \sin(k_1 z) - k_1 \cos(k_1 z) \cos(q_2)],$$

$$y_2(z, r) = rk_1 [k_1 \sin(q_1) \sin(k_1(z - l)) + pk_2 \cos(k_2(z - l) \cos(q_1)] - r^2 pk_1 k_2 \cos(k_1(z - l_1)),$$

$$C_1 = y_{1,z}(0, r_n^{-1}), \quad C_2 = -y_{1,z}(0, r_n).$$

The construction of the remaining functions mentioned in Statements 2–6 and the test for the fulfillment of various conditions can be carried out by a program similar to *Maple V*.

ACKNOWLEDGMENTS

This work was supported by the Russian Foundation for Basic Research, project no. 97-01-00-464.

REFERENCES

1. I. I. Vorovich and V.A. Babeshko, *Dynamic Mixed Problems of Elasticity Theory for Nonclassical Domains* (Nauka, Moscow, 1979).
2. I. P. Getman and Yu. A. Ustinov, *Mathematical Theory of Rigid Nonregular Waveguides* (Rostov State Univ. Press, Rostov-on-Don, 1993).
3. Yu. A. Ustinov, *Izv. Akad. Nauk, Ser. Mekh. Tverd. Tela*, No. 5, 87 (1991).
4. D. D. Zakharov, *Izv. Akad. Nauk, Ser. Mekh. Tverd. Tela*, No. 6, 62 (1988).
5. Yu. A. Ustinov, *Prikl. Mat. Mekh.* **40**, 236 (1976).
6. N. I. Muskhelishvili, *Some Fundamental Problems of Mathematical Theory of Elasticity* (Nauka, Moscow, 1966).
7. I. P. Getman and Yu. A. Ustinov, *Dokl. Akad. Nauk* **310**, 309 (1990).
8. B. P. Demidovich, *Lectures on Mathematical Theory of Stability* (Nauka, Moscow, 1967).

Translated by V. Chechin

Self-Maintained Glow Discharge in a Hypersonic Air Flow

Corresponding Member of the RAS V. M. Fomin*, T. A. de Roquefort**,
A. V. Lebedev*, and A. I. Ivanchenko*

Received August 31, 1999

The effects observed when a self-maintained glow discharge occurring in a supersonic gas flow interacts with shock waves are currently of considerable scientific interest [1–5]. It is established that the glow discharge can decrease the amplitude of the shock wave and increase the width of its front [3, 4]. It rearranges the pattern of the supersonic gas flow around the body. In particular, this manifests itself as a dissipation of the front shock [5]. Seemingly, the fact that the effects observed cannot be explained exclusively within the scope of a model of temperature distribution for a neutral gas should be considered as proven now [3, 4]. Therefore, energy characteristics of the supersonic gas flow with a discharge become important for discriminating “thermal” effects from “nonthermal” ones (associated with properties of plasma).

We have already established the fact [5] that, if the longitudinal glow discharge occurs at the incident-flow Mach number $M = 3.2$, the voltage in it drops noticeably only in the near-electrode regions. In addition, a model of the non-self-maintained discharge can be used to describe the potential distribution in a discharge gap except the near-electrode regions.

However, the effect of variation of the interelectrode spacing L , the static pressure P (the density ρ), and the incident-flow Mach number M on energy characteristics of the discharge remained completely unknown until now. Here, we are the first to present the results of the investigation that concerns the effect of the above-mentioned parameters on the voltage–current characteristic of a longitudinal self-maintained glow discharge occurring in a hypersonic air flow.

A setup used in the experiments to investigate the discharge was similar to that applied in [5]. A streamlined model body, i.e., a cylinder 8 mm in diameter, was placed in a hypersonic air flow ($M = 7.1, 8.15$ and $\rho =$

2.8×10^{-2} – 5.4×10^{-2} kg/m³). The cylinder spherical head served as a cathode, while the 0.2-mm plate shifted upstream and located in the plane of symmetry of the model body at a distance $L = 21$ – 52 mm from the cathode served as an anode. To localize the discharge, the anode had a triangular cusp at its back edge. Both the plate (the anode) and the cylinder (the cathode) were placed at the zero angle of incidence to the flow. A high-voltage power supply contained a full-wave rectifier without smoothing filters. The duration of measurement runs used for constructing each voltage–current characteristic was 10^{-2} s. Gas renewal in the discharge occurred during the characteristic time of 2×10^{-5} – 5×10^{-5} s. Therefore, with respect to processes in the discharge, these characteristics can be considered as steady-state. Duration of each experiment was 10 s. In this period, the voltage–current characteristics were measured and recorded automatically about 10^3 times.

Figure 1 presents the discharge appearance in the hypersonic air flow at $M = 8.15$. The pattern is almost the same as at $M = 7.1$ and similar to that observed at $M = 3.2$ in [5]. The volume occupied by the discharge (the non-near-electrode zones) has the shape of a cylinder of about 3 mm in diameter, which turns into a cone near the head, i.e., near the cathode of the streamlined body. The cathode layer, characteristic for glow discharges, forms at the cathode. Photographing shows that the thickness of the layer is about 0.6 mm. In our experiments, the characteristic maximum current density observed at the cathode was 0.38 A/cm². The same quantity in the volume occupied by the discharge took the value 4.7 A/cm². Variation of the interelectrode spacing did not affect the shape of the near-cathode region of the discharge but changed the length of the discharge-occupied volume. To visualize the wave pattern of the flow around the body, we applied the shadow method. The results obtained by us are similar to those presented in [5]: the discharge causes dissipation of the shock wave in front of the blunt part of the body.

Figures 2–4 show the voltage–current characteristics. Each curve presented is obtained by averaging several thousands of experimental results. The dependence of the voltage between the anode and cathode on the strength of the electric current exhibits a pronounced hysteresis: two values of the voltage can correspond to

* *Institute of Theoretical and Applied Mechanics, Siberian Division, Russian Academy of Sciences, ul. Institutskaya 4/1, Novosibirsk, 630090 Russia*

** *Centre d'Etudes Aérodynamiques et Thermiques, Route de l'Aérodrome 43, 86036 Poitiers Cedex, France*

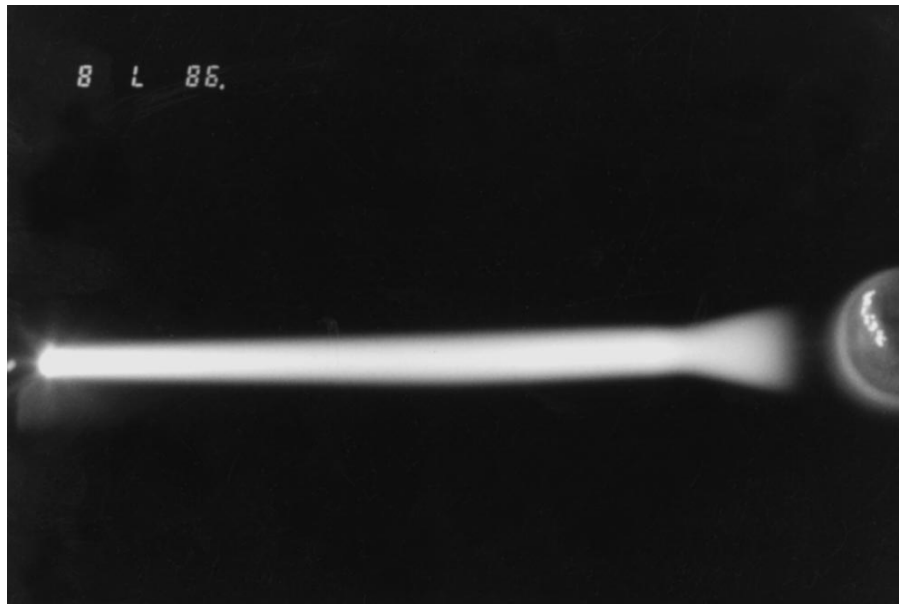


Fig. 1. Discharge appearance at $M = 8.15$.

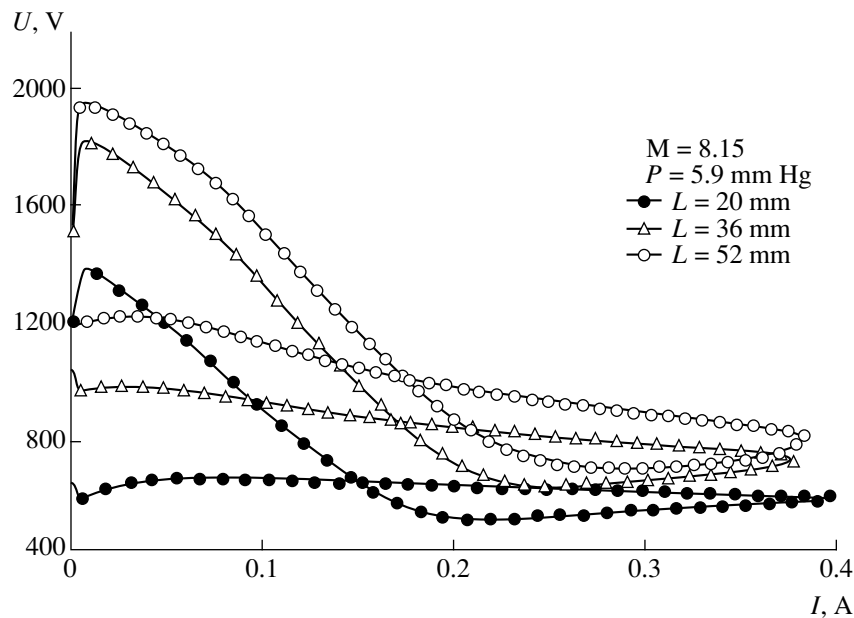


Fig. 2. Effect of the electrode spacing on the voltage–current characteristics.

one value of the current in the discharge. The direction of movement around the hysteresis loop is identical for all of the curves and is shown by arrows in Fig. 4. Each of the voltage–current characteristics can be divided into two parts. In accordance with the direction of movement around the hysteresis loop, the first part begins at the maximum value of the voltage and ends in the region of its minimum. It corresponds to the discharge ignition and is characterized by both the short duration and increased spread of the experimental

results. Going further along the voltage–current characteristic, we traverse its second (main) part. It corresponds to the dominant part of the discharge duration and is characterized by high reproducibility. Analyzing this region allows the following conclusions to be drawn. Within the range of variation of the parameters investigated, the interelectrode spacing affects the voltage–current dependence most strongly. Increasing the interelectrode spacing enhances both the discharge-gap voltage and the effect of hysteresis. An increase in the

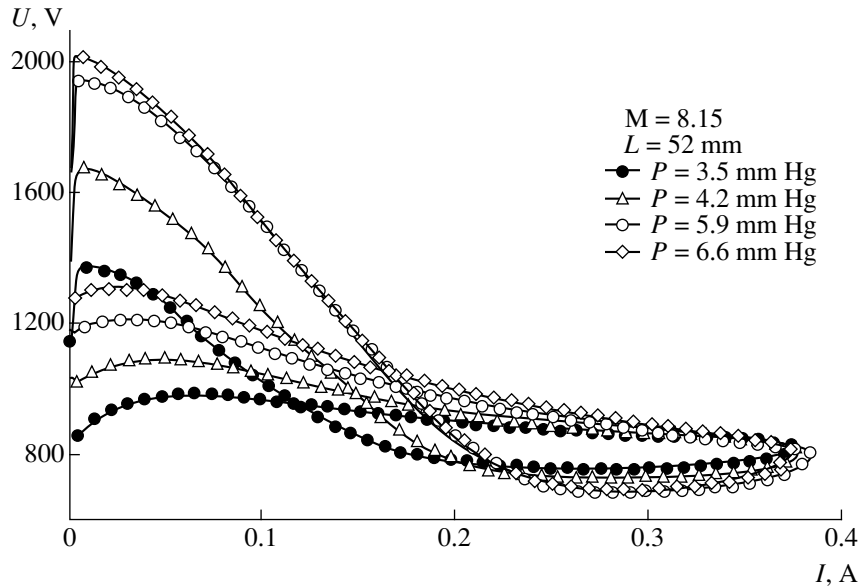


Fig. 3. Effect of static pressure on the voltage–current characteristics.

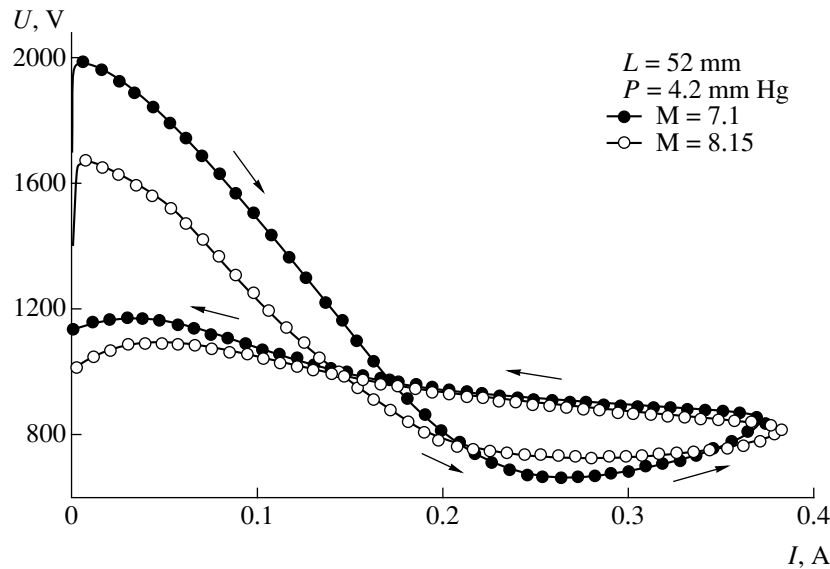


Fig. 4. Effect of the Mach number on the voltage–current characteristics.

static pressure has the same, but less pronounced, effect. An increase in the Mach number from 7.1 to 8.15 does not affect noticeably the voltage–current characteristics.

Below, we consider the hysteresis in greater detail. According to paper [6], this phenomenon can be associated with processes that occur at the cathode surface at the boundary separating current and current-free zones of the discharge in the regime when not the entire cathode surface glows (in the case of classic glow discharges, such a regime is usually called normal). However, only processes occurring in the near-cathode regions cannot explain the hysteresis observed in our

experiments, as evidenced by the following arguments. The direction of movement around the hysteresis loop is opposite to that observed in [6], and the value of the hysteresis depends on the interelectrode spacing, i.e., on processes occurring in the volume occupied by the discharge. Apparently, this volume decreases with reducing the electric current more slowly than it increases with the current growth. At the same time, the normal component of the cathode-current density can vary depending on whether the current in the discharge increases or decreases, which is a cause of the hysteresis.

ACKNOWLEDGMENTS

This work was supported by the Russian Foundation for Basic Research, project no. 98-02-17936.

REFERENCES

1. G. I. Mishin, Yu. L. Serov, and I. P. Yavor, *Pis'ma Zh. Tekh. Fiz.* **17**, 65 (1991) [*Sov. Tech. Phys. Lett.* **17**, 413 (1991)].
2. G. I. Mishin, A. I. Klimov, and A. Yu. Gridin, *Pis'ma Zh. Tekh. Fiz.* **18**, 86 (1992) [*Sov. Tech. Phys. Lett.* **18**, 506 (1992)].
3. B. N. Ganguly, P. Bletzinger, and A. Garscadden, *Phys. Lett. A* **230**, 218 (1997).
4. P. Bletzinger and B. N. Ganguly, in *Proceedings of AIAA VIII International Space Planes & Hypersonic Systems and Technologies Conference*, Norfolk, 1998.
5. V. M. Fomin, A. V. Lebedev, and A. I. Ivanchenko, *Dokl. Akad. Nauk* **361**, 58 (1998) [*Dokl. Phys.* **43**, 440 (1998)].
6. L. Rothard, *Mber. Dtsch. Akad. Wiss.* **3**, 18 (1961).

Translated by Yu. Verevochkin

Instability and Gradual Loss of Smoothness Inherent in Flows of Perfect Fluid

V. I. Yudovich

Presented by Academician I.I. Vorovich November 2, 1999

Received November 12, 1999

In this study, we investigated a specific instability inherent in flows of perfect incompressible fluid and appearing as an unlimited growth of strains in liquid particles. As a result, in three-dimensional flows, a vortex grows indefinitely with time, while for two-dimensional flows the growth of the vortex gradient is typical. In the general case, these statements remain to be hypothetical; however, their validity is beyond any doubt considering a set of examples available for particular flows and classes of flows.

The problem of global unambiguous solvability for the Euler equations of perfect incompressible fluid remains to be the most urgent in the mathematical hydrodynamics. Because the local unambiguous solvability was established as early as 1920th in classical studies by N. Günter and L. Liechtenstein, the problem reduces to deriving reasonably strong prior estimates for solutions and, above all, for a vortex. However, the satisfactory results are now known only in the two-dimensional case [1–7]. For example, if the initial data and the boundary of the flow domain are C^∞ -smooth, it is possible to guarantee the existence of a unique C^∞ -smooth solution for all values of the time variable t . An interesting review of results and unresolved problems can be found in [8].

From the physical point of view and also from the point of view of a computer experiment, the conclusion about the smoothness of two-dimensional flows is of somewhat formal character. The examples presented in [9] have shown that the vortex gradient can grow indefinitely with time in two-dimensional flows, while in three-dimensional flows the vortex itself can grow indefinitely. Meanwhile, this is the smoothness, that is conserved uniformly at infinite intervals of time, could be considered as real and observable in natural and computer experiments. Such a conservation of the smoothness can be provided only by the global prior estimates of derivatives, which are based on the conser-

vation laws. In the dynamics of the perfect incompressible fluid, the law of conservation of circulation (the Helmholtz–Thomson theorem) acts also along with the law of conservation of energy. In the two-dimensional case, the vortex conservation follows from the law of conservation of circulation, but constraints are not imposed on its derivatives. In the three-dimensional case, there are no obstacles for the indefinite growth of the vortex and the deformation rate.

There are likely no laws that should require the growth of a vortex for all or at least “almost all” three-dimensional flows, excluding, perhaps, steady, periodic, and quasi-periodic flows. The same can be said also with respect to the vortex gradient in the two-dimensional case. Therefore, such a growth, resulting in a gradual loss of the flow smoothness, sometimes takes place, and sometimes does not. At the same time, it can be assumed with confidence that the class of flows for which this phenomenon occurs is so wide that a dense set of initial data corresponds to this class everywhere in the phase space of the system. As a result, it turns out that almost any steady flow is unstable in the sense of Lyapunov in the vortex metric ($\max|\text{curl}\mathbf{v}| + \text{minor norm}$) in the three-dimensional case and in the vortex-gradient metric ($\max|\nabla\omega| + \text{minor norm}$) in the two-dimensional case. This smoothness-loss phenomenon and a sort of the stochastic behavior associated with it were, for the first time, pointed to in [9].

The results presented in what follows illustrate and confirm the point of view proposed. The details can be found in [10].

1. Basic equations and definitions. The motion of a fluid in the domain $\mathcal{D} \subset \mathbb{R}^n$ with an impenetrable boundary is considered as given if, for an arbitrary liquid particle occupying the position $\mathbf{a} = (a_1, \dots, a_n) \in \mathcal{D}$ at the initial moment $t = 0$, its position $x(\mathbf{a}, t) \in D$ is known for all $t \in \mathbb{R}$; moreover, $x(\mathbf{a}, 0) = \mathbf{a}$. Differentiating with respect to time t gives the Lagrangian velocity field $\mathbf{a} \rightarrow \dot{x}(\mathbf{a}, t)$ at the moment t . The Eulerian velocity field is determined as $\mathbf{v}(x, t) = \dot{x}(x^{-1}(x, t), t)$ at the moment t for an arbitrary $x \in \mathcal{D}$.

Rostov State University,
ul. Zorge 5, Rostov-on-Don,
344104 Russia

For an arbitrary continuum, the following relationship is valid:

$$\dot{S} = DS, \quad (1)$$

$$D = \frac{\partial \mathbf{v}}{\partial x_k} = \left(\frac{\partial v_i}{\partial x_k}(x(\mathbf{a}, t), t) \right)_{i,k=1}^n.$$

Here, $S = \frac{\partial x}{\partial a}$ is the distortion matrix.

The Lagrangian condition of incompressibility for a homogeneous medium is

$$\det S = 1, \quad S = \left(\frac{\partial x_i(\mathbf{a}, t)}{\partial a_k} \right)_{i,k=1}^n. \quad (2)$$

From this condition, it follows that $\text{Tr} D = 0$. D can be represented in the form $D = E + \Omega$, where E is the symmetric matrix (of deformation rates), and Ω is the skew-symmetric matrix (of rotations). For $n = 3$, the action of the skew-symmetric operator Ω on an arbitrary vector $\xi \in \mathbb{R}^3$ is specified by the vector product $\Omega \xi = \frac{1}{2} \omega \wedge \xi$, where $\omega = \text{curl } \mathbf{v}$ is the vortex.

The Lagrange equations of motion for a homogeneous incompressible fluid (with the unit density) can be written in the form:

$$\ddot{x} = -\frac{\partial p}{\partial x}, \quad (3)$$

where $p = p(\mathbf{a}, t)$ is the pressure, and the following designations are used:

$$\frac{\partial p}{\partial x} = \left(\frac{\partial p}{\partial x_1}, \dots, \frac{\partial p}{\partial x_n} \right), \quad \frac{\partial p}{\partial x_i} = \sum_{j=1}^n \frac{\partial p}{\partial a_j} \frac{\partial a_j}{\partial x_i}. \quad (4)$$

The corresponding Euler equations look like:

$$\frac{dv_i}{dt} = -\frac{\partial p}{\partial x_i}, \quad \text{div } \mathbf{v} = 0, \quad \left(\frac{d}{dt} = \frac{\partial}{\partial t} + v_k \frac{\partial}{\partial x_k} \right). \quad (5)$$

Differentiating with respect to x_i , we derive the relationship:

$$\dot{D} = \Pi - D^2, \quad \Pi = -\left(\frac{\partial^2 p}{\partial x_i \partial x_k} \right)_{i,k=1}^n. \quad (6)$$

From this relationship, the pair of equations for E and Ω follows:

$$\dot{E} = \Pi - E^2 - \Omega^2, \quad \dot{\Omega} = -E\Omega - \Omega E. \quad (7)$$

The latter equation yields the conservation law:

$$\frac{d}{dt}(S^* \Omega S) = 0, \quad (8)$$

so that the following equality is fulfilled for all t :

$$S^* \Omega S = \Omega_0, \quad \Omega_0 = \Omega|_{t=0}.$$

In the three-dimensional case, this is the Cauchy classical equation for a vortex:

$$\omega_i = \omega_{0k} \frac{\partial x_i}{\partial a_k}, \quad i, k = 1, 2, 3. \quad (9)$$

Note the following generalization of equation (8): if the matrix-valued function V_λ is the solution to the Cauchy problem $\dot{V}_\lambda = (E + \lambda \Omega)V_\lambda$, $V_\lambda|_{t=0} = I$, then $\frac{d}{dt}(V_\lambda^* \Omega V_\lambda) = 0$. Here, λ is an arbitrary quantity con-

served for liquid particles, i.e., $\frac{d\lambda}{dt} = 0$. For $\lambda = 1$, we have $V_1 = S$.

2. Loss of smoothness at the boundary and the instability of steady flows. Sometimes, it is possible to find the local Lyapunov functional, i.e., the function of Eulerian unknown quantities, which increases (or decreases) monotonically in the course of a motion of a liquid particle. The first example is the plane motion of a fluid when there is a straight stream line, for example, an interval of the x -axis on the plane x, y . In this case, the following relationship holds [9]:

$$\frac{d}{dt} \omega_x \omega_y = \omega \omega_x^2. \quad (10)$$

Here, ω is the vortex, and ω_x and ω_y are its derivatives.

The second example is given by the axially symmetric flow of a fluid. Let u, v , and w be the components of the velocity in the cylindrical coordinates r, θ , and z . If u and w are independent of θ and $v = 0$, then, for a liquid particle moving along an impenetrable cylinder $r = r_0$ (in this case, $u|_{r=r_0} = 0$), the following relationship will be fulfilled:

$$\frac{d}{dt}(qq_r q_z) = r_0 q^2 q_z^2, \quad q = \frac{\omega}{r}, \quad \omega = u_z - w_r. \quad (11)$$

If the trajectory of the liquid particle lies in the plane $z = z_0$, we shall have

$$\frac{d}{dt} \left(\frac{q}{r} q_r q_z \right) = -q^2 q_r^2. \quad (12)$$

It is worth noting that the value ω in the plane case and the value q in the axially symmetric case are conserved in the liquid particle: $\dot{\omega} = 0$ and $\dot{q} = 0$.

If the boundary of the domain \mathcal{D} contains a portion of the plane $x_3 = 0$ in which the rectilinear trajectory $x_2 = 0$ of the liquid particle lies, then

$$\frac{d}{dt} \omega_1 \omega_2 \omega_3 = -\omega_1^2 \omega_3^2. \quad (13)$$

The following lemma is applicable to these situations [9].

Lemma. *Let us assume that f and g are the smooth functions of time t : $0 \leq t < \infty$, and the following equation is fulfilled:*

$$\frac{d}{dt}fg = \omega f^2, \quad \omega = \text{const.} \quad (14)$$

Let $\omega f(0)g(0) > 0$. In this case, the function $f^2(t) + g^2(t)$ is unbounded on the interval $[0, \infty)$, i.e., such a sequence $t_n \rightarrow +\infty$ exists that $f^2(t_n) + g^2(t_n) \rightarrow \infty$. Moreover, the function $f^2(t) + g^2(t)$ tends to infinity at $t \rightarrow +\infty$ "with the probability equal to unity." This means that, for any real N at $T \rightarrow +\infty$, the limiting equality is valid:

$$\frac{1}{T} \text{mes}\{t: f^2(t) + g^2(t) > N^2; 0 \leq t \leq T\} \rightarrow 1. \quad (15)$$

According to this lemma the modulus of the vortex gradient increases indefinitely at $t \rightarrow +\infty$ both in the plane and axially symmetric cases considered above, broadly speaking, for the half of the initial data (for another half, this takes place at $t \rightarrow -\infty$). In the three-dimensional case, it follows from (13) that the vortex itself increases indefinitely.

The class of flows with the indicated broken smoothness is so large that its representatives can be found in an arbitrarily small vicinity of an arbitrary steady regime. More precisely, an arbitrarily small C^∞ -smooth local (near a point of rectilinear trajectory of a liquid particle) perturbation leads to a flow with a damage of the smoothness under the conditions specified by theorem 1.

Theorem 1. *Under conditions of equalities (10)–(12), any steady flow (for example, in the case of a band confined between a straight line and a certain curve, or in the similar domain of rotation) is unstable in the vortex-gradient metric.*

Under conditions specified by equality (13) (for example, for flows in a parallelepiped), any steady flow is unstable in the vortex metric.

Recall that, according to the Arnold results [11, 12], there are many plane and axially symmetric steady flows stable in the vortex metric.

3. Incompressible motions of a dust medium. If particles of a continuum do not interact, each of them execute coasting along the geodesic line, which is a straight line in the \mathbb{R}^n case. In the classical works by Ya.B. Zel'dovich, the theory of a self-gravitating dust medium is used as the basis for investigating the universe at large scales [13]. The Lagrange equations of motion look like $\ddot{x} = 0$; whence it follows that $x(\mathbf{a}, t) = \mathbf{a} + t\mathbf{v}_0(\mathbf{a})$, where \mathbf{v}_0 is the initial velocity. The Euler equation of motion is $\frac{d\mathbf{v}}{dt} = 0$, or, in coordinates,

$$\frac{\partial v_i}{\partial t} + v_k \frac{\partial v_i}{\partial x_k} = 0, \quad i = 1, \dots, n. \quad (16)$$

In general, the equations for a dust medium can be obtained from the corresponding equations for an incompressible fluid by putting $p = 0$ in the latter ones and rejecting the incompressibility conditions $\det S = 1$ and $\text{div } \mathbf{v} = 0$. Instead of (6), we have

$$\dot{D} = -D^2. \quad (17)$$

This equation for a liquid particle can be integrated:

$$D(t) = D(\mathbf{a}, t) = (I + tD_0)^{-1}D_0, \\ D_0 = D_0(\mathbf{a}) = D(\mathbf{a}, 0).$$

In the one-dimensional case, the collapse always takes place: the nonzero solution of set (16) cannot be determined for all $t \in \mathbb{R}$. For $n \geq 2$, the globally defined motion of continuum is possible if D_0 has no real eigenvalues except, maybe, zero.

It turns out that the incompressibility condition $\det(I + tD_0) = 1$ is fulfilled for a dust medium if and only if $D_0^n = 0$; i.e., D_0 is a nilpotent operator. In this case for all t

$$D(t) = (I - tD_0 + t^2D_0^2 - \dots + (-1)^{n-2}t^{n-2}D_0^{n-2})D_0.$$

It turns out that the incompressible flows of a dust medium are globally defined, but both the deformation rates and the vortex grow polynomially with time (linearly, in the \mathbb{R}^3 -case). The examples of such flows can be found in [10]. Note that the solutions of the Euler equations of the type considered are mentioned in [14].

4. Three-dimensional instability of plane flows. A plane flow with the velocity field $(u(x, y, t), v(x, y, t))$ in the domain $\mathcal{D} \in \mathbb{R}^2$ can be treated as the three-dimensional flow in the cylinder $\mathcal{D} \times \mathbb{R}$ with the velocity field $(u, v, 0)$. For perturbed flows, we lay down the condition of periodicity for velocity and pressure in the axial variable z . If the initial perturbation of the velocity field looks like $(0, 0, w_0(x, y))$, i.e., the z -component of the velocity is independent of z , then $u(x, y, t)$, $v(x, y, t)$, and $p(x, y, t)$, as before, will be defined by the two-dimensional Euler equations in the \mathcal{D} domain. For the z -component $w = w(x, y, t)$, we have the Cauchy problem:

$$\frac{dw}{dt} = 0, \quad w(x, y, 0) = w_0(x, y) \quad (18)$$

$$\left(\frac{d}{dt} = u\partial_x + v\partial_y \right).$$

This problem is globally univalently solvable, and $\max|w(x, t, y)|$ with respect to $(x, y) \in \mathcal{D}$ is t -independent. However, the derivatives w_x and w_y , as a rule, grow with time.

Let u, v, p be a time-independent solution of the plane problem in \mathcal{D} , the boundary $\partial\mathcal{D}$ being impenetrable. Let ψ be the corresponding stream function, and $\psi = c_0$ be the nondegenerate stream line, so that

$|\nabla\psi| \neq 0$ everywhere in this line. In this case, we can introduce the action-angle variables ψ, ϕ in the vicinity of this line, where ϕ is determined as the solution of the differential equation $\frac{d\phi}{ds} = v(c)|\nabla\psi|$ in every line $\psi = c$. Here, s is the arc length, and $v(c)$ is the frequency of rotation of a liquid particle with the axis of rotation being aligned with the stream line $\psi = c$. In this case, $s = 0$ corresponds to a certain curve which is a transversal to the stream line $\psi = c_0$. Then, equation (18) takes the form $w_t + v(\psi)w_\phi = 0$, and the solution of Cauchy problem (18) is $w = w_0[\phi - tv(\psi), \psi]$. Now, it is easy to verify that $|\nabla w| \rightarrow \infty$ as $t \rightarrow \infty$ always when the following conditions are fulfilled:

$$\inf_{\phi} \left| \frac{\partial w_0(\phi, c_0)}{\partial \psi} \right| > 0, \quad v'(c_0) \neq 0. \quad (19)$$

The first condition is fulfilled by the choice of the initial velocity w_0 , while the second one is the condition of the nonlinearity for a pendulum with the Hamiltonian function $\psi(x, y)$. This condition is not always (but as a rule) fulfilled. For example, if $\psi = \psi(r)$, where r is the polar radius, then $v'(\psi) = 0$ everywhere only in the case of the solid-state rotation, when $\psi(r) = \omega r^2/2$.

5. Composition of Lagrangian motions and the time growth of a vortex. The configuration space for a perfect incompressible fluid in a fixed domain is a group of volume-conserving transformations. It is natural to ask: under which conditions will the composition $g(t)h(t)$ of two solutions of Lagrange equations (2) and (3) also be a solution? The general answer is unknown, but some examples can be given.

Let $[U(y), 0, 0]$ and $[0, 0, W(x, y)]$ be two steady flows (x, y, z are the Cartesian coordinates in \mathbb{R}^3) with smooth profiles U and W . The following motions $g(t), h(t)$ [$(a, b, c) \in \mathbb{R}^3$] of particles correspond to these flows:

$$\begin{aligned} g(t)(a, b, c) &= (a + tU(b), b, c), \\ h(t)(a, b, c) &= (a, b, c + tW(a, b)). \end{aligned} \quad (20)$$

The composition acts according to the rule $g(t)h(t) = [a + tU(b), b, c + tW(a, b)]$. The corresponding Euler field

$$(U(y), 0, W(x - tU(y), y)) \quad (21)$$

satisfies the Euler equations with the pressure $p = 0$. We arrived at the incompressible motion of a dust medium. However, an analogous flow in the cylindrical coordinates with the components

$$u = 0, \quad v = V(r), \quad w = W\left(r, \theta - t\frac{V(r)}{r}\right) \quad (22)$$

corresponds to a nonzero pressure $p = p(r)$ determined from the equation $\frac{dp}{dr} = \frac{V^2}{r}$. Solution (21) can be considered as a flow in the layer $y_1 < y < y_2$ with impenetrable walls $y = y_1$ and $y = y_2$. We can conclude that the steady flow $[0, 0, W(x, y)]$ is unstable in the sense of Lyapunov in the vortex metric for an arbitrary periodic (with respect to x) and variable profile $W(x, y)$. This is the rare instance when it has been possible to establish the instability by presenting an explicitly growing perturbation. Note that solution (21) in the particular case when $U = \sin y, W = \cos x$ is presented (with a misprint) in [8]. Correspondingly, solution (22) helps to establish that both flows $[0, 0, W(r, \theta)]$ and $[0, V(r), 0]$ are unstable in the vortex metric if $\frac{V}{r}$ is not a constant and $\frac{\partial W}{\partial \theta} \neq 0$.

ACKNOWLEDGMENTS

This work was supported by the Russian Foundation for the Basic Research, grant no. 99-01-01023.

REFERENCES

1. W. Wolibner, Math. Zam., No. 37, 698 (1933).
2. V. I. Yudovich, Dokl. Akad. Nauk SSSR **136**, 564 (1961) [Sov. Phys.-Dokl. **6**, 18 (1961)].
3. V. I. Yudovich, Zh. Vychisl. Mat. Mat. Fiz. **3**, 1032 (1963).
4. V. I. Yudovich, Dokl. Akad. Nauk SSSR **146**, 561 (1962) [Sov. Phys.-Dokl. **7**, 789 (1962)].
5. V. I. Yudovich, Mat. Sborn. **106**, 562 (1964).
6. T. Kato, Arch. Rat. Mech. **27**, 188 (1968).
7. V. I. Yudovich, Math. Res. Lett., No. 2, 27 (1995).
8. J. F. Marsden, D. G. Ebin, and A. E. Fischer, in *Proceedings of XIII Biennial Seminar of the Canadian Math. Congress*, 1972, Vol. 1, p. 135.
9. V. I. Yudovich, in *Dynamics of Continuum* (Novosibirsk, 1974), No. 16, p. 71.
10. V. I. Yudovich, Available from VINITI, 1998, Moscow, No. 2331-B98.
11. V. I. Arnold, Ann. Inst. Fourier **16**, 316 (1966).
12. V. I. Arnold, Izv. Vyssh. Uchebn. Zaved., Math., No. 5, 3 (1966).
13. Ya. B. Zel'dovich and A. D. Myshkis, *Elements of Mathematical Physics* (Nauka, Moscow, 1973).
14. P. Serfati, J. Math. Pures Appl. **74**, 95 (1995).

Translated by V. Bukhanov